2016

Characterization of Tensile Deformation in AZ91 Mg Alloy Castings

Ogun Unal
University of North Florida, n00977101@ospreys.unf.edu

CHARACTERIZATION OF TENSILE DEFORMATION IN AZ91 MG ALLOY CASTINGS

By

Ogűn Únal

A thesis submitted to School of Engineering

In partial fulfillment of the requirements for the degree of

Master of Science in Mechanical Engineering

UNIVERSITY OF NORTH FLORIDA

COLLEGE OF COMPUTING, ENGINEERING and CONSTRUCTION

April, 2016

CERTIFICATION OF APPROVAL

This thesis titled “Characterization of Tensile Deformation in AZ91 Mg Alloy Castings” of Ogűn Űnal is approved by:

Date

_____ _____
Dr. Murat Tiryakioğlu, Ph.D., CQE, Advisor

_____ _____
Dr. Paul Eason, Ph.D., PE, Committee Member

_____ _____
Dr. Stephen Stagon, Ph.D., Committee Member

Accepted for the School of Engineering:

_____ _____
Director of School of Engineering,
Dr. Murat Tiryakioğlu, Ph.D., CQE

Accepted for the College of Computing, Engineering and Construction

_____ _____
Dr. Mark A. Tumeo, Ph.D., PE,
Dean of the College of Computing, Engineering and Construction

Accepted for the University:

_____ _____
Dr. John Kantner, Ph.D.
Dean of the Graduate School

DEDICATION

This thesis is dedicated to my professor Dr. Murat Tiryakioğlu

who has been a constant source of knowledge and inspiration to me.

Without him, I would be just another engineer.

"Non Scholae Sed Vitae Discimus"

ACKNOWLEDGMENTS

The completion of this thesis could not have been possible without the guidance and participation of my colleagues. Their contributions are sincerely appreciated and gratefully acknowledged. It was a priceless pleasure and great experience working with great faculty and also being a part of a university like University of North Florida.

I would like to express my deep appreciation to Dr. Murat Tiryakioğlu for his patience, endless support and understanding spirit. It was a great honor for me to work under his supervision. His support was essential to my thesis and also to my life. His wisdom made me a better engineer and a better person. His desire to see me happy, healthy and successful is the most powerful motivation I can ever imagine.

I am thankful for the chance of working with Dr. Paul Eason and Dr. Stephen Stagon for the valuable discussions which were essential to this degree.

I would like to thank Dr. Derya Dispinar for his support and supervision. His encouragement for my career means a lot to me. I also thank my colleagues, Muhammet Uludag, Huseyin Ozdes, for their support during my research.

Finally, I would like to thank my parents and my sister for their continued support.

TABLE OF CONTENTS

LIST OF TABLES

LIST OF FIGURES

LIST OF SYMBOL AND ABBREVIATIONS

Al – Aluminum

Mg – Magnesium

Al_2O_3 – Alumina

HCP – Hexagonal Close-Packed

MPa – MegaPascal

SEM – Scanning Electron Microscope

σ – True Stress (MPa)

ε_p – True Plastic Strain

σ_y – Yield Stress (MPa)

e_F – Elongation to Fracture (%)

E – Modulus of Elasticity (MPa)

KM – Kocks–Mecking

K – Kocks–Mecking Parameter

K_v – K parameter for the Voce equation (MPa)

K_H – K parameter for the Hollomon equation, also known as strength coefficient (MPa)

K_L – K parameter for the Ludwik equation (MPa)

K_S – K parameter for the Swift equation (MPa)

Θ – Work hardening rate (MPa)

Θ_0 – Initial work hardening rate (MPa)

ABSTRACT

Tensile deformation characteristics of cast aluminum alloys have been investigated extensively. Cast Mg alloys have remained mostly neglected by researchers, despite their potential for weight savings. This present study is motivated by this gap in the literature and consists of two stages; in Stage 1, analysis of tensile data gathered from literature were reanalyzed, and in Stage 2, data generated from tensile testing of 60 specimens of AZ91 Mg alloy castings in both T4 and T6 conditions were analyzed to characterize work hardening behavior.

In Stage 1, more than 1600 data were collected from the literature for various Mg alloy families. After plotting these data in yield strength-elongation charts, highest points were identified and interpreted as the maximum ductility, i.e., ductility potential (e_{Fmax}). The trend in maximum points indicated a linear relationship with yield strength (σ_Y), expressed as;

$$e_{F(max)}\,\% = 41.8 - 0.106\sigma_Y \qquad (1)$$

This ductility potential equation can be used as a metric to compare elongation obtained from tensile specimens to measure the structural quality of Mg alloy castings. Moreover, results indicated that ductility potential was not affected by heat treatment, grain size (within 30-120 μm), casting geometry, size, the type of casting process nor chemical composition.

In Phase 2, AZ91 cast Mg alloy specimens in T4 and T6 conditions were tested in tension to obtain stress-strain data for each specimen. Fits of four constitutive equations, namely, the Hollomon, Voce, Ludwik and Swift, to true stress-true plastic strain data in the elastoplastic region were characterized for the specimens with highest elongation

values for T4 and T6 specimens. The coefficient of determination, R^2, values for all equations were in excess of 0.99, suggesting that all four equations provide excellent fits to tensile data in both conditions.

The change in work hardening rate with true stress was investigated for all specimens by using Kocks-Mecking (KM) plots. It was determined that work hardening behavior of Mg alloy castings in T4 and T6 is distinctly different. In T4 specimens, there is a plateau in work hardening rate at approximately E/25 which was observed in all specimens. The presence of this plateau is consistent with results given in the literature for pure Mg. However, this plateau was not observed in any of the T6 specimens. The reasons for the absence of the plateau in T6 specimens are unknown at this time. In both T4 and T6 specimens, the KM work hardening model in which work hardening rate changes linearly with true stress was found to be applicable. This is the first time that KM model was found to be valid for Mg alloys. Moreover in all specimens, there was a sudden drop in work hardening rate just prior to final fracture. This drop was first hypothesized to be due to structural defects in specimens, which was subsequently validated via fractography. Structural defects were found in all specimens whose fracture surfaces were investigated, indicating low to medium levels of quality.

The quality index method, originally developed for cast aluminum alloys as the ratio of elongation to ductility potential, was found not to be applicable to Mg alloys, at least in its original form. This is due to the fact that work hardening behavior of cast aluminum alloys follows the KM model and there is no plateau where work hardening rate is constant. Hence the work hardening behavior of cast aluminum alloys and AZ91 specimens in T6 condition was similar. However the plateau of constant work hardening

rate had a strong effect on elongation in T4 specimens. Therefore quality index analysis, which is supposed to be independent of alloy condition, did show that T4 and T6 specimens had different quality index levels. This finding contradicted the result from Stage 1 that aging has no effect on ductility potential. However because of the presence of structural defects in all specimens, quality index levels were low (0.30-0.45). Therefore it is unclear at this point whether the work hardening behavior of T4 and T6 specimens would still be different if elongation values were in the proximity of the ductility potential line. More research is needed to characterize work hardening behavior of cast Mg alloys in the absence of major structural defects and also address other questions raised in this study.

CHAPTER 1: INTRODUCTION

The density of Mg alloys ranges from 1.5 g/cm^3 in Mg-Li to 1.8 g/cm^3 in Mg-RE alloys [1]. Because of their low density, Mg alloys offer significant weight saving potential in load-bearing applications, where weight is critical [2], such as in automotive and aerospace applications. Nevertheless, cast Mg alloy castings have not been used as commonly as cast aluminum alloys. The barriers to their wider use have been recently stated [3]: (i) porosity and hot–tearing during solidification, (ii) complex thermal treatments and (iii) the lack of knowledge for process design to produce high–integrity cast magnesium components with high ductility and strength i.e., low porosity that are free from oxide inclusions. For wider use of Mg alloy castings in structural applications, these barriers need to be overcome through careful improvement of casting processes. Therefore, the effect of structural defects such as porosity and oxide inclusions on the performance of Mg alloy castings needs to be investigated.

Structural defects in castings adversely affect mechanical properties, including fatigue life [4,5], elongation [6,7,8,9] and tensile strength [10,11]. Research [12] has shown that the inclusions in castings are mostly prior surface oxides that have been entrained into the casting. These surface films fold over and form a bifilm which act as nucleation sites for pores and intermetallics, and eventually lead to premature fracture under load. It is imperative that the initial melt has a low number of entrained films and the filling system needs to be designed to minimize or even eliminate additional damage by entrainment of new surface films. In the absence of structural defects, cast Mg alloys [13] can have tensile ductility that is significantly higher than most results reported in the literature.

In cast Al alloys, it was found [14,15,16] that true tensile deformation characteristics cannot be determined when structural defects are present, because these defects reduce the work hardening rate. Moreover, a sudden drop in work hardening rate was observed just before final tensile fracture as a result of major structural defects. Tensile deformation has been shown as a tool to assess structural quality. There have been only limited number of studies [17,18,19] conducted on the tensile deformation characteristics of Mg alloys. This study is motivated by this gap in the literature.

In Chapter 2, literature review is provided about commonly known mechanical properties of Mg alloys, alloy designations, historical development of magnesium alloys and advantages and disadvantages for industries. Moreover, important casting process variables are introduced and their effects on the casting quality are discussed.

In Chapter 3, quality index approach taken by Tiryakioğlu have been used for Mg alloy castings which was the previous study of the author. In that study [13], author collected over one thousand and six hundred data points from various studies and plotted them to the elongation-yield strength chart. Ductility potential line and the equation of the line were presented. Mg alloy castings that near the ductility potential line are examined. Effects of grain size, dendrite arm spacing, section thickness, heat treatment and casting processes are discussed. Equation of the line and the estimation of ductility potential in the literature are compared.

In Chapter 4, selected Mg alloy and the chemical composition of the specimens are presented. Casting process and heat treatment procedure of the samples are given. Dimensions of the specimens and the details regarding the preparation of the sample are provided. Experimental procedure that author followed in this study is explained.

In Chapter 5, quality index of both heat treatment conditions are provided and compared with the help of ductility potential concept for both tempers. Best fits of constitutive equations in order to characterize the tensile deformation of Mg alloys are analyzed. Kocks-Mecking analysis is conducted and relationship between elongation, also alternatively quality index and work hardening parameters is observed. Contribution of Stage II work hardening to the T4 specimens is investigated. Important questions regarding the reasons of differences have been raised. Bifilms and pores on the fracture surfaces have been investigated with the help of fractographs that obtained with SEM analysis.

In Chapter 6, conclusions for the characterization of cast AZ91 magnesium alloys are presented.

In Chapter 7, relevant questions that have been raised regarding the results are mentioned.

CHAPTER 2: LITERATURE REVIEW

Magnesium can be extracted from the hydrosphere or lithosphere. Research [20] stated that supplies for magnesium can practically be considered as unlimited. In the sea water, every 1 km^3 sea water contains 1.3 million tons of magnesium. Moreover, magnesium can be found as ores such as dolomite ($MgCO_3.CaCO_3$) and magnesite ($MgCO_3$) in the earth's crust.

2.1. Properties of Magnesium

Magnesium is a member of the periodic table group 2, having atomic number of 12 and atomic weight of 24.31 g/mol [21]. Magnesium is the lightest of all commonly used metals with the density of 1.74 g/cm^3. It has a melting point of 650^{o}C, an electrical conductivity of 39%IACS and a thermal conductivity of 167W/mK [21]. Physical properties of magnesium were presented in the literature [22].

The crystal structure of magnesium is hexagonal close-packed (HCP) and consequently, slip is more limited than in body-centered cubic (BCC) and face-centered cubic (FCC) crystal structures. With the lattice parameters a=3.18Å and c=5.19Å, magnesium has a c/a ratio of 1.624 [21]. Alloying additions affect the c/a ratio in Mg. Table 1 shows the list of the crystallographic indices of the slip and twinning planes and directions in Mg.

Deformation in magnesium initially starts with basal slip, which saturates quickly and leads to twinning. Depending on the parameters such as c/a ratio, other slip planes can be activated. Slip requires higher shear stress and consequently usually results in brittle behavior.

Table 1: Crystallographic indices of the slip and twinning planes and directions of magnesium [21].

Planes	Directions	Type	Slip Direction	Number of Independent Systems
{0001}	$<11\bar{2}0>$	Basal	a	2
$\{10\bar{1}0\}$	$<11\bar{2}0>$	Prismatic	a	2
$\{11\bar{2}1\}$	$<11\bar{2}0>$	Pyramidal	c+a	4
$\{10\bar{1}2\}$	$<10\bar{1}1>$	Pyramidal (Twinning)	c+a*	3
$\{10\bar{1}1\}$	$<10\bar{1}2>$	Pyramidal (Twinning)	c+a*	3
$\{11\bar{2}2\}$	$<10\bar{2}3>$	Pyramidal (Twinning)	c+a	4
$\{11\bar{2}1\}$	$<10\bar{2}\bar{6}>$	Pyramidal (Twinning)	c+a	4

* Frequent ones

Magnesium can be used in pure form just like most of the other metals. Its HCP structure and atomic diameter allow for extended solid solubility with many elements. Like other alloying systems, main purpose of alloying with magnesium is achieving improvements for alloy properties, especially strength [23]. Most commonly used alloying elements for magnesium are aluminum, zinc, manganese, zirconium, silver, yttrium and rare earth elements. Among all these alloying elements, aluminum is considered as the most common alloying element in Mg alloys [24]. Moreover, copper, nickel and iron are considered as harmful impurities for the quality of magnesium alloys.

2.2. History of Applications of Magnesium Alloys

First automotive application of magnesium alloys was reported as Indy 500 in 1918 [21]. Also magnesium alloy castings were used for city buses and tractors in England. Other applications emerged in Germany such as crankcases and housings were

made of Mg alloy castings [25]. Most of magnesium alloys were produced by high - pressure die casting process. Magnesium alloys were one of the main aerospace construction metals and were used for German military as early as World War I and exclusively for German aircraft in World War II [21]. Popularity of magnesium alloys increased with the World War II. Magnesium alloy sheet, casting, forgings and extrusions were used by the United States Air Force and Soviet aircraft industry. Commercial air plane producers such as Boeing decided to use magnesium alloys for control surfaces, door frames, wheels, engine gear boxes, power generation components and structural components in 1950s. After several reports were issued about magnesium alloys being dangerous due to corrosion problems and flammability, the use of magnesium alloys started to decline. Currently most common uses of magnesium are engine castings and landing gears. Magnesium has also been used in helicopter industries such as gear boxes [21].

Magnesium wheels that produced with sand casting were used by Porsche in 1960s for racing cars [26]. These magnesium parts lasted more than 150,000 km. However due to the lack of the improvement in die casting technology, automotive industry started to lose interest in magnesium alloys [27]. The peak of the use of magnesium alloys was the Volkswagen Beetle in 1970s for air-cooled engines and gear boxes [21].

After 1970s, the use of magnesium as a structural powertrain component dwindled. The reasons behind this result were greater power requirements for the engine. Therefore application of water cooling instead of air cooling gained more popularity [21]. However most magnesium alloys could not tolerate the new operating environments. As

stated above, corrosion resistance was one the major resistance for the use of magnesium alloy and therefore efforts were made to eliminate this disadvantage for structural magnesium alloys. Consequently, high purity alloys such as AZ91D, AZ91C, AM60B and AM60A were developed in the 1980s that resulted in increase of cost which in turn limited the wider use of magnesium alloys in automotive applications [21]. Recently, a significant interest in magnesium alloys as a light-weight material to be used in transportation has been reported [28,29]. Nowadays, cast magnesium alloys are becoming just as popular in industry as wrought magnesium alloys. Main reason behind this result is isotropy in mechanical properties of castings and economic advantages of castings related to mass production [30].

The most significant issue in the production of magnesium alloy components is the fire hazard, especially during machining process because of the low melting point of magnesium alloys [21]. It must be noted that especially thin chips comparing to the thick ones and the dust in grinding are more likely flammable, if heated to melting temperature. They can easily ignite or explode during the process. To eliminate fire risks, fine cuts, dull tools, power tool design and heat buildup need to be avoided and proper coolant needs to be used. Chips and dust on the machines, on the ground or on the clothes must be cleaned carefully before process. It must be noted that water based coolants cannot be used since they reduce the salvage value of the scrap and increase the risk of fire [21].

2.3. Mg Alloy Designations

A designation system for Mg alloys was developed by the American Society for Testing and Materials (ASTM) and is outlined in ASTM-B257. [31]. This designation uses a three part code. First part is the letter that shows the major elements in the alloy.

Second part shows the composition of the alloy and third part code is the letter that differentiates the alloys which have the same designation. As an example: ZQ91D indicates that this alloy contains 9% Zinc, 1% Silver and “D” indicates that the fourth alloy that registered. Table of codes for each alloying element is given in Table 2 [31].

Table 2: Codes of each element for the designation of magnesium alloys [31].

CODE	ALLOYING ELEMENT
A	Aluminum
B	Bismuth
C	Copper
D	Cadmium
E	Rare Earth Elements
F	Iron
H	Thorium
K	Zirconium
L	Lithium
M	Manganese
N	Nickel
Q	Silver
R	Chromium
S	Silicon
T	Tin
W	Yttrium
Y	Antimony
Z	Zinc

Temper designations for Mg alloys are provided in Table 3. Most commonly used tempers in cast Mg alloys are F, T4, T5, T6 and T7.

Table 3: International temper designations [32].

Temper	Definition
F	As fabricated
T1	Cooled from an elevated temperature shaping process and naturally aged
T2	Cooled from elevated temperature - shaping process, cold worked, and naturally aged
T3	Solution heat treated, cold worked and naturally aged
T4	Solution heat treated and naturally aged
T5	Cooled from an elevated temperature - shaping process and artificially aged
T6	Solution heat treated and artificially aged
T7	Solution heat treated and artificially overaged
T8	Solution heat treated, cold worked, and artificially aged
T9	Solution heat treated, artificially aged and cold worked
T10	Cooled from elevated temperature shaping process, cold worked, and artificially aged

Studies have been conducted [31] on the effects of other alloying elements on the mechanical properties such as tensile strength and hardness. For instance, aluminum additions to Mg result in the formation of the β-$Mg_{17}A_{l2}$ phase, which increases strength. Moreover corrosion resistance and castability are improved when aluminum and zinc are added together. Zinc additions refine grain structure, whereas Si additions improve creep resistance, however reduce the castability and corrosion resistance [23,31,33]. Most widely used cast Mg alloys and their typical characteristics are presented in Table 4 [34].

Table 4: Most commonly used magnesium alloys and their characteristics [34].

Alloy	Characteristics
AZ63	Good room temperature strength and ductility
AZ81	Tough, leak tight castings with 0.0015Be, used for pressure die-casting
AZ91	General-purpose alloy used for sand and die castings
AM50	High-pressure die castings
AM20	Good ductility and impact strength
AS41	Good creep properties to 150^{o}C
AS21	Good creep properties to 150^{o}C
AE42	Good creep properties to 150^{o}C
ZK51	sand castings, good room temperature strength and ductility
ZK61	As for ZK51
ZE41	Sand Castings, good room temperature strength, improved castability
ZC63	Pressure-tight castings, good elevated temperature strength, weldable
EZ33	Good castability, pressure-tight, weldable, creep resistant to 250^{o}F
HK31	Sand castings, good castability, weldable, creep resistant to 350^{o}F
HZ32	Same as for HK31
QE22	Pressure tight and weldable, high proof stress to 250^{o}C
QH21	Pressure-tight, weldable, good creep resistance and proof stress to 300^{o}C
WE54	High strength at room and elevated temperatures
WE43	Good corrosion resistance, weldable
M1	Low-to-medium-strength alloy, weldable, corrosion resistant
AZ31	Medium-strength alloy, weldable, good formability
AZ61	High -strength alloy, weldable
AZ80	High-strength alloy
ZM21	Medium-strength alloy, good formability, good damping capacity
ZK30	High strength alloys
ZK60	Good formability
ZMC711	High strength alloys
HK31	High creep resistance to 350^{o}C, short time exposure to 425^{o}C, weldable
WE43	High temperature creep resistance
WE54	High temperature creep resistance
LA141	Ultra-light weight

2.4. Mg Alloy Castings and Casting Defects

For complex shaped parts, casting process is usually the preferred method of production. The most common casting method for magnesium alloy products has been die-casting, especially for automotive applications [35]. Like aluminum alloys, magnesium alloys oxidize rapidly in air. Magnesium alloys are very sensitive to turbulence during pouring, leading structural defects in the castings [36], which will be discussed in the next section.

AZ91 is the most widely used magnesium alloy for many applications including aerospace and automotive applications [34]. Mg-Al alloys where aluminum is the major alloying element, shows very good castability [37,38]. This result leads to the use of magnesium alloys in pressure assisted casting processes such as high pressure die casting. Moreover, other alloy series such as WE shows lower castability. Casting methods such as permanent and sand mold casting can be supported by pressure in purpose of achieving thin walled structures [26]. Magnesium has great die-filling properties. Therefore large, thin-walled and complex shaped components can be produced with magnesium alloys. Studies [26] also indicated that low heat capacity, lower latent heat of solidification and less affinity to iron are further advantages of magnesium castings.

2.5. Casting Defects

Casting defects, namely inclusions and pores, are produced during the casting process but affect the properties and performance of castings adversely. In contrast, most materials science textbooks emphasize the effect of microstructure, such as grain size, dendrite arm spacing (DAS), secondary phases, eutectic structures and interface properties, on mechanical properties in which engineers are taught that mechanical

properties are determined by microstructure. For example, reducing grain size is considered as a way to increase yield strength due to the Hall-Petch affect:

$$\sigma_y = \sigma_0 + \frac{k}{\sqrt{d}} \qquad (2)$$

where σ_0 is a material constant (MPa) and d is the grain size (μm), k is the specific strengthening coefficient for each material ($MPa.\mu m^{0.5}$). During deformation, grain boundaries act as obstacles for the dislocation movement, which results in increase in strength. Strengthening in Mg alloys is achieved in precipitation hardening (e.g., Mg-Zn, Mg-Al and Mg-Ag systems), solute solution hardening and/or grain size hardening. Similar to the effect of grain size, reduction in dendrite arm spacing, for instance by solidification at higher rates, leads to higher strength. From a metallurgical standpoint, a reduction in grain size or DAS, should result in lower ductility because it is an established metallurgical principle that there is a strength-ductility compromise. One property has to be sacrificed to gain in the other. However, elongation was reported to increase with decreasing DAS in cast Al [39,40] and in Mg [21] alloys. Therefore, the traditional thinking that "the microstructure controls the properties" for cast metals has been questioned recently. Campbell [41] commented on the effect of microstructure on properties as "at worst this not true, and at best it is a half-truth". Moreover, Campbell [41] also stated that reduced grain size is only effective in increasing elongation when the melt is not clean.

The main defects in castings are bifilms and pores. Oxides, that form on the surface of the molten metal, get entrained into liquid metal during melting (surface of ingot), melt transfers [42] or mold filling, as depicted schematically in Figure 1. Because

most bifilms have neutral buoyancy in liquid metal, they remain suspended in the melt [4]. During solidification, intermetallics usually nucleate and grow on these bifilms. An example is provided in Figure 2, in which Fe-bearing intermetallics precipitates on a bifilm (indicated by an arrow).

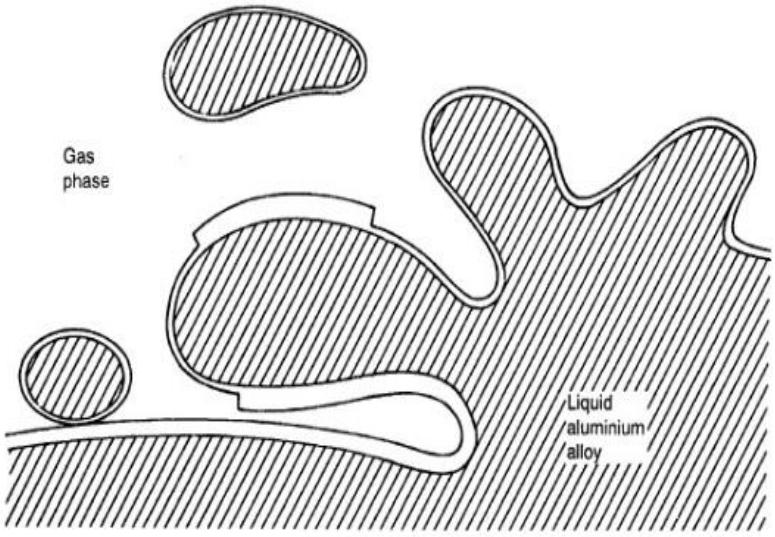

Figure 1: Folding action of a bifilm [4].

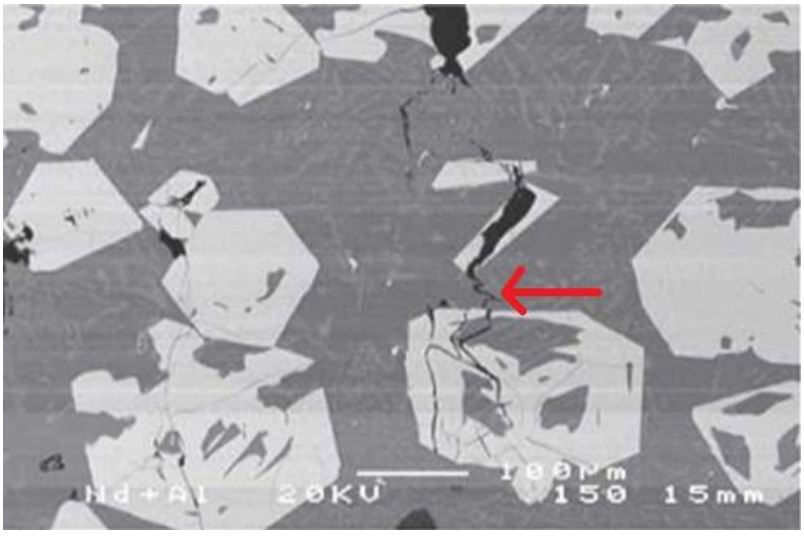

Figure 2: Typical example of a bifilm on which Fe containing intermetallics precipitated in an Al-Si alloy [43].

Another example of a convoluted, coarse bifilm is provided in Figure 3. The shiny parts of the bifilm are one-half of the bifilm.

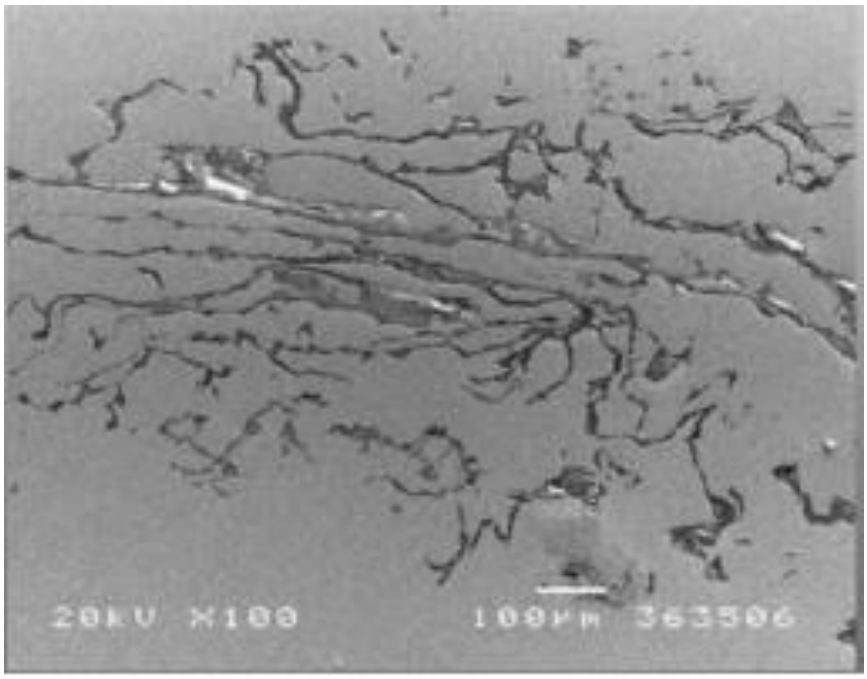

Figure 3: Relatively old and thick tangled bifilm on polished surface [12].

2.6. Tensile Deformation

Work hardening takes place because of the increase in dislocation density with deformation. Work hardening rate, Θ, can be written as;

$$\Theta = \frac{d\sigma}{d\varepsilon_p} \tag{3}$$

Characterization of work hardening involves analysis of both true stress – true plastic strain relationship as well as the change of work hardening rate at different stage of deformation. Deformation occurs in mono- and polycrystals in several stages. Stage I occurs only during single slip in single crystals. This stage is known as easy glide because large amount of strain can be achieved without much work hardening. When

certain amount of strain is reached, a transition occurs for single crystals from low hardening rate to larger and cause the raise of Stage II [44]. Stage II, also referred to as athermal work hardening, is a stage with a higher work hardening rate. Stage II occurs in both single crystals and polycrystals and work hardening rate decreases with increased testing temperature. Stage I and Stage II occur independently. Stage III (dynamic work hardening), corresponds to a steady decrease of work hardening rate [44].

Research [45,46] on the work hardening characteristics of pure magnesium single crystals showed that Stage I, Stage II and Stage III work hardening all took place, similar FCC metals [47]. Caceres and Blake [17] investigated the work hardening behavior of cast pure Mg in tension and compression. Work hardening rate-true stress plot reported by Caceres and Blake is presented in Figure 4. Note that there is a plateau in work hardening rate at approximately 1.7 GPa for the curve for tension (as indicated by the arrow). This is unique to Mg and was not reported for cast Al alloys.

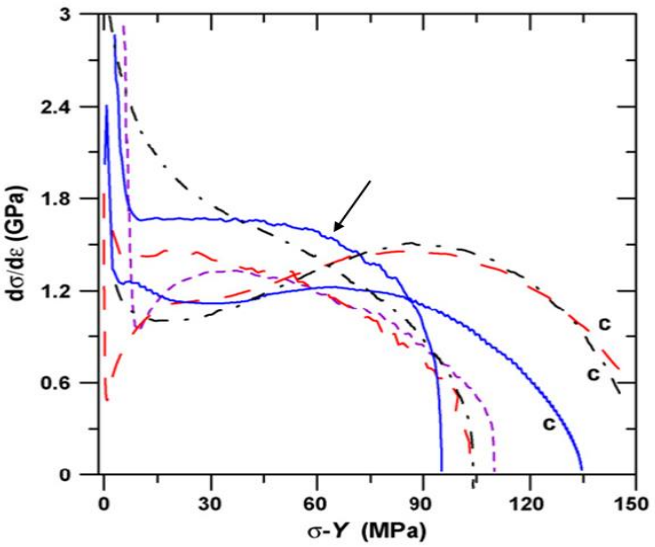

Figure 4: Work hardening rate a function of the difference between true stress and yield strength in pure cast Mg in compression (C) and tension [17].

2.6.1. Constitutive Equations and Work Hardening

True stress – true plastic strain relationships in metals can be modeled by several constitutive equations, including the Hollomon [48], Voce [49], Ludwik [50] and Swift [51] equations. These equations are given below.

Hollomon Equation:

$$\sigma = K_H \varepsilon_p^{\,n_H} \tag{4}$$

Voce Equation:

$$\sigma = \sigma_\infty - (\sigma_\infty - \sigma_0) e^{-K_V \varepsilon_p} \tag{5}$$

Ludwik Equation:

$$\sigma = \sigma_L + K_L \varepsilon_p^{\,n_L} \tag{6}$$

Swift Equation:

$$\sigma = K_S (\varepsilon_p + \varepsilon_S)^{n_S} \tag{7}$$

Note that the Hollomon equation has two parameters while the others have three parameters that need to be estimated.

In cast Al alloys, Stage III work hardening rate was found to decrease linearly with true stress, which represents the Kocks - Mecking (KM) work hardening model [52,53]:

$$\Theta = \frac{d\sigma}{d\varepsilon_p} = \Theta_0 - K\sigma \tag{8}$$

where Θ_0 is the initial work hardening rate and K is the KM parameter. Note that cast pure Mg shown in Figure 4 does not exhibit a region in which Θ decreases linearly with true stress.

Characteristics of tensile deformation can be used as a tool to assess the structural integrity of castings. In castings, work hardening rate analysis has been used [14] to characterize structural quality; when Θ was plotted versus σ in cast aluminum alloys, a sudden drop was observed just prior to fracture [15]. Fractographic analysis showed that this sudden drop could be attributed to major casting defects. In specimens with higher structural quality (no major defects), there was no sudden drop in Θ and deformation continued past the intersection of the curves for Θ and σ. The KM parameter K has a profound effect on elongation, as shown in Figure 5. With increasing K, elongation was found to decrease in A206-T7 aluminum alloy castings [16]. Also there is a sudden decrease in Θ just prior to final fracture.

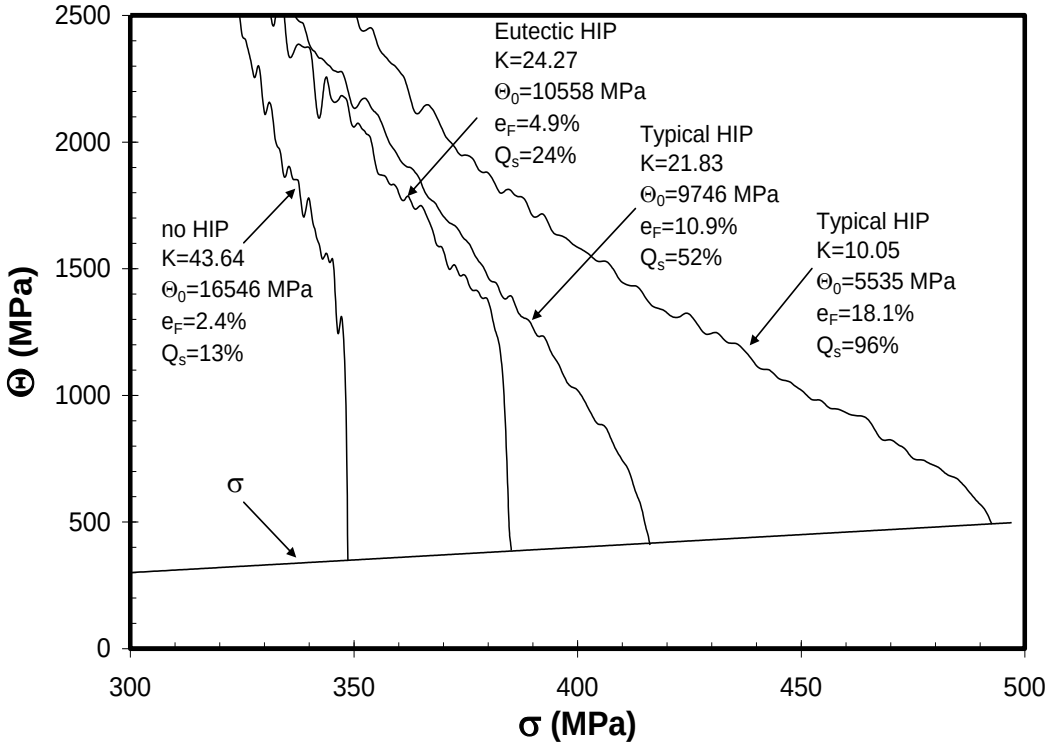

Figure 5: Change in Stage III work hardening characteristics with structural quality [16].

Based on the findings shown in Figure 5, Tiryakioğlu et al. [16] explained schematically how work hardening behavior is affected with structural quality, as presented in Figure 6. When the castings are free from defects, Stage II continues uninterrupted until the Considere criterion is met, without a sudden drop in work hardening rate.

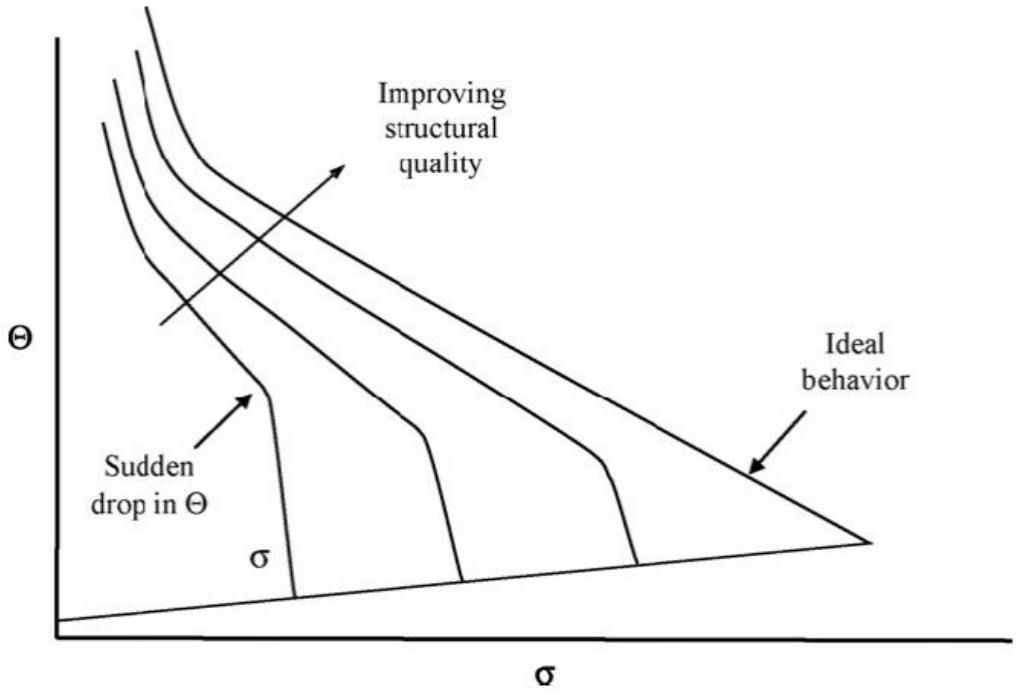

Figure 6: Schematic illustration of the change in work hardening behavior in cast Al alloys with structural quality and ideal behavior in the absence of structural defects [16].

2.7. Concept of Ductility Potential and Quality Index

Among all mechanical properties, low ductility is the most prominent symptom of the presence of major structural defects [54]. That is why effort to increase ductility by changing heat treatment, a practice promoted in traditional metallurgy books as strength-ductility trade-off, has been often been fruitless [55]. A more effective strategy to

increase ductility is to improve the initial melt quality, eliminate liquid metal transfers and design the filling system carefully so that additional oxide bifilms are not entrained [12,54].

The use of elongation as a measure of the structural quality of aluminum castings was proposed by Tiryakioglu *et al.* [56]. Comparison of current elongation to defect-free elongation, estimated from work hardening characteristics was proposed as a quality index. However, structural defects affect the work hardening characteristics significantly in cast aluminum alloys [14,16]. Therefore, using work hardening characteristics [15] of specimens with defects to estimate defect-free properties was found [54] to significantly underestimate $e_{F(max)}$. Subsequently, Tiryakioglu *et al.* used hundreds of data points from the aerospace and premium castings literature for Al-7Si-Mg [55], A206 [57] and A201 [58] to estimate $e_{F(max)}$. Because yield strength is minimally affected by structural defects, it is plotted in the x-axis with e_F on the y-axis. The elongation-yield strength plot for cast Al-7%Si-Mg alloys is presented in Figure 7 [59].

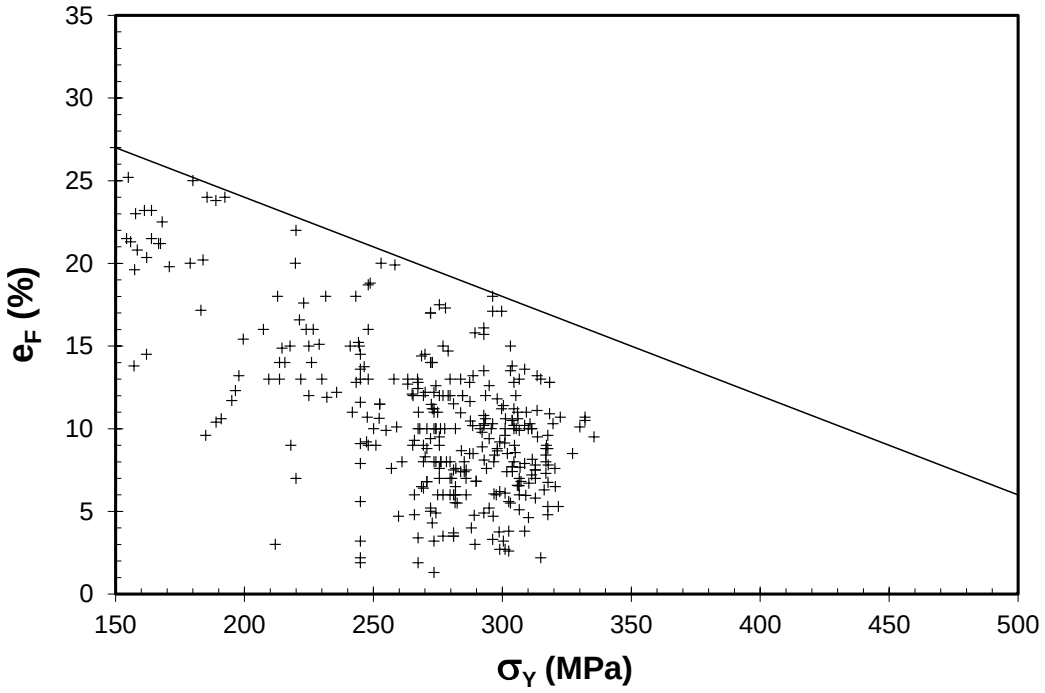

Figure 7: Elongation plotted versus yield strength for cast Al-7%Si-Mg alloys [59]

Note that there is a linear relationship between σ_y and the maximum levels of elongation. Hence maximum possible elongation or ductility potential, e_F, can be expressed [59] as;

$$e_{F(max)} = \beta_0 - \beta_1 \sigma_y \qquad (9)$$

where β_0 and β_1 (MPa^{-1}) are alloy-dependent coefficients, which are presented in Table 5.

Table 5: **The coefficients of Equation 9 for Al-7%Si-Mg, A201 and A206 alloys [60].**

	β_0	β_1 (MPa^{-1})
A356-357	36.0	0.064
A201	34.5	0.047
A206	47.8	0.085

The ductility potential developed for each alloy family can be used as a metric to compare elongation to ductility potential. Therefore, the quality index, Q_T, can then be found by [59];

$$Q_T = \frac{e_F}{e_{F(max)}} = \frac{e_F}{\beta_0 - \beta_1 \sigma_Y} \tag{10}$$

The concept of Q_T is shown schematically in Figure 8.

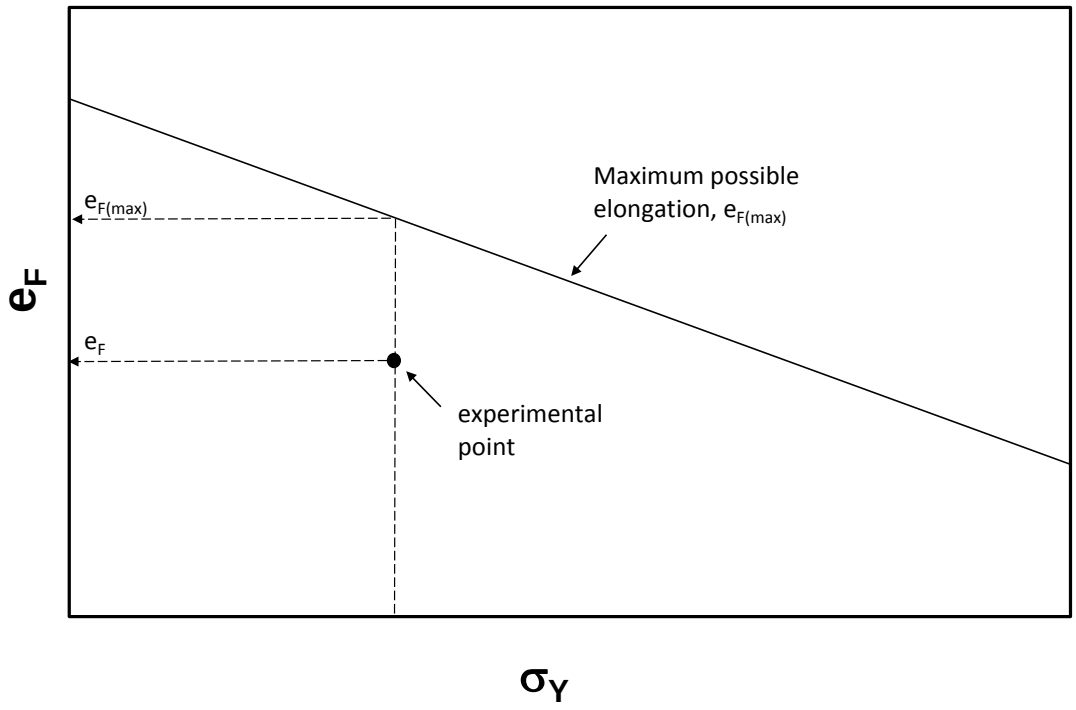

Figure 8: Schematic illustration of the use of the ductility potential to assess structural quality [59].

Tiryakioglu and Campbell [59] have recently suggested that there are three regions for Q_T: (1) Q_T is below 0.25, (2) Q_T is between 0.25 and 0.70, and (3) Q_T is above 0.70. Region 1, premature fracture is due to "old", coarse oxide bifilms which are typically the skin of ingots. In this region, engineers need to focus on melt quality to

eliminate old oxides from remelts. Chilling the melt can increase the quality marginally. In Region 2, the molten metal which is free from major "old" oxides but there are "young" oxide bifilms in the beginning of the process which can increase the properties of the metal. When Q_T is above 0.70, every small detail of the melt preparation and mold filling system design needs to be reviewed. In this region, chilling, i.e., decreasing dendrite arm spacing (DAS) has no effect on elongation [12]. For all three regions, Tiryakioglu and Campbell proposed specific quality improvement efforts.

2.8. Effect of Casting Defects on Tensile Properties in Cast Mg Alloys

Tensile deformation is cast Mg alloys with defects has been investigated recently [61,62,63]. Song *et al.* conducted *in situ* experiments in die cast AM50 alloys and observed how the material around pores and bifilms deforms in tension. Only after stress exceeds yield stress, there was noticeable deformation around pores and bifilms. Song *et al.* also stated that (i) the final fracture is probably not due to cracking and/or decohesion of the β-phase ($Mg_{17}Al_{12}$) and (ii) the alloy could withstand large amount of plastic deformation before fracture although the presence of structural defects reduced the elongation to only 6%. For the same alloy, Lee *at al.* [64] found a strong correlation between elongation and area fraction of porosity on the fracture surface. The fracture path was observed to go through the regions of clusters of structural defects. Lee *et al.* stated that the defect-free elongation for the alloy with $\sigma_y \approx 120$MPa should be 29%. Weiler and Wood investigated the effect of pores on the elongation and tensile strength of AM60B alloy castings via experimentation [62] and finite element modeling. As can be expected, they found that elongation is reduced significantly with increasing size of pores. They also attempted to estimate elongation when the area fraction of pores is zero, i.e., when

the specimen is defect-free, by extrapolating the elongation-area pore fraction relationship to zero pores. For a specimen with $\sigma_y \approx 130$ MPa, they estimated the defect-free elongation $e_{F(max)}$, to be 10%. A similar approach was taken by Lee and Shin [65] and Lee [66] for AZ91 alloy castings. In these studies, elongation was correlated to the level of microporosity [65] and grain size [66]. Lee and Shin developed a critical strain model, which predicted $e_{F(max)}$ to be between 6 and 10% for σ_y=125 MPa, which agrees with the results of Weiler and Wood. Lee [66] extrapolated elongation-area pore fraction relationships for various grain sizes and found that for σ_y=125 MPa, defect-free elongation can be estimated as:

$$e_{F(max)} = 13.6 \exp(-1.3 \times 10^{-3} d) \tag{11}$$

Lee also suggested that the effect of grain size on elongation should become less pronounced with decreasing level of porosity.

2.9. Statistics for Fracture

To model fracture, Weibull [67,68,69] developed a distribution, based on the weakest link theory which was introduced earlier by Pierce [70]. Weibull distribution can be presented as:

$$P = 1 - \exp\left[-\left(\frac{\sigma - \sigma_T}{\sigma_0} \right)^m \right] \tag{12}$$

where P is the probability of failure at a given stress, σ, or lower, the threshold value, σ_T, is the value below which no specimen is expected to fail. σ_0 is the scale parameter, m is the shape parameter which refers to the Weibull modulus. Weibull found that this theory can be applied to fracture of ceramics and metals. Largest defects act as the weakest link by raising the local stresses and resulting in premature fracture. Since the main reason

behind the drop in mechanical properties address the structural defects, it is suitable to state that fracture-related mechanical properties such as fracture stress, elongation, fracture toughness, fatigue life can be analyzed with the concept of defect-size distribution [71, 72].

The probability density function, f, for any continuous distribution can be written as:

$$f = \frac{dP}{d\sigma} \tag{13}$$

For the Weibull distribution, f can be written as:

$$f = \frac{m}{\sigma_0}\left(\frac{\sigma-\sigma_T}{\sigma_0}\right)^{m-1} \exp\left[-\left(\frac{\sigma-\sigma_T}{\sigma_0}\right)^{m}\right] \tag{14}$$

Weibull probability plot is the most common way to apply Weibull fits to data. Equation 12 can be rearranged in to Equation 14 which can be expressed as:

$$\ln\left[-\ln(1-P)\right] = m\ln(\sigma-\sigma_T) - m\ln(\sigma_0) \tag{15}$$

This equation is linear when the left side of the equation is plotted versus $\ln(\sigma-\sigma_T)$ with a slope of m and an intercept of $-m \ln(\sigma_0)$. This probability plot can also be obtained when the same side of the equation is plotted versus $\ln(\sigma)$ [73].

Tiryakioglu and Campbell [74] provided Weibull probability plots for 3-parameter Weibull distribution and Weibull mixtures. They noted that 2-parameter Weibull distribution is applicable when castings have defects which were introduced into the melt during the mold filling, from one source of damage. They noted that, in this case, $\sigma_T=0$ for 2-parameter Weibull distributions. Therefore Equation 15 can be written as;

$$\ln\left[-\ln(1-P)\right] = m\ln(\sigma) - m\ln(\sigma_0) \tag{16}$$

A relationship between *m* in 2-parameter Weibull distributions of fracture strength and the metal quality has been expressed by Campbell [75]. For pressure die casting m is usually between 1 and 10, for gravity-filled castings it is between 10 and 30, for high quality aerospace castings it is in range from 50 to 100.

CHAPTER 3: APPLICATION OF THE QUALITY INDEX APPROACH FOR MG ALLOY CASTINGS

The approach taken by Tiryakioğlu and coworkers has been applied to Mg alloy castings by collecting large numbers of tensile data from the literature and analyzing elongation versus yield strength. A copy of the paper that was published as a result of the investigation is given in Appendix I.

All data collected from literature are presented in Figure 9. Note that there are many specimens at low ductility levels (<5%), especially when yield stress exceeds 100 MPa. Therefore, it is easy to understand why low ductility is assumed to be intrinsic in Mg castings. Figure 9 also shows that for a particular level of yield strength, number of data points becomes sparse with increasing elongation. The number of points that can be considered maximum at any given yield strength level is approximately twenty five. Therefore, less than 2% of all data included in this study represent maximum elongation values.

In, maximum points seem to have linear trend with yield strength, similar to what was reported for Al alloy. The line that goes immediately above all maximum points follows Equation 1;

$$e_{F(max)}\,\% = 41.8 - 0.106\sigma_Y \qquad (1)$$

The line represents the true ductility potential of cast Mg alloys. It also represents the true (intrinsic) trade-off between ductility and strength, commonly referred to in metallurgy textbooks.

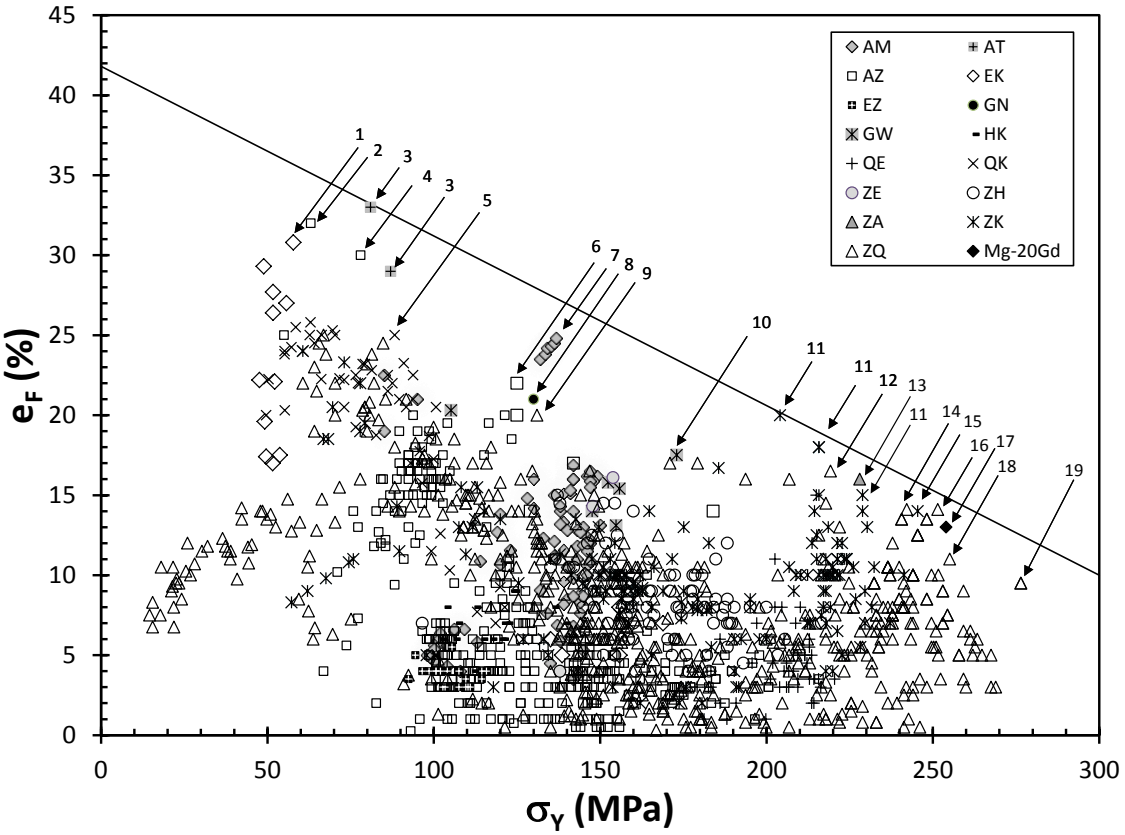

Figure 9: Ductility Potential of various Mg alloy families [13].

It is noteworthy that there are data from almost all Mg alloy systems near the true ductility potential line. While alloying additions affect the strengthening mechanisms to reach the desired yield strength, the maximum elongation at that particular yield strength is independent from the chemical composition of the alloy. This result has significant implications for the selections of Mg alloys for particular applications and/or future Mg alloy development effort, because the same strength and elongation can be obtained by different alloying additions. As an example, at σ_y=235MPa in Figure 9, there are two data points just below at line, one from the ZK (Mg-Zn-Zr) alloy family and the other from the ZQ (Mg-Zn-Ag) alloy family. Although they have almost the same strength and elongation, the cost for the two alloys can be expected to be vastly different because of

the silver addition in the ZQ series. Hence significant cost savings can be achieved by selecting a less expensive alloy and careful design of process to minimize structural defects.

In addition, it was shown by the author that there are almost all alloy families around the line. Casting geometry and size include plate, separately-cast tensile bars, ingot, and actual premium and aerospace castings. Hence, it can be stated that maximum elongation can be reached for any casting shape and size. Specimens with different heat treatment conditions, produced via various casting process can reach the maximum elongation levels. A significant result of the study is grain size of specimens near the true ductility line shows ranges between 10 and 163μm. Hence, there is strong evidence that grain size has no effect on ductility when castings are free from structural defects.

The ductility potential line can be used to assess the structural quality of all Mg alloy castings by using Equation 1. Therefore, Q_T can be used as a metric during any effort to improve the structural quality and hence the performance of Mg alloy castings.

To examine the relationship between various Mg alloy castings on the ductility potential line, points around the line were examined more closely, the details of which are provided in Table 6.

Table 6: Detailed information about data indicated in Figure 9 [13].

Point	Alloy	Temper	d (μm)	Process	Casting
1	EK11	F	30	Permanent mold casting	5 mm diameter, 25 mm length
2	AZ31	F	-	Copper mold	150 mm diameter, 200 mm length
3	AT33	F	55	Copper mold	60 mm × 40 mm × 12 mm
4	AZ31	F	163	Copper mold with electromagnetic stirring	150 mm diameter, 200 mm length
5	QK71	T6	71	Green sand casting	13 mm diameter cast tensile bars
6	AZ91	W	125*	Sand casting	200 mm×100 mm×15 mm plate
7	AM60	F	10*	Intensively sheared melt, high pressure die casting	6.4 mm diameter bars
8	GN112	W	70*	Permanent mold casting	70 mm×50 mm×20 mm plate
9	ZQ33	T6	90*	Green sand casting	13 mm diameter cast tensile bars
10	GW63	F	25	High vacuum die casting	6.3 mm diameter tensile bars
11	ZK61	T6	76	Green sand casting	25.4 or 50.8 mm-thick rectangular plates with chills
12	ZQ71	T6	81	Green sand casting	25.4 or 50.8 mm-thick rectangular plates with chills
13	ZA81	T6	80	Permanent mold casting	Ingot
14	ZQ64	T6	-	Permanent mold casting	Aerospace casting
15	ZK61	T6	-	Green sand casting	13 mm diameter cast tensile bars
16	ZQ71	T6	-	Permanent mold casting	Aerospace casting
17	Mg-20Gd	F	80	Copper mold	70 mm×40 mm×9 mm ingot
18	ZQ91	T6	25	Green sand casting	13 mm diameter cast tensile bars
19	ZQ64	T6	-	-	12 kg premium quality casting

The details in provided in Table 1 have several implications:

1. As mentioned previously, there are data from almost all alloy families around the line.
2. Casting geometry and size include plate, separately-cast tensile bars, ingot, and actual premium and aerospace castings. Hence, it can be stated that maximum elongation can be reached for any casting shape and size.
3. Specimens with different tempers, produced via various casting processes can reach the maximum elongation levels.
4. Table 6 shows that grain size of specimens near the true ductility line shows ranges between 10 and 163 μm. Hence, there is strong evidence that grain size has no effect on ductility when castings are free from structural defects.

That grain size has no effect on the ductility potential is consistent with the finding in cast Al-7%Si-Mg alloys that SDAS, similarly, does not affect $e_{F(max)}$. Although Lee [66] has been correct to state that the effect of grain size on elongation is lessened with increasing quality, the results in the present study suggest that the effect of grain size on elongation disappears completely as elongation approaches $e_{F(max)}$. If grain size is taken as a measure of the local solidification time, then, in the absence of bifilms, the heterogeneous nucleation sites for pores and intermetallics do not exist, resulting in defect-free castings, regardless of how long it takes for the castings to solidify. Moreover, cracking along grain boundaries is not expected to occur as easily during tensile deformation when bifilms (and intermetallics) are not on grain boundaries. Although grain boundaries are usually assumed to be weak and consequently cracking along them is considered normal, recent research [76] on bicrystals has shown that the

strength of grain boundaries, when inclusions and impurities are not present, approaches the theoretical strength of monocrystals. Hence cracking along grain boundaries during tensile deformation and a "beneficial" effect of grain refining should be taken as symptoms of a high density of bifilms in the structure. This point has been suggested by Campbell [41] to explain the true "grain refining" effect of Zr, a common alloying addition in Mg alloys, by the sedimentation of bifilms to the bottom of the melt.

Along the same lines as grain size, the effect of section thickness should be reevaluated. Hu et al. [77] stated that yield strength and elongation decrease with section thickness, i.e., solidification time. However, when attention was paid to every detail of the casting process, Lagowski and Meier [7878] reported that section thickness had no effect on the ductility of Mg alloys.

Turning our attention to past efforts to estimate defect-free elongation, Equation 11, developed for σ_Y=125 MPa, can be compared with Equation 1. Taking the two extreme grain size values in Table 9, 10 and 163 μm, Equation 11 yields 13.4% and 11.0% elongation for the defect-free condition. These numbers are significantly lower than $e_{F(max)}$ = 28.6% found by using Equation 1 for the same yield strength. Hence Equation 11 underestimates $e_{F(max)}$ significantly. The same conclusion can be made for the estimates of $e_{F(max)}$ made by Weiler and Wood [62] and Lee and Shin [65]. The estimate, $e_{F(max)}$ = 29%, provided for Lee et al. [64] at $\sigma_Y \approx 120$ MPa, is almost identical to the outcome of Equation 1 (29.1%).

CHAPTER 4: EXPERIMENTAL PROCEDURE

4.1. Alloy

For this study, the AZ91D magnesium alloy has been selected. Chemical composition for AZ91D is given in Table 7. Specimens which have been selected for this study were carried out with T4 and T6 conditions.

Table 7: Chemical composition in (wt. %) of AZ91D Mg alloy used in this study.

Al	Zn	Mn	Si	Fe	Cu	Mg
9.2	0.7	0.3	0.03	0.003	0.001	Balance

4.2. Tensile Testing

Sand cast tensile bars produced in ASTM B108 sand molds (Figure 10) with 12.7 mm diameter were received from a magnesium casting supplier in T4 and T6 conditions. In the literature [79], it has been stated that AZ91 Mg alloys for the T4 condition follows the heat treatment procedure which is; 415^{o}C for 16 to 24 hours and maximum heat treating temperature is 418^{o}C. For T6, it is solution treating at 415^{o}C for 16 to 24 hours, maximum treatment temperature is 418^{o}C and aging at 168^{o}C for 16 hours.

Figure 10: ASTM B108 test bar mold.

These bars were subsequently machined into 6.35 mm diameter bars. The final geometry of tensile bar is presented in Figure 11. Sixty specimens in each temper were tested in tension at a strain rate of 10^{-3}/s. True stress and true strain values were obtained by assuming conservation of volume. The tensile machine used was Instron with an extansometer attached to the specimen throughout the tensile tensting. Extensometer gauge length was 25 mm. Data points were digitally recored at 10 data points per seconds.

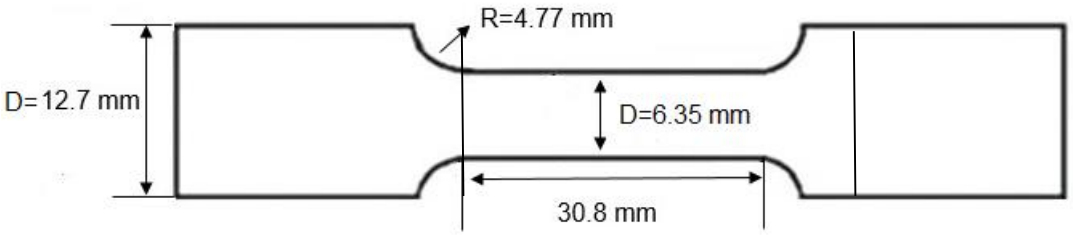

Figure 11: The geometry of tensile bar with dimensions.

For the microstructural analysis, specimens were polished with 240μm, 360μm, 600μm, 800μm and 1200μm grit silicon carbide (SiC) paper. This procedure followed by 1μm, 0.3μm and 0.5μm alumina (Al_2O_3) suspensions.

Specimens with highest and lowest quality index were selected from both tempers. Samples were sectioned and prepared for electron microscope. Fracture surfaces of selected specimens were analyzed with a JEOL Scanning Electron Microscope (SEM) at the University of Florida. Composition of observed intermetallic particles or interfaces were provided with Energy Dispersive Spectometer (EDS) which was mounted in the SEM column.

CHAPTER 5: RESULTS AND DISCUSSION

The microstructure of the AZ91 castings used in this study is provided in Figure 12. Grain size of the specimens have been calculated with the intercept method [80]. It can be seen from the Figure 12 that the grain size of the specimens are in range of 120-150μm according to ASTM E112-13 [80]. Dots were present due to the polishing procedure of the samples.

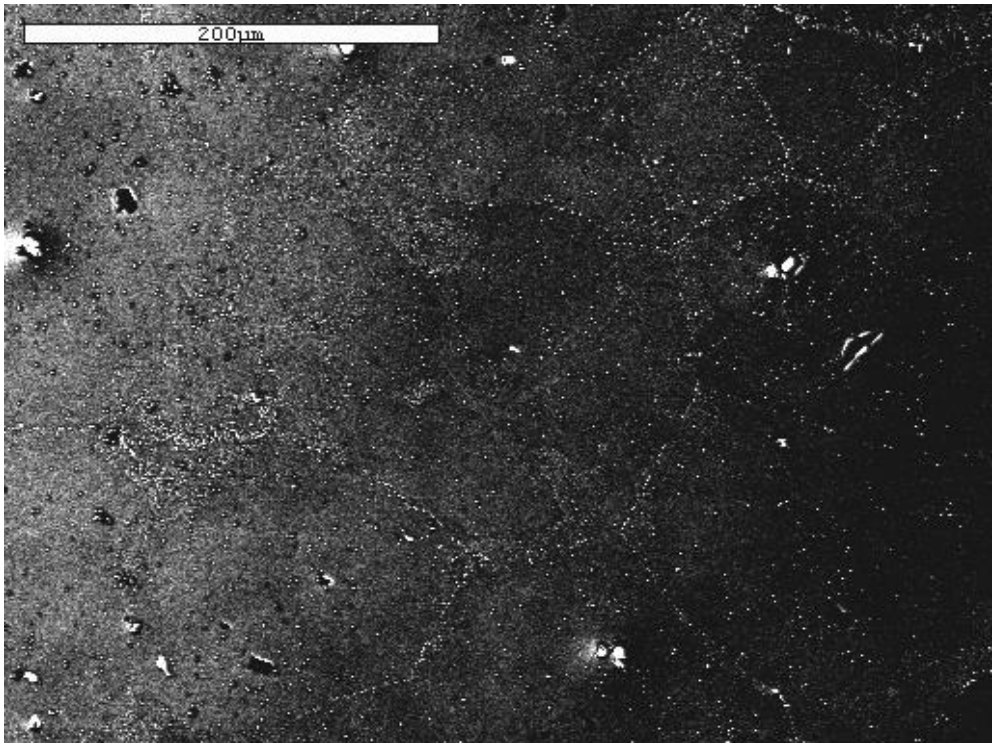

Figure 12: Microstructure of AZ91D specimen.

Yield strength, elongation, tensile strength, quality index and toughness, i.e, the area under the true stress-strain curve, were obtained by tensile testing for T4 and T6 specimens. Results are presented in the Table 8.

Table 8: Tensile data for T4 and T6 conditions.

T4						T6					
No.	**σ_y (MPa)**	**S_T (MPa)**	**e_F (%)**	**Ψ (MJ/m^3)**	**Q_T**	**No.**	**σ_y (MPa)**	**S_T (MPa)**	**e_F (%)**	**Ψ (MJ/m^3)**	**Q_T**
1	91.16	274.36	13.68	30.69	0.43	1	126.94	271.47	5.27	12.51	0.19
2	92.22	273.06	13.62	30.39	0.43	2	124.47	267.56	5.38	12.68	0.19
3	97.99	287.13	14.54	34.29	0.46	3	126.30	283.95	6.86	16.79	0.24
4	82.06	269.46	11.52	24.95	0.35	4	125.79	287.02	7.32	18.14	0.26
5	90.05	282.90	16.77	39.50	0.52	5	136.34	265.71	4.20	10.03	0.15
6	80.40	266.91	11.86	25.44	0.36	6	141.77	282.87	4.58	11.61	0.17
7	80.88	269.99	13.62	29.72	0.41	7	124.81	271.50	6.12	14.34	0.21
8	82.63	276.65	15.26	34.78	0.46	8	136.18	292.95	7.58	19.32	0.28
9	83.33	283.68	15.64	36.61	0.47	9	136.54	289.29	5.36	13.71	0.20
10	87.17	278.95	15.88	36.28	0.49	10	141.46	276.48	4.52	11.21	0.17
11	72.52	277.39	14.34	32.52	0.42	11	122.74	280.01	5.89	14.32	0.20
12	87.42	278.64	13.68	30.90	0.42	12	99.86	254.58	4.49	9.98	0.14
13	85.53	276.67	15.18	34.60	0.46	13	145.87	266.36	3.28	8.08	0.12
14	76.50	253.70	15.05	31.51	0.45	14	118.82	264.55	5.10	11.76	0.17
15	105.30	282.21	14.30	33.57	0.47	15	122.20	270.60	5.78	13.49	0.20
16	89.07	290.39	16.11	38.84	0.50	16	136.83	266.06	2.85	6.93	0.10
17	85.69	272.44	14.19	31.50	0.43	17	116.05	262.15	2.93	6.99	0.10
18	86.49	274.24	13.81	30.85	0.42	18	119.05	257.51	5.48	12.11	0.19
19	88.97	282.39	16.68	39.01	0.52	19	115.88	275.53	6.85	16.12	0.23
20	96.35	282.29	13.27	30.12	0.42	20	129.39	281.11	6.98	17.13	0.25
21	99.07	275.37	10.84	24.12	0.35	21	119.86	273.49	6.41	15.17	0.22
22	97.51	290.82	13.98	33.49	0.44	22	124.10	296.52	8.67	22.28	0.30
23	90.87	287.04	15.67	37.21	0.49	23	133.62	299.28	7.81	20.24	0.28
24	91.30	283.96	14.71	34.41	0.46	24	136.71	278.47	4.25	10.57	0.16
25	86.93	271.74	12.92	28.17	0.40	25	142.90	297.93	5.82	15.43	0.22
26	95.27	278.71	14.81	33.80	0.47	26	163.74	280.05	3.28	8.35	0.13
27	91.16	287.04	11.32	24.23	0.35	27	124.71	293.76	8.00	20.42	0.28
28	93.32	261.79	10.01	21.20	0.31	-	-	-	-	-	-

For T4, yield strength of specimens range from 80.40 MPa to 105.30 MPa and elongation ranges from 9.43% to 16.15%. By using elongation data and ductility potential of each specimen, quality index is calculated. Results range from 0.30 to 0.50 for T4 specimens. This means that T4 specimens used in this study are in Region 2 quality index which indicates that specimens are free from old bifilms but there are young bifilms introduced into the molten metal.

In Figure 13, the relationship between toughness and elongation is presented. Hence, there is a strong correlation between toughness and elongation for cast AZ91D specimens, as indicated by high values of coefficient of determination, R^2. This result is consistent with results reported previously for cast Al alloys [16,81].

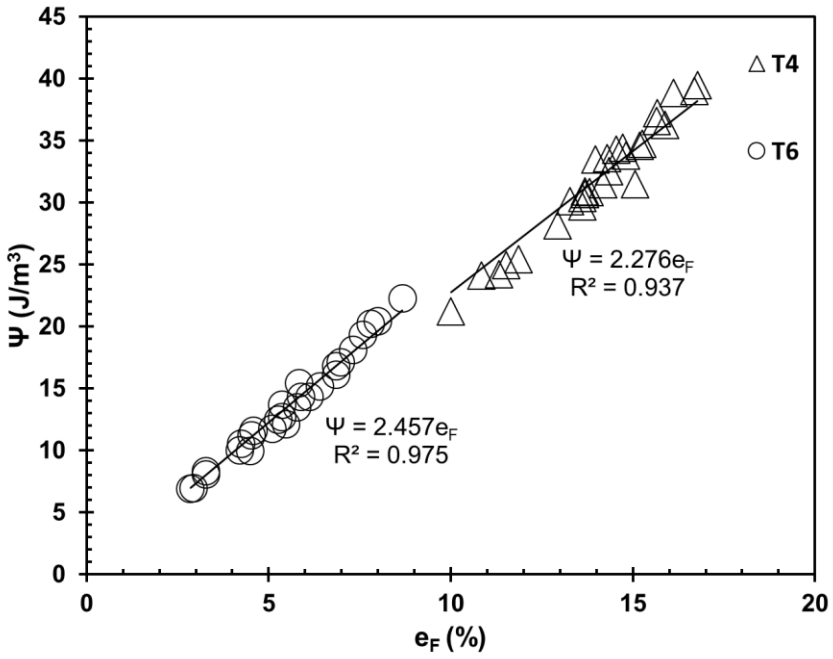

Figure 13: Relationship between toughness (Ψ) and elongation (e_F%) for both conditions.

For T6, yield strength of specimens ranges from 99.86 MPa to 163.61 MPa and elongation of each specimen ranges from 2.30% to 8.43%. By using elongation and ductility potential of each specimen, quality index is calculated. Results range from 0.08 to 0.23. This means specimens used in this study are in region 1 quality index which indicates that melt quality needs to be focused and old oxide bifilms need to be eliminated.

Figure 14 shows the dot plot for the quality index of both heat treatment conditions. In Chapter 3, it was stated that heat treatment did not affect ductility potential. The experimental results from T4 and T6 specimens, however, suggest that the aging does indeed affect Q_T, as presented in Figure 14. Specimens in T4 have clearly higher quality index. Because castings were produced from the same heat, it is not realistic to attribute the difference in Q_T between the two tempers to any structural quality issue. To determine the reason for this discrepancy, a detailed analysis of the work hardening behavior in the two conditions is necessary.

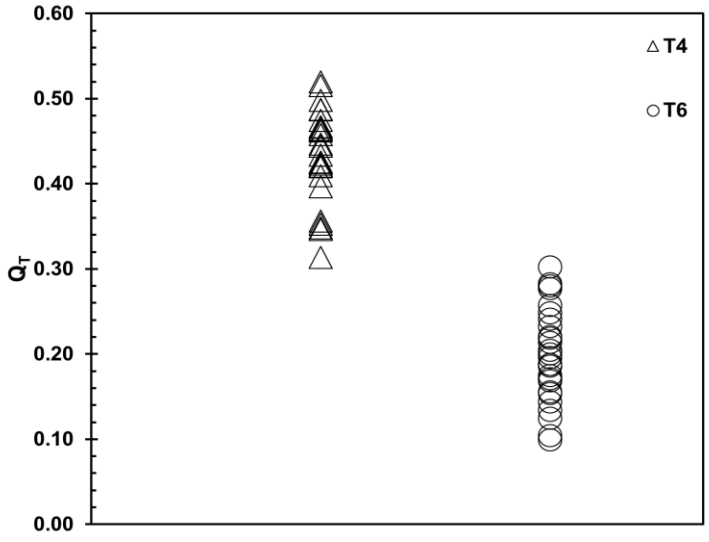

Figure 14: Dot plot analysis of Q_T data for T4 and T6 specimens.

In order to characterize the statistical distribution of Q_T values in both conditions, Weibull distributions have been fitted to the quality index results by using the maximum likelihood method. Estimated Weibull parameters are provided and Weibull probability plots are presented in Figure 15. Linear trends for T4 and T6 conditions in their Weibull probability plots indicate two parameter distributions, i.e., the threshold values are zero. Note in Table 9 that for both tempers R^2 is in excess of the critical value, $R^2_{0.05}$ for corresponding sample sizes [73], indicating that Weibull fits cannot be rejected.

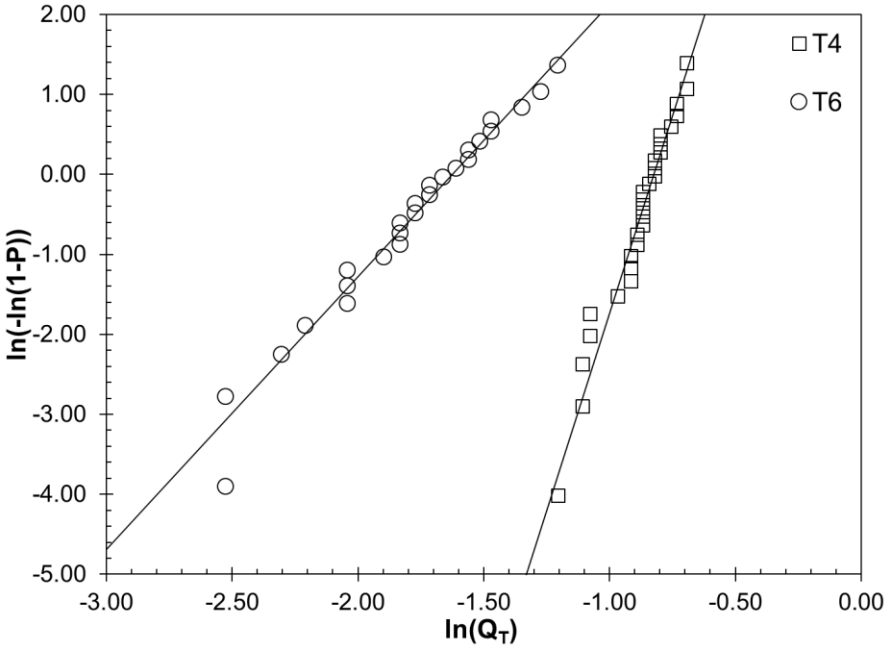

Figure 15: Weibull probability plots for Q_T for both conditions.

Table 9: Estimated Weibull parameters for Q_T data.

			Parameter Estimates			Goodness of Fit		
Alloy	Temper	n	σ_0 (MPa)	σ_T (MPa)	m	$R^2_{0.05}$	R^2	Weibull?
AZ91D	T4	28	0.4386	0	9.874	0.909	0.951	Yes
	T6	27	0.1969	0	3.411	0.913	0.972	Yes

The probability density functions for the Weibull distributions for T4 and T6 specimens are presented in Figure 16. The upper distribution of T4 specimens is located at higher values of quality index than T6 specimens. Note that Weibull distributions of two sets are significantly apart from each other. This difference is hypothesized to be due to differences in the work hardening characteristics between T4 and T6 specimens.

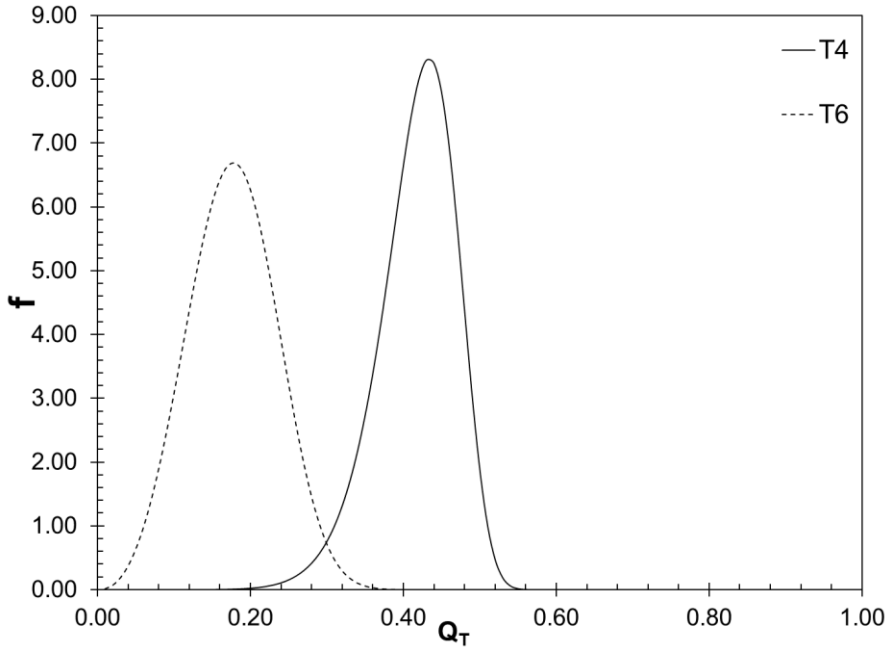

Figure 16: Weibull probability plots for Q_T for both conditions.

5.1. Tensile Deformation

The performance of the four constitutive equations are listed in Table 10 in modeling the work hardening behavior of AZ91D cast magnesium alloy was assessed by using tensile data from specimens in T4 and T6 conditions. Moreover, the work hardening characteristics in T4 and T6 were characterized by using $\sigma - \Theta$ charts. The σ - ε_p curves of the specimens with highest and lowest elongation selected for this study are presented in Figure 17. The specimens with highest elongation had yield strength (σ_y) of 90.4 and 124.6 MPa and elongation (e_F) of 16.2 and 8.0% for T4 and T6 conditions in

Figure 17-a and the specimens with lowest elongation had the yield strength (σ_y) of 93.32 and 145.87 MPa and elongation (e_F) of 10.01% and 3.28% for T4 and T6 conditions in Figure 17-b, respectively.

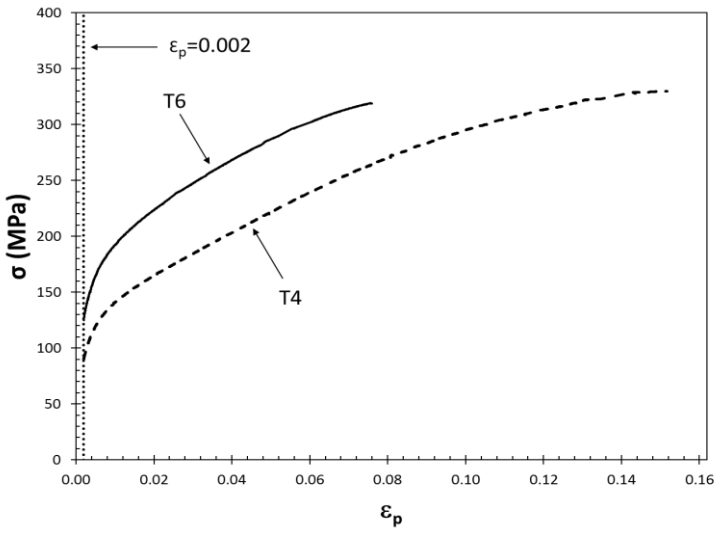

(a)

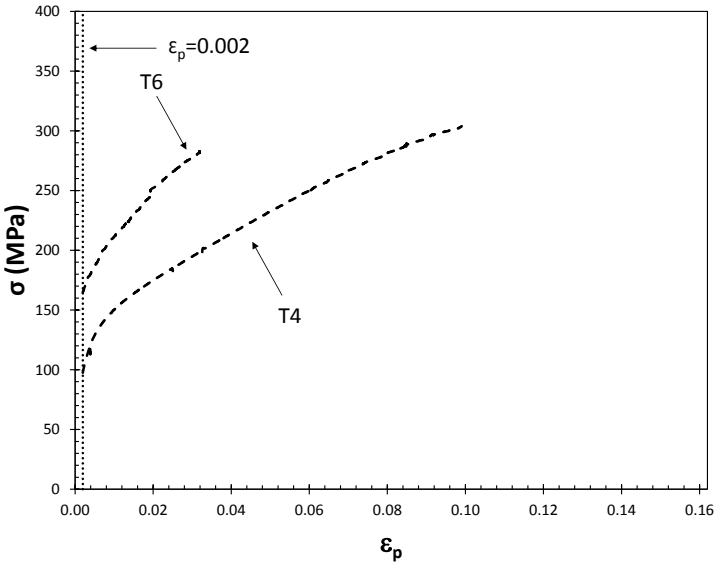

(b)

Figure 17: True stress – true plastic strain curves for specimens with (a) highest and (b) lowest elongation in both tempers.

True-stress-true plastic strain data in the plastic region of the specimens with highest elongations were used to determine how well the four constitutive equations (Equations 4-7). To find the best fits, Newton-Raphson method was used to minimize the root mean square error (RMSE), which can be calculated as:

$$RMSE = \sqrt{\frac{\Sigma_{t=1}^{n}(y_t - y)}{n - a}} \tag{17}$$

where a is the number of parameters to be fitted and n is the specimens number. The coefficient of determination, R^2,was also calculated for each fit;

$$R^2 = 1 - \frac{SS_{res}}{SS_{tot}} \tag{18}$$

where SS_{res} is sum of squares of residuals, SS_{tot} is total sum of squares for experimental data.

The values of the estimated parameters as well as RMSE and R^2 for each fit are presented in Table 10. Note that the R^2 values in each case is above 0.99 which shows that all constitutive equations included in this study can be used to characterize the true stress – true strain relationship in this alloy.

The derivative of the four constitutive equations were taken and rearranged so that Θ is only a function of σ. These work hardening rate equations are also provided in Table 11. Note that Equation 8 is identical to the work hardening rate for the Voce equation in Table 11, such that, $\Theta_0 = \sigma_\infty K_V$ and $K = K_V$.

Table 10: Estimated parameters for the constitutive equations for the two specimens and the RMSE and R^2 of each fit.

		T4			T6		
Equations	**Parameters**	**Estimate**	**RMSE (MPa)**	**R^2**	**Estimate**	**RMSE (MPa)**	**R^2**
Hollomon	**K_H (MPa)**	645.2	6.22	0.991	605.0	2.81	0.997
	n_H	0.346			0.250		
Voce	**σ_∞ (MPa)**	393.8	3.14	0.998	341.5	5.14	0.991
	σ_0 (MPa)	106.9			135.8		
	K_V	10.5			27.2		
Swift	**K_S (MPa)**	733.7	3.40	0.997	636.0	2.33	0.998
	ε_S	0.007			0.001		
	n_S	0.413			0.269		
Ludwik	**σ_L (MPa)**	68.5	3.51	0.997	54.7	1.99	0.999
	n_L	0.516			0.334		
	K_L (MPa)	729.4			628.2		

Table 11: True stress – true plastic strain work hardening rate as function of true stress for the four constitutive equations.

Constitutive Equations	**$\sigma = f(\varepsilon_p)$**	**$\Theta = f(\sigma)$**
Hollomon	$K_H \varepsilon_p^{\,n_H}$	$n_H \left(\frac{\sigma}{K_H}\right)^{\left(\frac{n_H-1}{n_H}\right)}$
Voce	$\sigma_\infty - (\sigma_\infty - \sigma_0)e^{-K_V \varepsilon_p}$	$K_V(\sigma_\infty - \sigma)$
Ludwik	$\sigma_L + K_L \varepsilon_p^{\,n_L}$	$n_L K_L \frac{(\sigma - \sigma_L)^{\left(\frac{n_L-1}{n_L}\right)}}{K_L}$
Swift	$K_S(\varepsilon_p + \varepsilon_S)^{n_S}$	$K_S n_S \left(\frac{\sigma}{K_S}\right)^{\left(\frac{n_S-1}{n_S}\right)}$

The change in Θ with the difference between true stress and yield stress ($\sigma-\sigma_y$) for the two specimens is presented in Figure 18. Note that curves with work hardening rates obtained by using the equations in Table 11 and estimated parameters in are also indicated. For the T4 specimen in Figure 18-a, all constitutive equations initially underestimate the work hardening rate. The Voce equation provides the best fit after approximately $\sigma - \sigma_y = 50$ MPa. All constitutive equations provide almost identical fits for $\sigma-\sigma_y \geq 100$ MPa. For the T6 specimen in Figure 18-b, Hollomon, Swift and Ludwik equations give similar fits that closely follow the work hardening rate curve. The voce equation does not provide a good fit especially at lower stress levels.

It is noteworthy that the T4 specimens exhibited first a steep decrease in work hardening rate, due to a short elastoplastic transition, followed by a plateau in work hardening rate, indicated as Stage II. Consequently, there is a region in the true stress – true plastic strain curve in Figure 17 where true stress increases linearly with strain, approximately between true stress levels of 150 and 250 MPa. For the T4 specimen, Stage II work hardening is followed by Stage III in which work hardening rate decreases linearly with stress. The presence of a Stage II with constant work hardening rate was reported for pure Mg [17] and several Mg alloys [82,83]. Note that Θ is 1850 MPa in Stage II in Figure 18-a, which is similar to the levels reported for pure Mg [17] and equal channel angular pressed (ECAP) AM60 alloy [82].

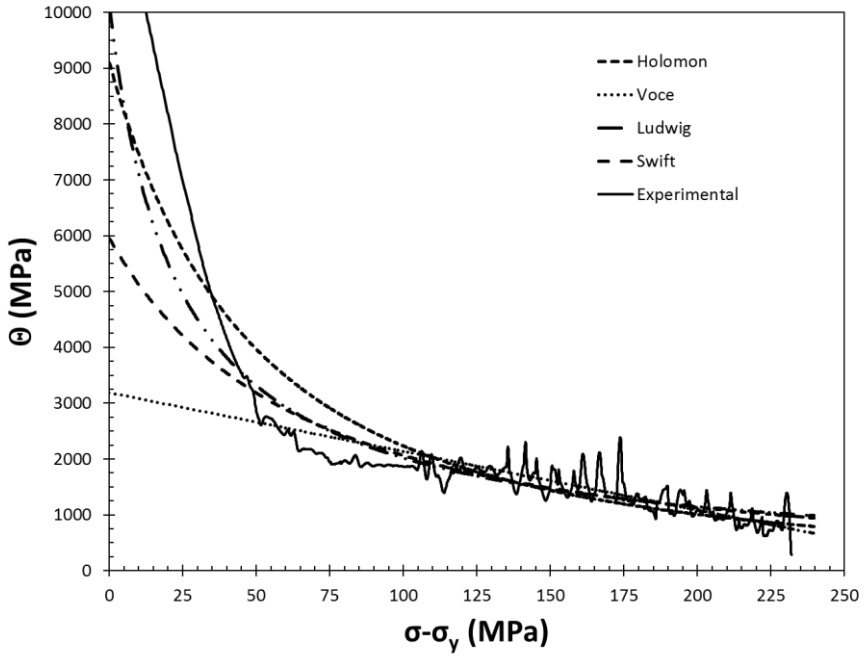

(a)

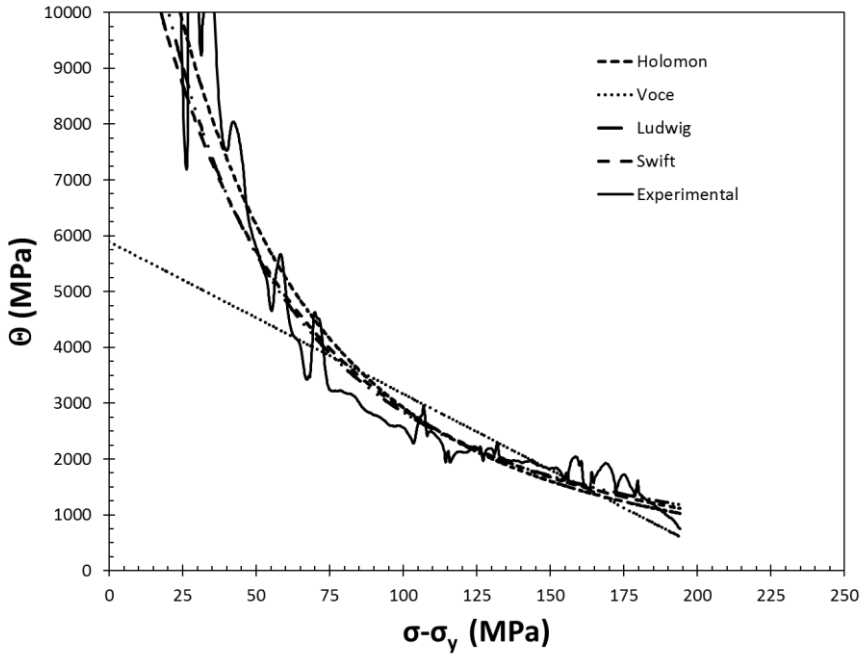

(b)

Figure 18: Kocks – Mecking diagram and plots of work hardening rate calculated from derivation of constitutive equations for (a) T4 and (b) T6 [84].

5.2. Kocks – Mecking Analysis

The work hardening rate in two specimens with highest elongation as a function of σ-σ_Y is presented in Figure 19. Note that in both specimens, there is a distinct Stage III work hardening region in Θ decreases linearly with increasing stress, following Equation 8. For the T4 specimen, Θ_0=4,827 MPa and K=12.8. For the T6 specimen, Θ_0 and K are 5709 MPa and 14.1, respectively.

The result for the T4 and T6 specimens are contradictory in how the four equations perform. Among the four equations, only Voce equation is based on the evaluation of the dislocation density with plastic deformation, developed by Kocks and Mecking [52,53]. Merely fitting the four constitutive equations to the stress – strain data past yield strength is not sufficient to characterize the plastic deformation behavior in this alloy.

The results of the Kocks-Mecking analysis for all specimens are given in Table 12. A plateau in work hardening rate at 1800 MPa (~E/25) is observed for T4 specimens. The presence of a plateau and its value is consistent with the results of Caceres and Blake [17] as presented in Figure 4. This region was stated as Stage II. It must be noted that the constant Stage II work hardening is only observed for T4 specimens. In T6 specimens, there is no plateau with a constant work hardening rate. This is the first time that the absence of this plateau is reported for Mg alloys. Moreover in both T4 and T6 specimens, there is a region in which work hardening rate decreases linearly with true stress, following the Kocks-Mecking Stage III work hardening model. Therefore the work hardening behavior is different from the one reported by Caceres and Blake for cast pure Mg, as shown in Figure 4.

The KM plots for specimens with lowest elongation are presented in Figure 20. The work hardening behavior is consistent between high and low quality specimens.

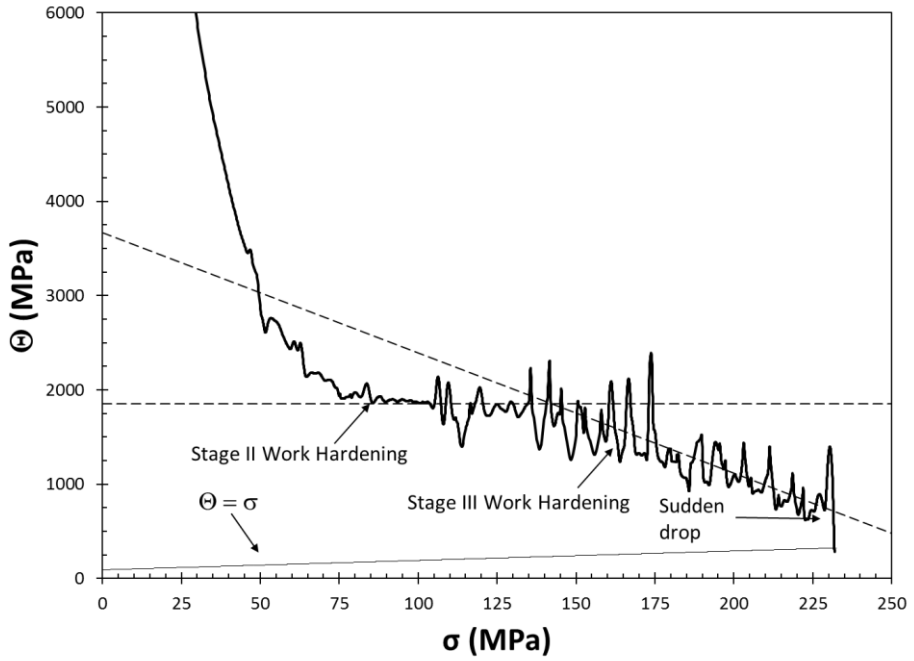

(a)

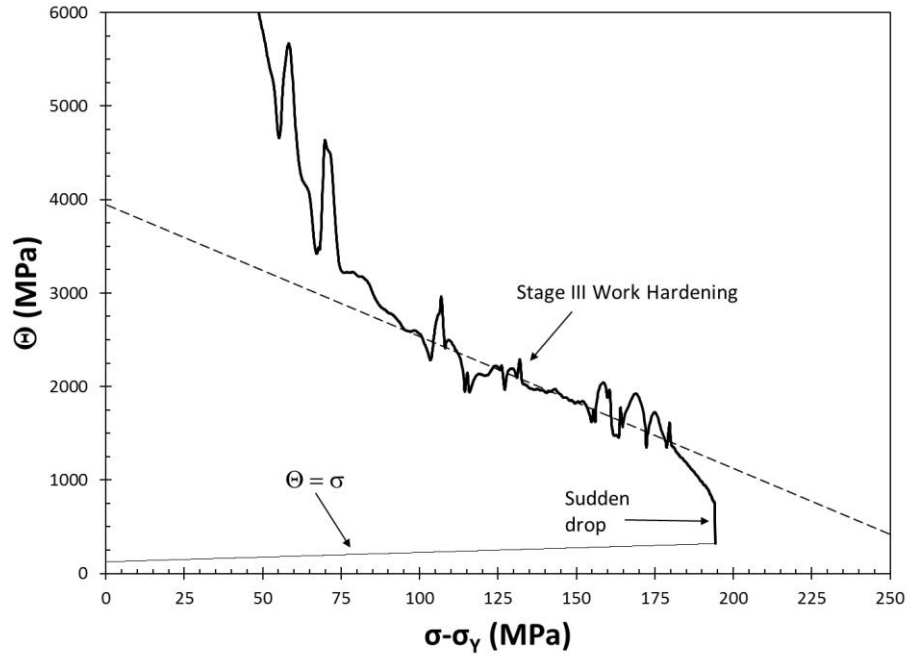

(b)

Figure 19: KM plots for specimens with highest elongation in (a) T4 and (b) T6 [84].

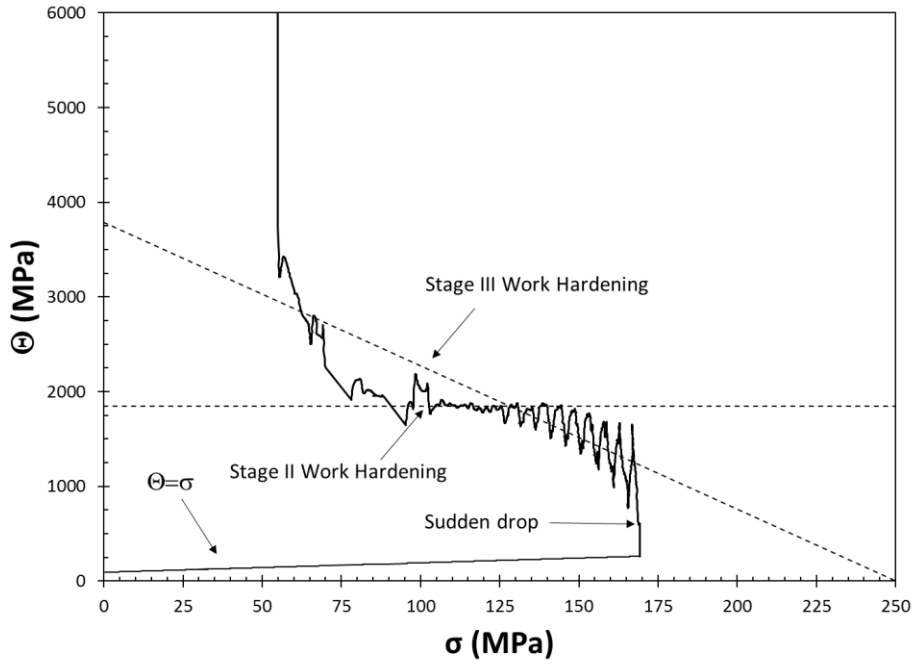

(a)

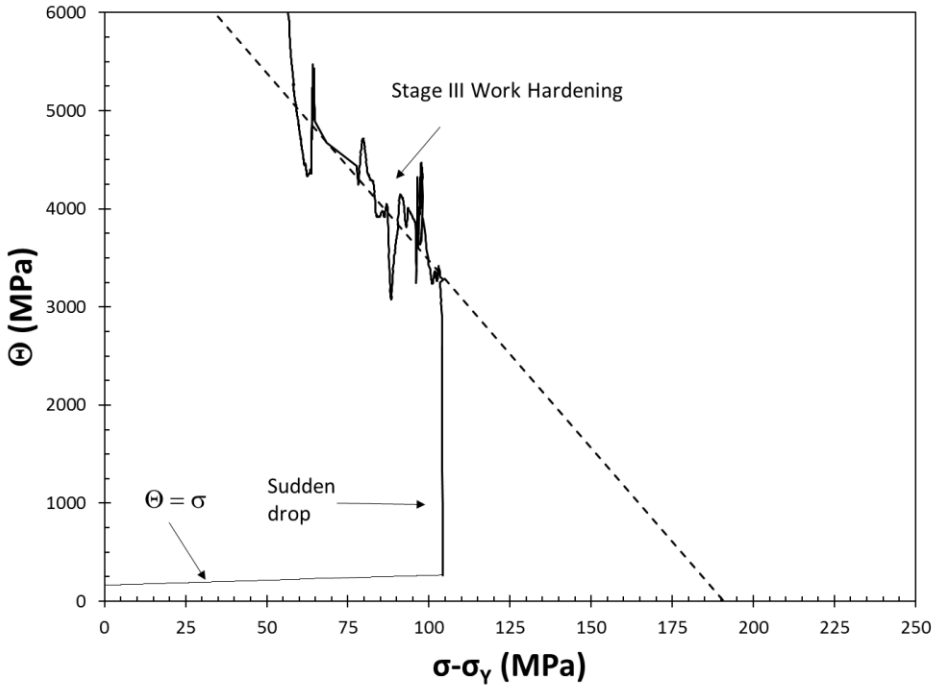

(b)

Figure 20: KM plots for specimens with lowest elongation in (a) T4 and (b) T6.

In all specimens, a sudden drop in work hardening rate prior to final fracture is observed. It was determined [14,15] in cast aluminum alloys via fractographic analysis that this sudden drop was a result of the presence of structural defects, such as bifilms and pores in castings. These defects result in premature fracture in tension. Note that the sudden drop in work hardening rate for both specimens has taken place at a level well above the level of true stress, as indicated by the "$\Theta = \sigma$" line. Therefore, the Consideré criterion is met only at the microscale, in areas around casting defects that acted as stress concentrators.

To determine the effect of work hardening behavior on ductility, possible relationships between work hardening parameters, K and Θ, and elongation need to be investigated. For T4, Θ_{III} values are clearly lower than T6 specimens. Figure 21 shows the dot plot of Θ_{III} for both heat treatment conditions.

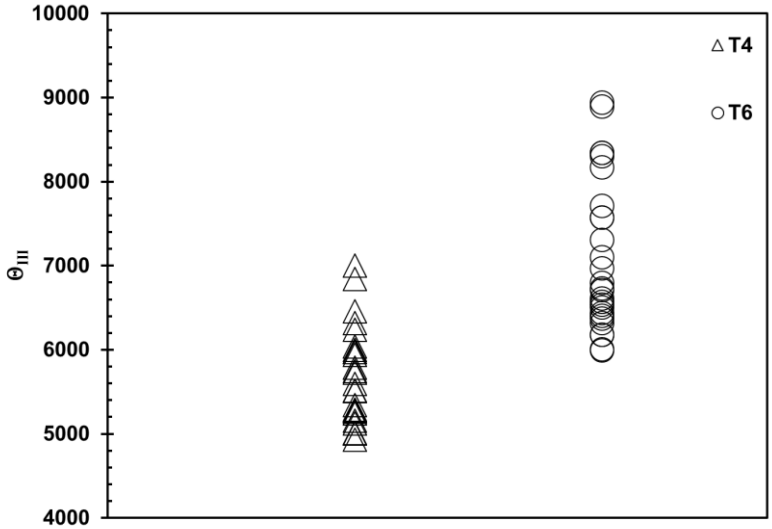

(a)

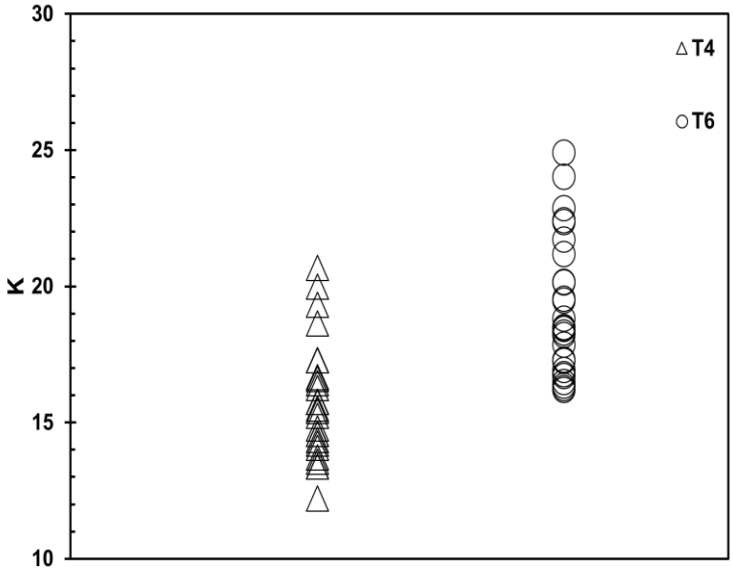

(b)

Figure 21: Dot plot analysis of T4 and T6 samples for Stage III work hardening rate, (a) Θ_{III} and (b) K.

Table 12 shows that decreased K value indicates higher elongation and higher quality index. Figure 24-a shows the relationship between elongation and K, alternatively Figure 24-b shows the relationship between quality index and K. In Figure 24, for both heat treatment conditions, it can be stated that higher elongation indicates lower K values. Lines of the decrease for both T4 and T6 specimens have very close slopes. This indicates that the relationship between K and elongation and alternatively the relationship between K and quality index is independent from the aging. Note that Stage II starts at the same work hardening rate for all specimens whether they have high elongation or low.

That is why contribution of Stage II region to the elongation and quality index needs to be compared with T6 specimens. Calculation of the $\Delta\sigma_{II}$ and contribution of Stage II work hardening are presented in Figure 22 and Figure 23 respectively. From the equations of the lines, intercept values were calculated and σ of Stage II start was subtracted from σ of Stage II end. Results are presented in Table 12. Relationships between K vs. elongation and K vs. quality index are re-analyzed for this purpose.

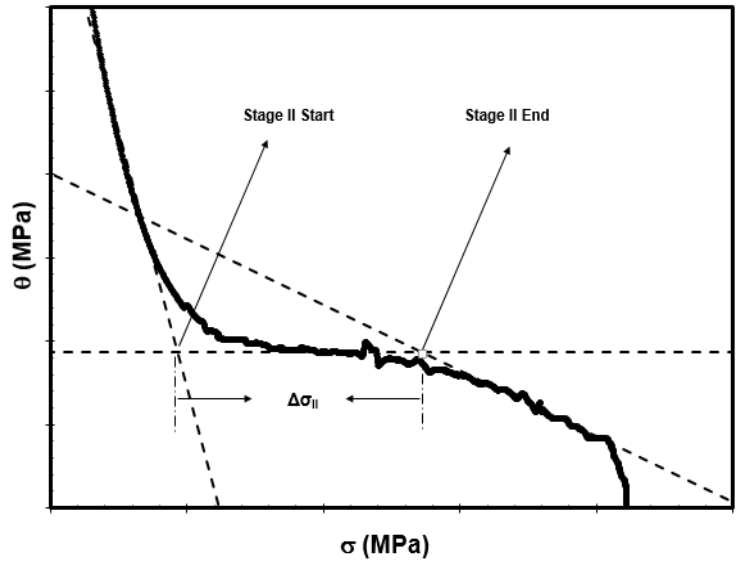

Figure 22: Calculation of Stage II work hardening.

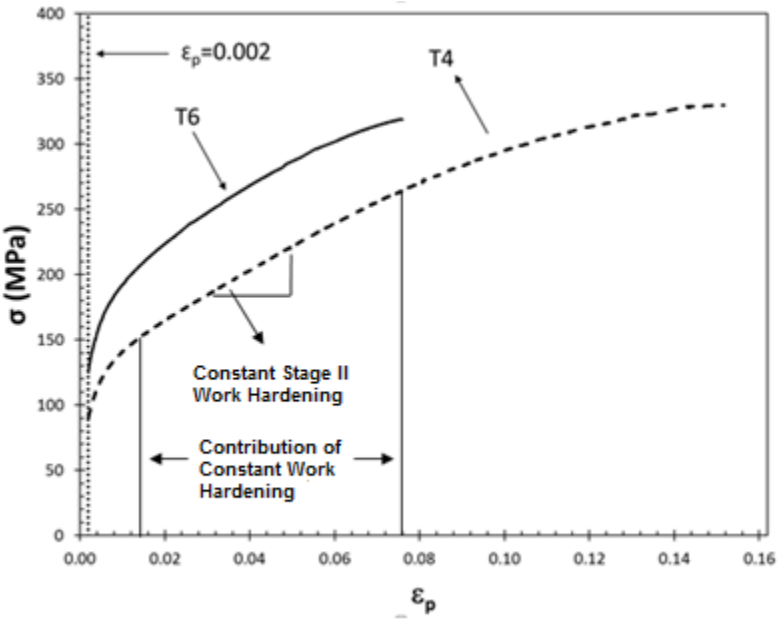

Figure 23: Contribution of Stage II work hardening.

Table 12: Result of the Kocks-Mecking analysis of all specimens in T4 and T6.

T4					T6		
No.	K	θ_{III} (MPa)	θ_{II} (MPa)	$\Delta\sigma_{II}$ (MPa)	No.	K	θ_{III} (MPa)
1	14.58	5274.5	1912	101.92	1	20.17	7310.0
2	13.56	5013.5	1879	97.78	2	19.49	6969.4
3	16.61	5996.6	1889	104.69	3	16.35	6180.9
4	20.68	6840.6	1901	99.76	4	16.27	6176.2
5	13.73	5123.7	1850	101.86	5	21.19	7571.1
6	18.64	6318.6	1890	107.78	6	22.37	8342.3
7	14.78	5286.7	1869	103.54	7	16.94	6316.1
8	14.24	5154.2	1850	96.40	8	16.72	6403.1
9	15.42	5725.4	1899	111.02	9	18.31	7098.4
10	15.25	5515.2	1862	109.01	10	22.88	8172.8
11	14.37	5262.3	1875	103.18	11	17.26	6435.4
12	13.39	5003.3	1881	96.72	12	18.45	6506.9
13	14.58	5274.5	1872	104.81	13	24.92	8894.9
14	15.76	5345.7	1922	101.41	14	18.50	6710.0
15	17.29	6237.2	1881	106.40	15	17.87	6572.1
16	12.20	4932.2	1878	107.04	16	21.72	8303.1
17	15.53	5511.5	1869	99.78	17	22.42	8345.1
18	15.76	5595.7	1875	101.66	18	16.78	6006.7
19	13.39	5003.3	1868	98.55	19	16.50	5990.0
20	16.68	5970.6	1882	108.15	20	18.81	6728.8
21	20.00	7000.0	1894	109.04	21	18.47	6608.4
22	16.27	5976.2	1878	101.23	22	17.30	6538.1
23	14.07	5244.0	1883	99.96	23	16.21	6372.7
24	15.76	5745.7	1888	104.88	24	20.16	7709.3
25	17.29	6037.2	1874	105.08	25	19.54	7572.3
26	16.44	5786.4	1868	101.28	26	24.03	8941.9
27	17.29	5937.2	1880	99.49	27	18.23	6793.5
28	19.32	6459.3	1860	96.23	-	-	-

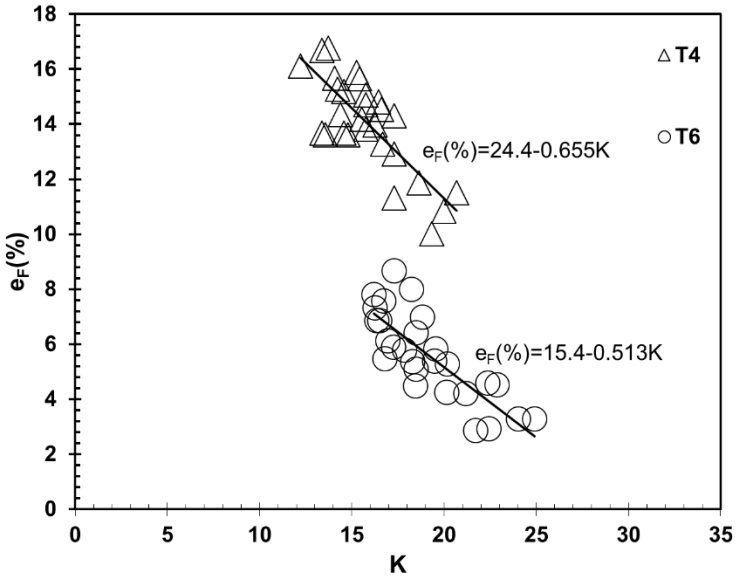

(a)

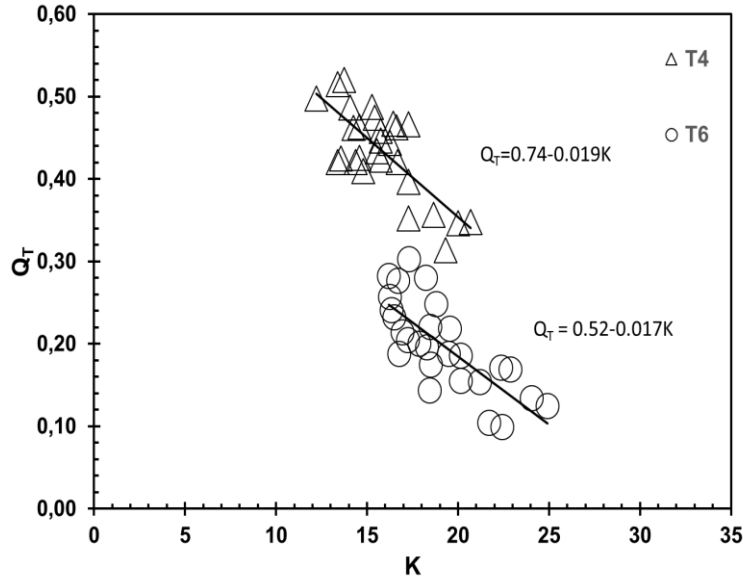

(b)

Figure 24: Relationship between K and (a) elongation, (b) quality index.

Figure 25 shows the absence of Stage II contribution for both (a) elongation and (b) quality index. In this figure, it can be observed that, in the absence of a plateau in Stage II, elongation (a) and quality index (b) of T4 specimens are approximately in the same region with T6 specimens. Hence the only difference in work hardening behavior between T4 and T6 specimens is the absence of the plateau in T6. The reason for this is unknown at this time.

Because the plateau in work hardening rate appears in T4 specimens but not in T6, the Q_T concept, originally developed for aluminum alloys which follow the same work hardening behavior and exhibits no such plateau, is not directly applicable to cast Mg alloys, at least in its original form.

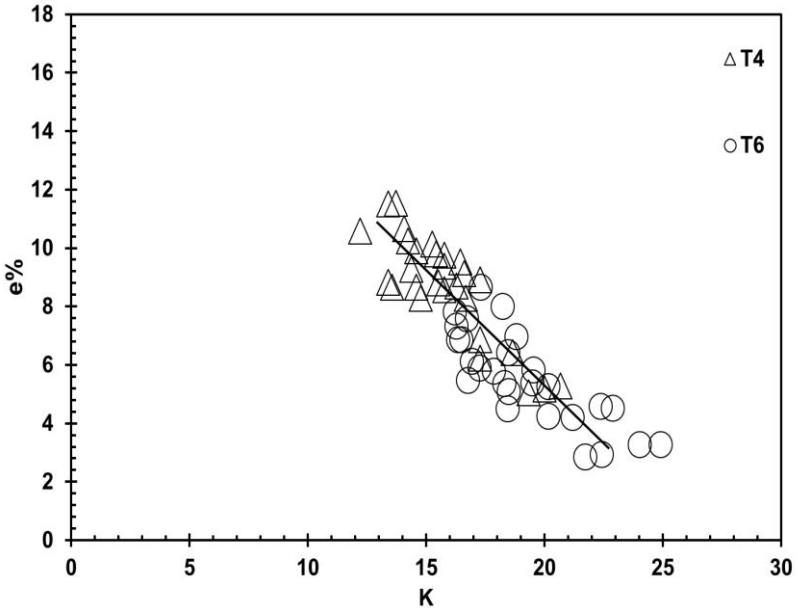

(a)

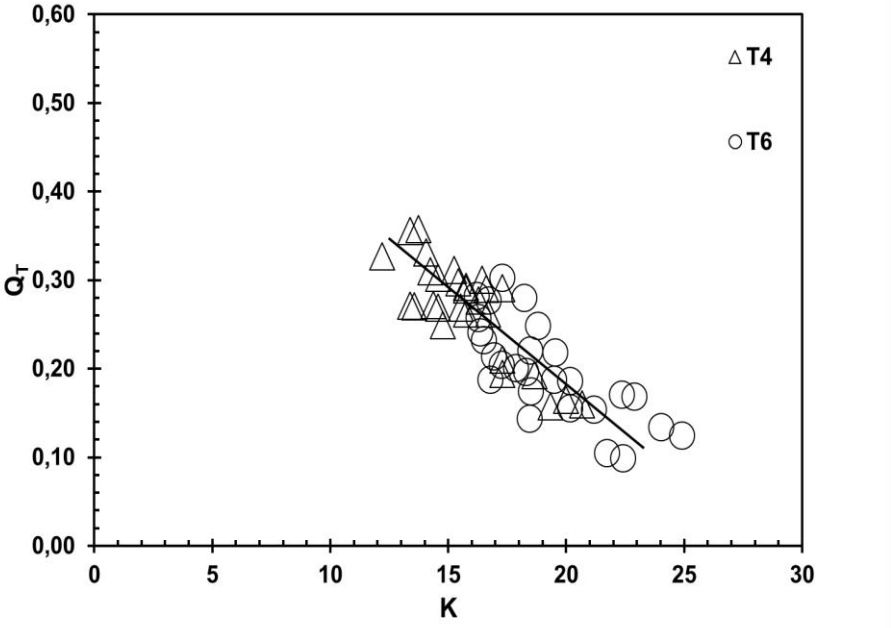

(b)

Figure 25: Relationship between (a) elongation and K and (b) quality index and K with constant.

Figure 26 shows that yield strength has no effect on Stage II work hardening. Moreover, this might mean that Stage II work hardening is the region that makes the difference between both heat treatment conditions.

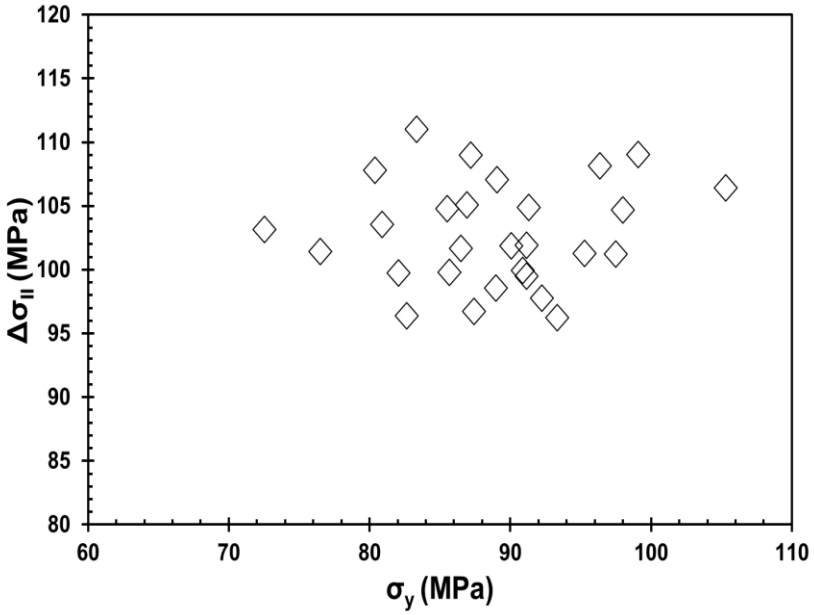

Figure 26: Relationship between Stage II work hardening in T4 specimens and yield strength.

The steep decrease in Θ, indicative of short elastoplastic transition, is in contradiction with the results reported [85] for an extruded AZ31B alloy, for which internal strains developed in tension and compression were measured by *in situ* neutron diffraction. The results showed that the elastoplastic transition is extended, sometimes lasting as long as 10% strain. Moreover, work hardening is a result of "a composite – like load sharing between soft – and hard – oriented grains" [85]. Note that the decrease in Θ for the T6 specimen is not as steep and there is not Stage II with a constant work hardening rate (Figure 19-b). Hence the elastoplastic transition is longer for the T6 specimen. Kocks-Mecking analysis conducted by del Valle et al. [82] on ECAP AM60

showed that some specimens displayed the short elastoplastic transition followed by a Stage II, similar to the T4 specimen (Figure 19-a), whereas others had an extended elastoplastic transition and no Stage II with a constant Θ, similar to the T6 specimen, (Figure 19-b). The reason for this difference in ECAP AM60 was attributed to texture effects.

5.3. Fractographs

To have a better understanding of possible effects of bifilms and pores on deformation, specimens with highest and lowest elongations were selected for SEM analysis. Oxide bifilms and pores are observed on the all fracture surfaces of tensile test specimens.

Pores can be seen from Figure 27 for T6 specimen. These pores are evidence of entrained bifilms. As a result of shrinkage induced shear forces, entrained oxides films were torn apart and lead specimen to fracture. Note that this fractograph was obtained for the specimen that has the highest elongation (a) (8%) and one of the lowest elongation (b) (3.2%) among other T6 specimens.

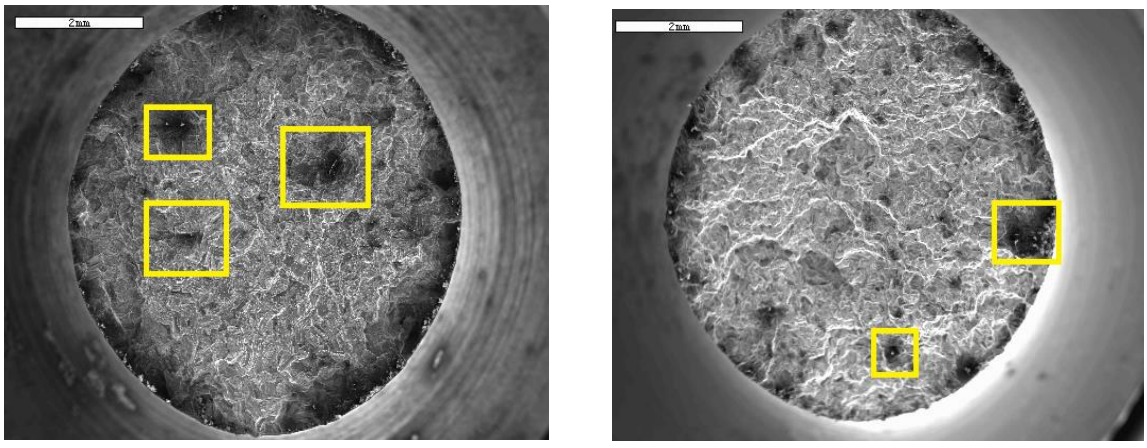

(a) **(b)**

Figure 27: Overall fractograph of T6 specimens with (a) 3.2% elongation and 0.12 quality index and (b) 8 % elongation and 0.28 quality index.

For the same specimen, ductile fracture morphology was observed in particular spots. Moreover, in some of these spots, a faceted fracture was also detected. Such example of the fracture surfaces of AZ91D samples with T6 heat treatment are shown in Figure 28. Dimples can be seen in Figure 28-b, indicative of ductile fracture.

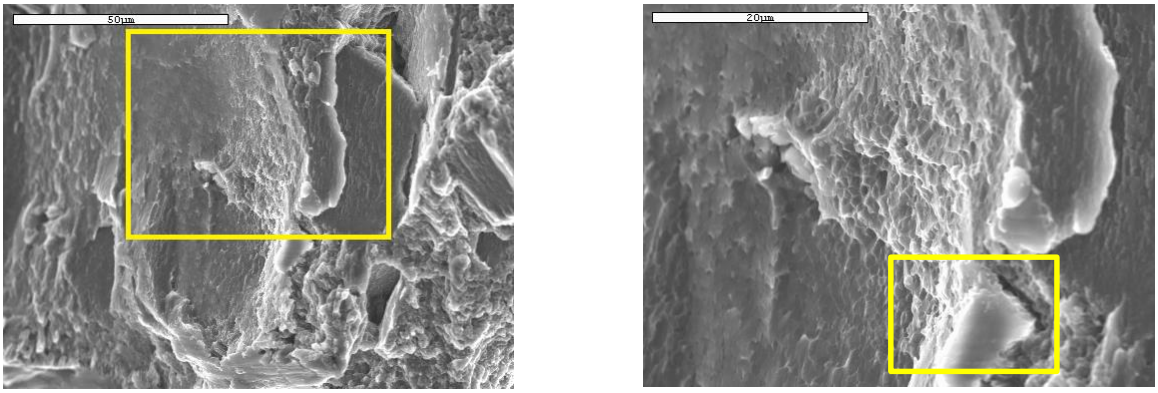

(a) **(b)**

Figure 28: Faceted fracture types in T6 specimen with 8 % elongation and 0.28 quality index.

Brittle fracture was observed for T6 specimens. This brittle fracture can also be seen in Figure 29 and Figure 31. It can be seen in these figures that these specimens show tortuous fracture surfaces which indicates the brittle fracture.

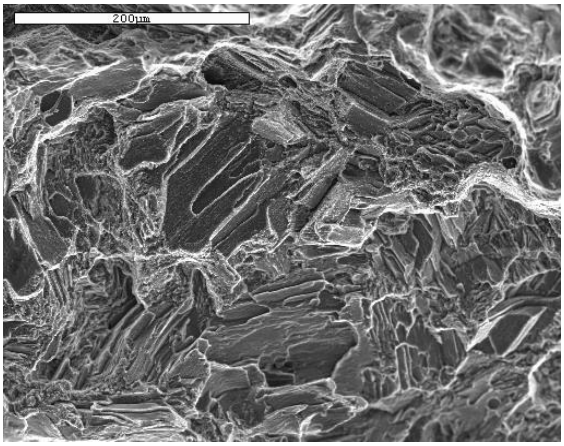

Figure 29: Fracture surface of T6 AZ91 sample with 8% elongation and 0.28 quality index.

Fracture surfaces of T6 specimen with 3.28 % elongation and 0.12 quality index are presented in Figure 30. Pores which are caused by oxide bifilms are indicated. Brittle fracture surface is observed for this specimen in Figure 31. Moreover, it must be noted that very interesting fractographs were observed on the fracture surfaces. Such an interesting feature is presented in Figure 32.

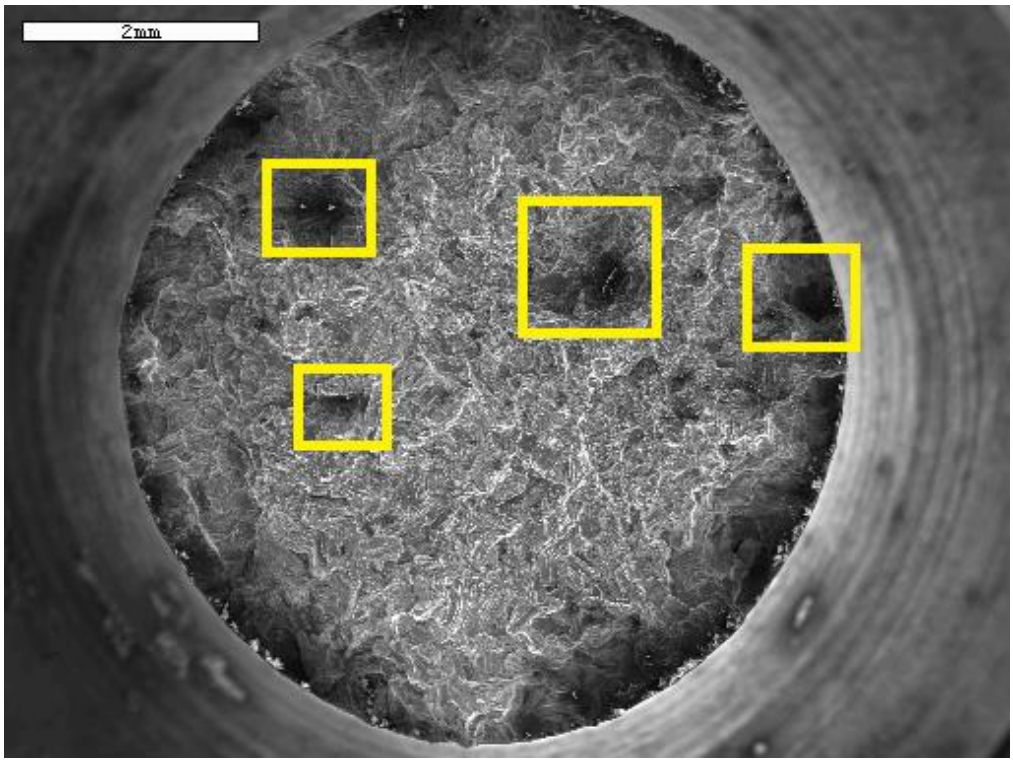

Figure 30: Pores on the fracture surface of AZ91 T6 samples with 3.28% elongation and 0.12 quality index.

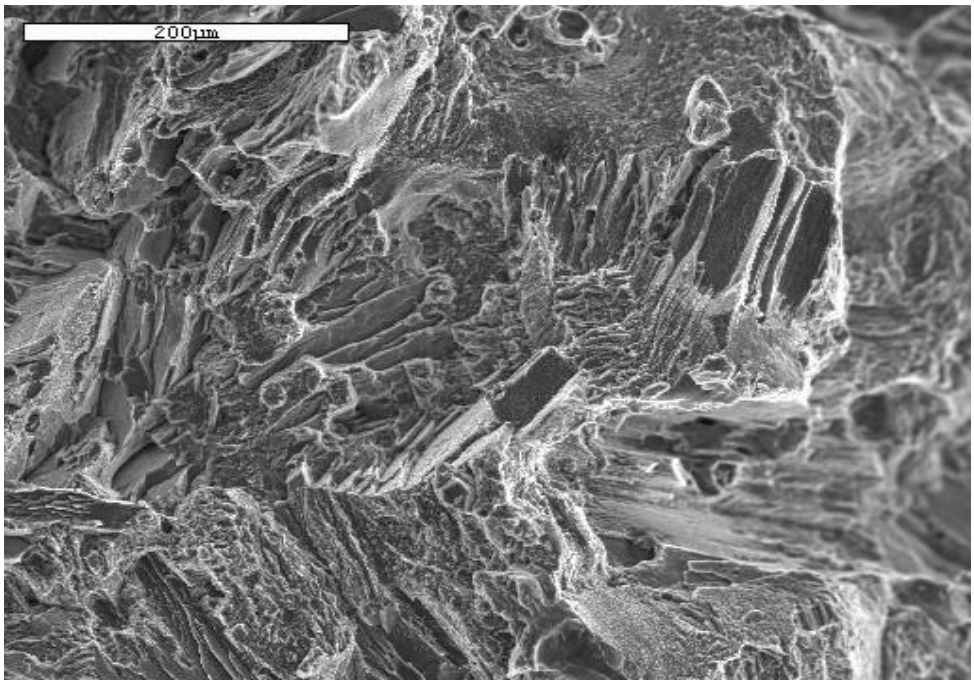

Figure 31: Fracture surface of AZ91 T6 samples with 3.28 % elongation and 0.12 quality index.

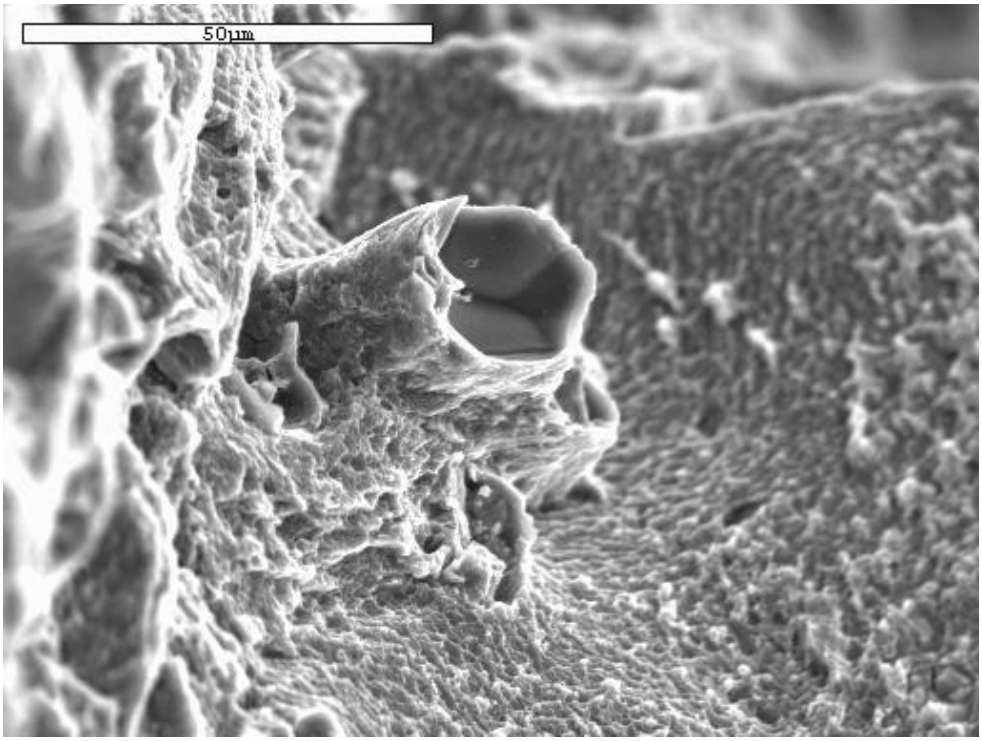

Figure 32: An interesting fracture surface was observed for AZ91D samples.

Fracture surfaces of tensile test specimens with T4 heat treatment were also taken (Figure 33) from AZ91 samples with 16.77% and 0.52 quality index. Consistently with previous figures, it can be stated that the fractures were occurred where entrained bifilms were present. Fractographs for fracture surfaces are obtained. Note that more pores have been detected (Figure 34 (a) and Figure 34 (b)) on the fracture surface of T4 specimen with lower elongation. Moreover, in particular spots, Mg-Si precipitates are detected and EDS analysis is conducted. Also for this specimen, high degree of localized ductility has been observed and it is presented in Figure 35.

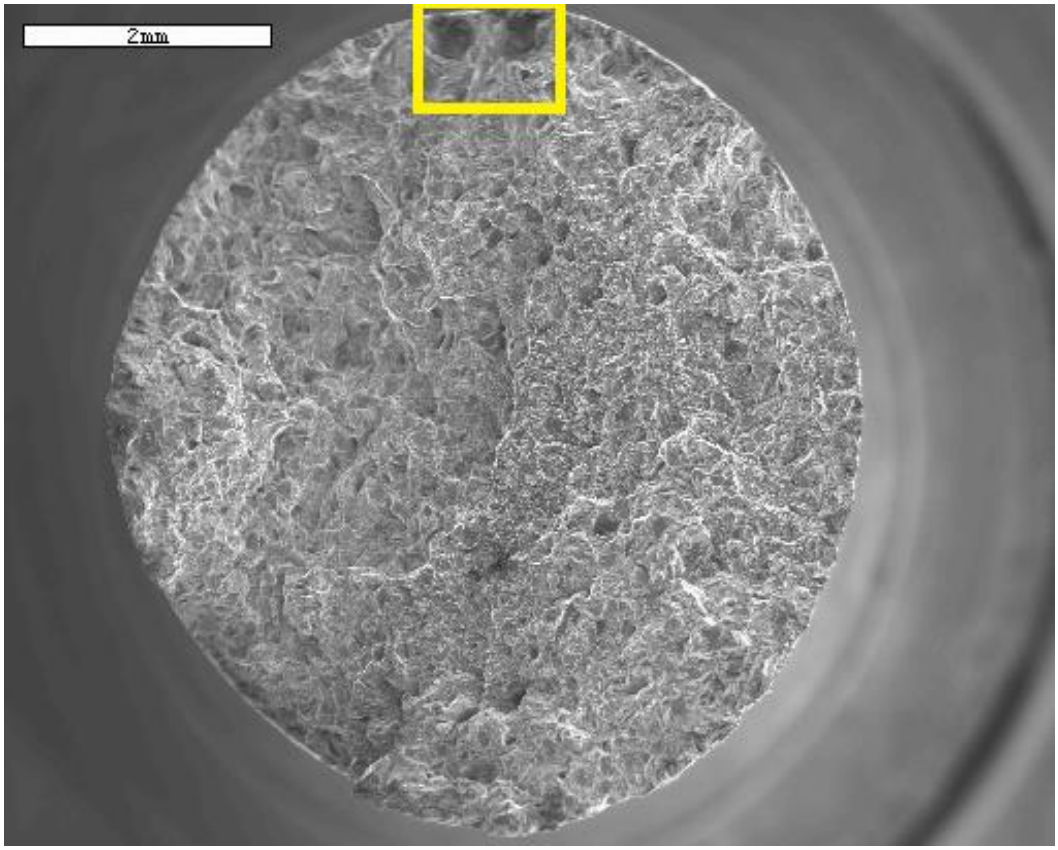

Figure 33: Overall fractograph of T4 specimen with 16.77 % elongation and 0.52 quality index.

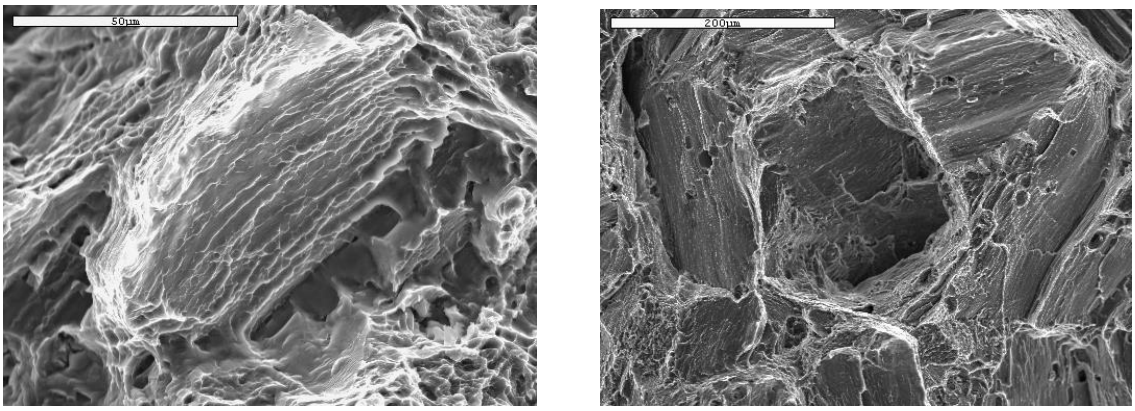

(a) **(b)**

Figure 34: Fracture surfaces for T4 specimen from AZ91 samples with 16.77 % elongation and 0.52 quality index.

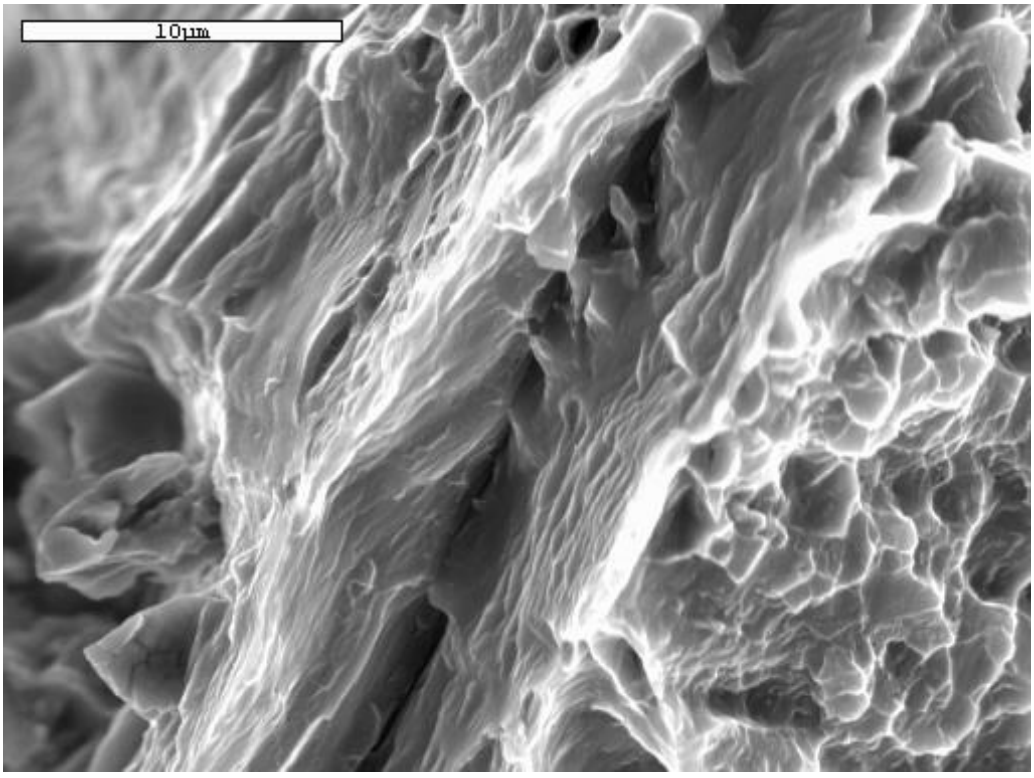

Figure 35: Tearing most likely caused by opened up oxide bifilms for AZ91 samples with 16.77% elongation and 0.52 quality index.

Fracture surfaces of tensile test specimens with T4 heat treatment were also taken (Figure 36) from AZ91 samples with 11.32 % and 0.35 quality index. Comparing with the other T4 sample that has higher elongation, more pores have been detected in this specimen. Like the other AZ91 samples, faceted fracture surfaces have been observed. For this specimen, oxide bifilm in a hole on the fracture surface has been detected. Brittle fracture surface is also observed for this sample and it is shown in Figure 37. In this specimen, also ductile fracture is observed in Figure 38.

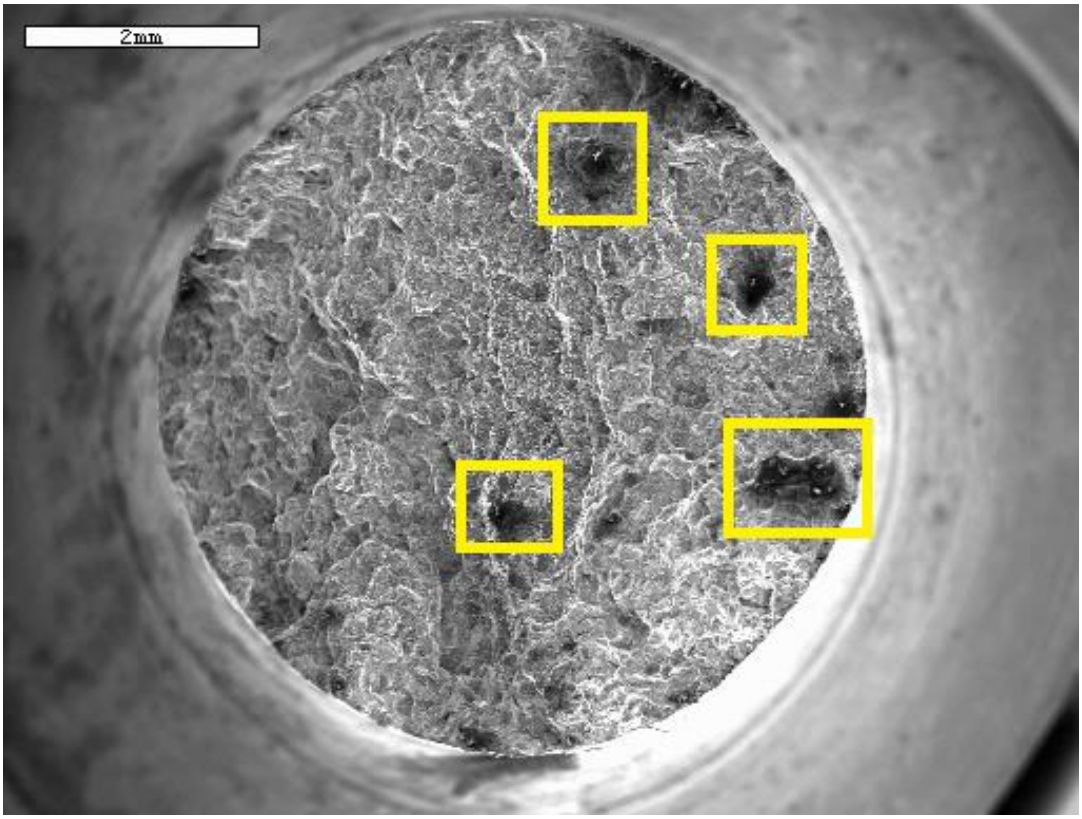

Figure 36: Fracture surface the AZ91-T4 specimen with 11.32 % and 0.35 quality index.

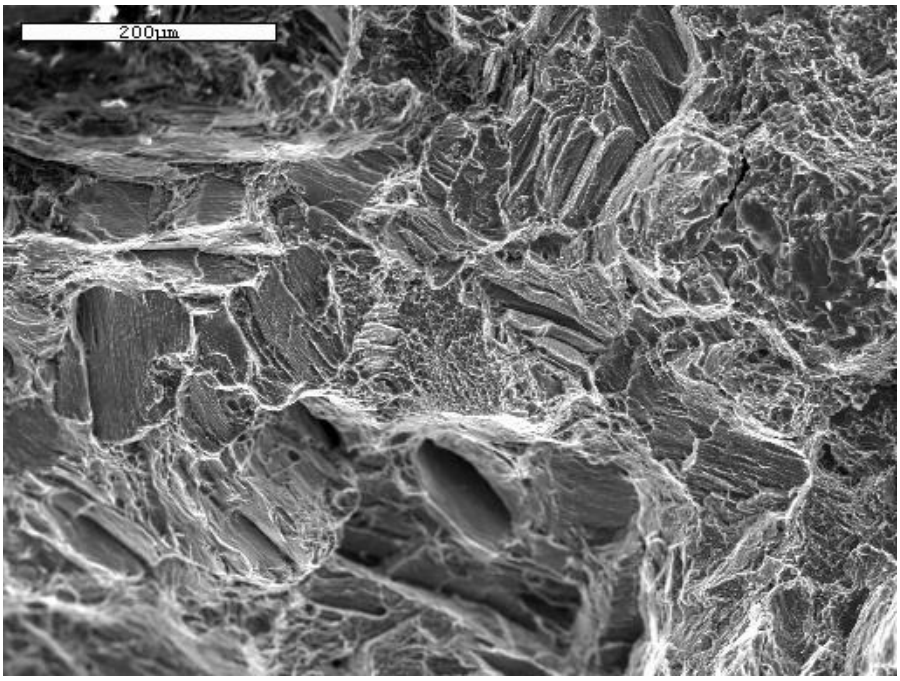

Figure 37: Fracture surface of the AZ91-T4 specimen with 11.32 % and 0.35 quality index.

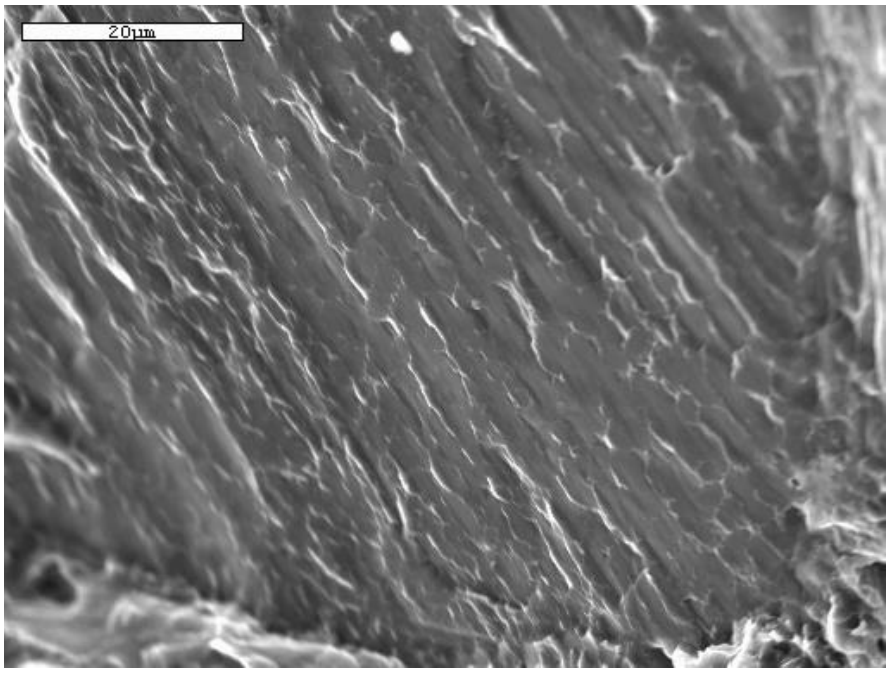

Figure 38: Ductile fracture surface of AZ91-T4 specimen with 11.32% elongation and 0.35 quality index.

CHAPTER 6: CONCLUSIONS

In this study, the following conclusions were reached:

1. After analyzing more than 1600 data points from the literature for various Mg alloy families, . the ductility potential (e_{Fmax}) for cast Mg alloys was developed as;

$$e_{F(max)}\,\% = 41.8 - 0.106\sigma_Y$$

   This ductility potential equation can be used as a metric to compare elongation obtained from tensile specimens to measure the structural quality of Mg alloy castings.

2. Results indicated that ductility potential was not affected by heat treatment condition, grain size (within 30-120 μm), casting geometry, size, the type of casting process nor chemical composition.

3. Four constitutive equations, the Hollomon, Voce, Ludwik and Swift, were fitted to true stress-true plastic strain data in the elastoplastic region of T4 and T6 specimens. Results indicated R^2 values for all equations were in excess of 0.99, suggesting that all four equations provide excellent fits to tensile data in both heat treatment conditions.

4. The change in work hardening rate with true stress was investigated for all specimens by using Kocks-Mecking (KM) plots. It was determined that work hardening behavior in T4 specimens exhibits a plateau in work hardening rate at approximately E/25. The presence of this plateau is consistent with results given in the literature for pure Mg.

5. None of the T6 specimens exhibited a plateau with constant work hardening rate. The reasons for the absence of the plateau in T6 specimens are unknown at this time.
6. In both T4 and T6 specimens, the KM work hardening model in which the work hardening rate changes linearly with true stress was found to be applicable. This is the first time that KM model was found to be valid for Mg alloys.
7. Elongation of cast AZ91 was found to decrease linearly with the KM parameter, K. However the relationship between elongation and K was different for each temper.
8. In all specimens investigated in this study, there was a sudden drop in work hardening rate just prior to final fracture. This drop was attributed to structural defects in specimens via fractography.
9. Because of the difference of the work hardening behavior between T4 and T6 specimens due to the plateau in T4, the quality index method, which is supposed to be independent of heat treatment, did show that T4 and T6 specimens had different quality index levels. Consequently, it was concluded that the quality index method was not applicable to Mg alloys, at least in its original form.

CHAPTER 7: FUTURE WORK

Although the present study shed some light on the tensile deformation characteristics of cast Mg alloys, it has also raised some questions, which are as follows:

1. Does chemical composition have truly no effect on the ductility potential? In aluminum alloys, different alloy families had different lines, although they are close to each other.
2. Does the plateau in work hardening rate change with artificial aging time? To determine the answer to this question, experiments can be designed to test the effect of aging time, ranging between as quenched and well-overaged. It is hypothesized that the width of the plateau, $\Delta\sigma_{II}$, is a function of the artificial aging time.
3. When casting quality is higher, i.e., closer to ductility potential and without major defects on fracture surfaces, will T6 specimens exhibit a plateau in KM plots?

It is recommended that research be conducted to determine the answer to these questions.

REFERENCES

1. D.J. Bray: in AGARD Lecture Series No. 174, 7-1, (1990).
2. P. Krajewski, A. Sachdev, A. Luo, J. Scroth, Ligt Metals Age, 67, 5, (2009), 6-13.
3. Anon. "High Integrity Magnesium Alloy Components", USAMP Project AMD 601, Final Report, (2010).
4. J. Campbell, Castings, 2nd Edition, Butterworth-Heinemann Ltd, Oxford, (2003).
5. J. T. Staley Jr., M. Tiryakioglu, J. Campbell, Mater Sci. Eng., A, 465, (2007), 136-145.
6. B. L. Mordike, T. Elbert, Mater. Sci. Eng. A, 302, (2001), 37-45.
7. C. D. Lee, K. S. Shin, Acta Mater., 55, (2007), 4293-4303.
8. C. D. Lee, Mater. Sci. Eng. A, 459, (2007), 355-360.
9. M. Tiryakioğlu. Mater.Sci Eng. A, 527, (2010), 4546–4549.
10. N. R. Green, J. Campbell, Mater. Sci. Eng. A, 173, (1993), 261-266.
11. C. Nyahumwa, N. R. Green, J. Campbell, Metall. Mater. Trans., A, 32, (2001), 349-358.
12. J. Campbell, Mater. Sci. Technol. 22, 2, (2006), 127-145.
13. O. Űnal, M. Tiryakioğlu: Mater. Sci. Eng., A, 643, (2015), 51-54.
14. M. Tiryakioğlu, J. Campbell, J.T. Staley: Scripta Mater., 49 (2003) 873–878.
15. M. Tiryakioğlu, J. Campbell, J.T. Staley: Mater. Sci. Eng., A, 368 (2004) 205-211.

16. M. Tiryakioğlu, J.T. Staley, Jr., J. Campbell: Mater. Sci. Eng., A., 487, (2008), 383-387.

17. C. H. Caceres, A.H. Blake, Mater. Sci. Eng., A, 462, (2007), 193-196.

18. H.-Y. Wu, J.-C. Yan, H.-H. Tsai, C.-H. Chiu, G.-Z. Zhou, C.-F. Lin: Mater. Sci. Eng., A, 527, (2010), 7197-7203.

19. N. Afrin, D.L. Chen, X. Cao, M. Jahazi: Scripta Mater., 57, (2007), 1004–1007.

20. M. Jonsson, Athmospheric Corrosion of Magnesium Alloys, Stockholm, Sweden, (2007).

21. M. O. Pekguleryuz, K. Kainer, A. Kaya, "Fundamentals of Magnesium Alloy Metallurgy" Woodhead Publishing, 1st Edition, (2013).

22. J.I. Skar, D. Albright, Magnesium Tech. 2002 (2002) 255-261.

23. M. M. Avedesian, H. Baker, "Magnesium and Magnesium Alloys", ASM International. Handbook Committee, (1999).

24. N. Woldman, "Magnesium Casting." Magnesium, ASM International, (1946).

25. A. Beck, "Magnesium und seine Legierungen", Springer Verlag, Berling, (1939).

26. C. Blawert, N. Hort and K. U. Kainer, Trans. Indian Inst. Met. 57, 4, (2004), 397-408.

27. R. Sachnell, R. Hones, F. Kaumle, "Verband fur Materialforschung und Korrosion an Fahrzeugen", DVM-Tag, (1995), 175-190.

28. A. Kumar, R.R. Adharapurapu, J.W. Jones, T.M. Pollock, Scr. Mater., 64, (2011), 65-68.

29. C.L. Fan, D.L. Chen, A.A. Luo, Mater. Sci. Eng., A, 519, (2009), 38-45.

30. H.A. Patel, D.L. Chen, S.D. Bhole, K. Sadayappan, J. Alloys Compd., 496, (2010), 140-148.

31. T. B. Abbot, M. A. Easton, C. H. Caceres, Marcel Dekker, (2004), 487-538.

32. J. C. Benedyk, Light Metal Age, Reprinted, International Temper Designation Systems for Wrought Aluminum Alloys, (2010), 16-22.

33. H. Westengen, Journal Physique IV, (1993), 491–501.

34. S. Fleming, "An Overview of Magnesium based Alloys for Aerospace and Automotive Applications", Rensselaer Polytechnic Institute, Hartford, CT, August, (2012).

35. E. F. Emley, "Principles of Magnesium Technology, Pergamon Press, Oxford, (1996).

36. A. R. Mirak, M. Divandari, S. M. A. Boutorabi and J. Campbell, International Journal of Cast Metals Research, 20 (2007) 215-220.

37. F.A. Mirza, D.L. Chen, D.J. Li, X.Q. Zeng, Mater. Sci. Eng., A, 575, (2013), 65–73.

38. A. Macwan, X.Q. Jiang, C. Li, D.L. Chen, Mater. Sci. Eng., A, 587, (2013), 344–351.

39. Q.G. Wang, C.H. Cáceres, Mater. Sci. Eng. A, 241 (1998) 72-82.

40. E.W. Miguelucci, AFS Trans., 93 (1985) 913-916.

41. J. Campbell, Metall. & Mater. Trans. A, 46, 11, (2015), 4848-4853.

42. D. Dispinar, J. Campbell, JOM, 182, (2007), 405-410.

43. X. Cao, J. Campbell, Metall. Mater. Trans. A, 34A, (2003), 1409-1420.

44. A. D. Rollett, U. F. Kocks, Materials Science Forum, (1993), 1-26.

45. A. Seeger, H. Kronmuller, S. Mader, H. Trauble, Philos Mag, 6, (1961), 639-644.

46. P.B. Hirsch, J.S. Lally. Philos Mag, 12, (1965), 595-602.

47. E. Schmid, W. Boas, "Kristallplastizitat" Berlin: Springer Verlag, (1935).

48. J. H. Hollomon. Trans. AIME., 162, (1945), 268-290.

49. E. Voce, Metallurgia, 51 (1955) 219-226.

50. P. Ludwik, in "Elements der technologischen Mechanik", p. 32,1909, Leipzig, Verlag Von Julius Springer

51. H.W. Swift, J. Mech. Phys. Solids, 1 (1952) 1-18.

52. U.F. Kocks: J. Eng. Mater. Tech., 98, (1976), 76.

53. H. Mecking, U.F. Kocks: Acta Metall., 29, (1981), 1865.

54. M. Tiryakioğlu, J. Campbell, N.D. Alexopoulos: Metall. Mater. Trans., B, 40, (2009), 802-811.

55. M. Tiryakioglu, J. Campbell, N.D. Alexopoulos: Metall. Mater. Trans., A, 40A, (2009), 1000-1007.

56. M. Tiryakioğlu, J.T. Staley, J. Campbell: Mater. Sci. Eng. A., 368, (2004) 231-238.

57. M. Tiryakioğlu, J. Campbell, N. Alexopoulos, Mater. Sci. Eng. A., 506, (2009) 23-26.

58. M. Tiryakioğlu, J. Campbell, Mater. Sci. Technol., 25, (2009) 784-789.

59. M. Tiryakioğlu, J. Campbell, Intl. J. Metalcasting, 8 (2014) 39-42.

60. M. Tiryakioğlu, J. Campbell: AFS Transactions, 13-1525, (2013), 217-222.

61. J. Song, S.-M. Xiong, M. Li, J. Allison: Mater. Sci. Eng., A, 520, (2009) 197-201.

62. J.P. Weiler, J.T. Wood: Mater. Sci. Eng., A, 527, (2009) 25-31.

63. J.P. Weiler, J.T. Wood: Mater. Sci. Eng., A, 527, (2009) 32-37.

64. S.G. Lee, G.R. Patel, A.M. Gokhale, A. Sreeranganathan, M.F. Horstemeyer: Scripta Mater., 53, (2005), 851-856.

65. C. D. Lee, K. S. Shin, Acta Mater., 55, (2007), 4293-4303.

66. C. D. Lee, Mater. Sci. Eng., A, 459, (2007), 355-360.

67. W. Weibull, "A statistical theory of the strength of materials". Proc. The Royal-Swedish Institute for Engineering Research. Nr. 151, (1939).

68. W. Weibull, "The phenomenon of rupture in solids", Royal Swedish Institute of Engineering Research (Ingenioersvetenskaps Akad. Handl.), Stockholm, 153, 1-55 (1939).

69. W. Weibull, J. Applied Mechanics, 13, (1951), 193-197.

70. F.T. Pierce, J. Textile Inst. 17, T355-T368, (1948).

71. M. Tiryakioglu, Metall. and Mater. Trans., A, 46A, (2015), 270-280.

72. B. Epstein, J. American Stat. Assoc., 43, (1948), 403-412.

73. M. Tiryakioglu, D. Hudak, Metal. Mater. Trans., B, 41, (2011), 1130-1135.

74. M. Tiryakioğlu, J. Campbell: Metall. Mater. Trans A., (2010), 41A, 3121-3129.

75. J. Campbell, "Casting", 2nd Edition, 303, London, Elsevier, (2003).

76. I.M. Mikhailovskij, T.I. Mazilova, V.N. Voyevodin, A.A. Mazilov: Physical Review B 83, 134115 (2011).

77. H. Hu, M. Zhou, Z. Sun, N. Li: J. Mater. Process. Technol. 201 (2008) 364-368.

78. B. Lagowski, J. Meier, "*Properties of Sand-Cast Mg Alloys, Part VIII: Foundry Characteristics of Mg-Zn-Ag-Zr Casting Alloys",* Mines Branch Research Report, Department of Mines and Technical Surveys, R161, Ottawa, Canada, (1965).

79. "Heat Treater's Guide, Practices and Procedures for Nonferrous Alloys", ASM International, USA, November, (1996).

80. "ASTM E112-13, Standard Test Methods for Determining Average Grain Size", ASTM International, West Conshohocken, PA, (2013), www.astm.org

81. M. Tiryakioğlu, N.D. Alexopoulos, Metallurgical and Materials Transactions A., 39A, (2008) 2772-2780.

82. J.A. del Valle, F. Carreno, O.A. Ruano: Acta Mater., 54, (2006), 4247-4259.

83. M. Karami, R. Mahmudi: Mater. Sci. Eng., A, 607, (2014), 512-520.

84. O. Űnal, M. Tiryakioğlu, Shape Casting: 6th International Symposium, TMS, (2016), 117-124.

85. S.R. Agnew, C.N. Tomé, D.W. Brown, T.M. Holden, S.C. Vogel: Scripta Mater., 49, (2003), 1003-1008.

APPENDIX I

Materials Science & Engineering A 643 (2015) 51–54

Contents lists available at ScienceDirect

Materials Science & Engineering A

journal homepage: www.elsevier.com/locate/msea

Short communication

On the ductility potential and assessment of structural quality in Mg alloy castings

O. Űnal, M. Tiryakioğlu *

School of Engineering, University of North Florida, Jacksonville, FL 32224, USA

ARTICLE INFO

Article history:
Received 19 June 2015
Received in revised form
30 June 2015
Accepted 1 July 2015
Available online 8 July 2015

Keywords:
Quality index
Elongation
Ductility potential
Defects
Bifilms

ABSTRACT

Tensile data from literature are reanalyzed to determine ductility potential in magnesium alloys, which has yielded a linear relationship between maximum elongation and yield strength. Ductility potential line is significantly higher than those in the literature. Moreover, grain size, chemical composition, temper do not affect the yield strength-maximum elongation relationship.

1. Introduction

Mg alloy castings have been attractive candidates in load-bearing applications, where weight is critical [1]. The density of Mg alloys ranges from 1.5 g/cm^3 in magnesium–lithium to 1.8 g/cm^3 in magnesium-rare earth alloys [2]. Despite the significant weight savings that can be achieved over other light metals, Mg alloy castings have not been as common in aerospace and automotive applications as aluminum alloys. The barriers to their wider use have been recently addressed [3]: (i) porosity and hot-tearing during solidification, (ii) thermal treatments and (iii) process design to produce high-integrity cast magnesium components with high ductility and strength, low porosity that are free from oxide bifilms. For wider use of Mg alloy castings in structural applications, these barriers need to be removed through careful improvement of casting processes.

Recent research [4] has shown that initial melt quality, handling the molten metal and finally design of the filling system in the mold significantly affect the mechanical properties of castings, including fatigue life [5], elongation (e_F) [6–11] and tensile strength [12–13]. Therefore significant improvement in the quality of magnesium castings should focus on melt preparation and handling as well as filling system design. Such a quality improvement effort requires a metric that can be used to gage the effectiveness of techniques and/or processes implemented. However, there is no such metric available yet for Mg alloy castings. This study is motivated by this gap in the literature.

A metric for the assessment of structural quality of cast Al alloys has been developed [14–17] recently, based on the concept that, when large numbers of data are analyzed together, there is an increased likelihood to come across extreme data points which may reflect the true property potential of the metal. Using this property potential, a quality index that compares actual to potential tensile elongation has been introduced [14–17], along with specific guidelines on where to focus quality improvement efforts, depending on the current quality level. The same approach has been expanded in this study to cast Mg alloys for various compositions. Elongation and yield strength (σ_Y) data from 25 independent studies in the literature have been reexamined to determine the maximum elongation points for a given yield strength level.

2. Background

Mechanical properties in castings are mainly determined by the extent of the structural defects such as bifilms and pores. Bifilms are surface films that are entrained into the liquid metal either through poor handling of the liquid metal or during mold filling if the filling system has not been designed properly [7]. During solidification, bifilms open up under the negative pressure developed in the metal as well as by the diffusion of dissolved gases. They act as heterogeneous nucleation sites for intermetallics

* Corresponding author. Fax: +1 904 620 1391.
E-mail address: m.tiryakioglu@unf.edu (M. Tiryakioğlu).

http://dx.doi.org/10.1016/j.msea.2015.07.003
0921-5093/

and pores and/or serve as cracks that lead to hot tearing in the casting. Because of their overwhelming effect on the mechanical behavior, it has been suggested [18] that the microstructure plays almost no role when there are structural defects in castings.

Among all mechanical properties, low ductility is the most prominent symptom of the presence of major structural defects [14]. That is why efforts to increase ductility by changing heat treatment, a practice promoted in traditional metallurgy books as strength-ductility trade-off, has often been fruitless [14,17]. A more effective strategy to increase ductility is to improve the initial melt quality, eliminate liquid metal transfers and design the filling system carefully so that additional oxide bifilms are not entrained [14,19,20].

Strengthening in Mg alloys is achieved in precipitation hardening (e.g., Mg–Zn, Mg–Al and Mg–Ag systems), solute solution hardening and/or grain size hardening following the well-known Hall–Petch equation:

$$\sigma_y = \sigma_0 + kd^{-0.5} \tag{1}$$

where σ_0 is a material constant (MPa) and d is the grain size (μm). Alloying additions such as Zr and rare earth (RE) elements have been used widely for grain refinement [21] to achieve significant grain size strengthening. Decreasing grain size was also observed to increase ductility [22–23]. The low ductility of cast Mg alloys at room temperature has been attributed [2,24] to cracking along grain boundaries during tensile deformation as a result of only three slip systems being active (in the $<11\bar{2}0>$ directions) due to its hexagonal close packed (hcp) unit cell.

Tensile deformation in cast Mg alloys with defects has been investigated recently [11,25,26]. Song et al. conducted *in situ* experiments on die cast AM50 alloys and observed how the material around pores and bifilms deforms in tension. Only after stress exceeds yield strength, there was noticeable deformation around pores and bifilms. Song et al. also stated that (i) the final fracture is probably not due to cracking and/or decohesion of the β-phase ($Mg_{17}Al_{12}$) and (ii) the alloy could withstand large amount of plastic deformation before fracture although the presence of structural defects reduced the elongation to only 6%. For the same alloy, Lee et al. [27] found a strong correlation between elongation and area fraction of porosity on the fracture surface. The fracture path was observed to go through the regions of clusters of structural defects. Lee et al. stated that the defect-free elongation for the alloy with $\sigma_Y \approx 120$ MPa should be 29%. Weiler and Wood investigated the effect of pore area fraction on the elongation and tensile strength of AM60B alloy castings via experimentation [25] and finite element modeling [26]. As can be expected, they found that elongation is reduced significantly with increasing size of pores. They also attempted to estimate elongation when the area fraction of pores is zero, i.e., when the specimen is defect-free, by extrapolating the elongation – area pore fraction relationship to zero pores. For a specimen with $\sigma_Y \approx 130$ MPa, they estimated the defect-free elongation, $e_{F(max)}$, to be 10%. A similar approach was taken by Lee and Shin [8] and Lee [9] for AZ91 alloy castings. In these studies, elongation was correlated to the level of microporosity [8] and grain size [9]. Lee and Shin developed a critical strain model, which predicted $e_{F(max)}$ to be between 6 and 10% for $\sigma_Y = 125$ MPa, which agrees with the results of Weiler and Wood. Lee [9] extrapolated elongation-area pore fraction relationships for various grain sizes and found that for $\sigma_Y = 125$ MPa, defect-free elongation can be estimated as:

$$e_{F(max)} = 13.6 \exp(-1.3 \times 10^{-3} d) \tag{2}$$

Lee also suggested that the effect of grain size on elongation should become less pronounced with decreasing level of porosity.

The use of elongation as a measure of the structural quality of aluminum castings was proposed by one of the authors and his coworkers [19,28]. Comparison of current elongation to defect-free elongation, estimated from work hardening characteristics [29] was proposed as a quality index. However, structural defects affect the work hardening characteristics significantly in cast aluminum alloys [30,31]. Therefore, using work hardening characteristics of specimens with defects to estimate defect-free properties was found [19] to significantly underestimate $e_{F(max)}$. Subsequently, one of the authors and his coworkers used hundreds of data from the aerospace and premium castings literature for Al-7% Si–Mg [32], A206 [33] and A201 [34] to estimate $e_{F(max)}$. Because yield strength is minimally affected by structural defects, yield strength is plotted in the x-axis with e_F on the y-axis. A linear relationship between yield strength and elongation was found [14] for all alloys:

$$e_{F(max)} = \beta_0 - \beta_1 \sigma_Y \tag{3}$$

where β_0 and β_1 (MPa^{-1}) are alloy-dependent coefficients although the linear relationships for the three alloys are very similar. Therefore, the quality index, Q_T, can then be found by;

$$Q_T = \frac{e_F}{e_{F(max)}} = \frac{e_F}{\beta_0 - \beta_1 \sigma_Y} \tag{4}$$

Tiryakioğlu and Campbell [14] have recently suggested that there are three regions for Q_T: (1) Q_T is below 0.25, (2) Q_T is between 0.25 and 0.70, and (3) Q_T is above 0.70. In Region 1, premature fracture is due to "old", coarse oxide bifilms which are typically the skins of ingots. In this region, engineers need to focus on melt quality to eliminate old oxides from remelts. Chilling the melt can increase the quality marginally. In Region 2, the molten metal which is free from major "old" oxides but there are "young" oxide bifilms which are entrained during molten metal transfers and mold filling. Chilling can freeze bifilms in the beginning of the process which can increase the properties of the metal. When Q_T is above 0.70, every small detail of the melt preparation and mold filling system design needs to be reviewed. In this region, chilling, i.e., decreasing secondary dendrite arm spacing (SDAS) has no effect on elongation [17]. For all three regions, Tiryakioğlu and Campbell proposed specific quality improvement efforts.

The approach taken by Tiryakioğlu and coworkers has been applied to Mg alloy castings in this study by collecting large numbers of tensile data from the literature and analyzing elongation versus yield strength.

3. Analysis of data and discussion

In this study, elongation and yield strength data from twenty five independent studies in the literature [35–59] have been reanalyzed. In total, more than one thousand and six hundred data points have been collected and analyzed. Alloys from fifteen commercial alloy families as well as a binary alloy have been included. As indicated above, elongation (y-axis) data have been plotted versus yield strength (x-axis). The plot for all data is presented in Fig. 1. Note that there are many specimens at low ductility levels ($\leq 5\%$), especially when yield strength exceeds 100 MPa. Therefore, it is easy to understand why low ductility is assumed to be intrinsic in Mg castings. Fig. 1 also shows that for a particular level of yield strength, number of data points becomes sparse with increasing elongation. The number of points that can be considered maximum at any given yield strength level is approximately 25. Therefore, less than 2% of all data included in this study represent maximum elongation values.

In Fig. 1, maximum points seem to have linear trend with yield strength, similar to what was reported for Al alloys. The line that

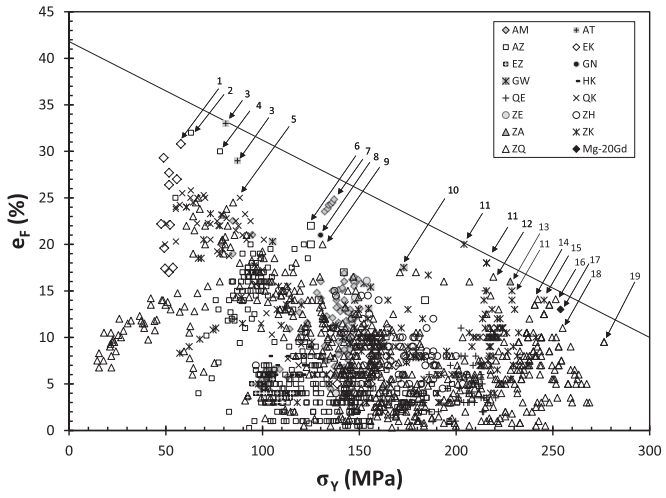

Fig. 1. Yield strength versus elongation plot for various series of Mg alloys.

goes immediately above all maximum points has the following equation:

$$e_{F(max)}(\%) = 41.8 - 0.106\sigma_y \quad (5)$$

This line represents the true ductility potential of cast Mg alloys. It also represents the true (intrinsic) trade-off between ductility and strength, commonly referred to in metallurgy textbooks.

It is noteworthy that there are data from almost all Mg alloy systems included in this study near the true ductility potential line. While alloying additions affect the strengthening mechanisms to reach the desired yield strength, the maximum elongation at that particular yield strength is independent from the chemical composition of the alloy. This result has significant implications for the selections of Mg alloys for particular applications and/or future Mg alloy development efforts, because the same strength and elongation can be obtained by different alloying additions. As an example, at $\sigma_y \approx 235$ MPa in Fig. 1, there are two data points just below the line, one from the ZK (Mg–Zn–Zr) alloy family (#15) and the other from the ZQ (Mg–Zn–Ag) alloy family (#14). Although they have almost the same strength and elongation, the cost for the two alloys can be expected to be vastly different because of the Ag addition in the ZQ series. Hence, significant cost savings can be achieved by selecting a less expensive alloy and careful design of processes to minimize structural defects.

Relevant details about selected points on or immediately below the line are presented in Table 1. The details in Table 1 have several implications:

1. As mentioned previously, there are data from almost all alloy families around the line.
2. Casting geometry and size include plate, separately-cast tensile bars, ingot, and actual premium and aerospace castings. Hence, it can be stated that maximum elongation can be reached for any casting shape and size.
3. Specimens with different tempers, produced via various casting processes can reach the maximum elongation levels.
4. Table 1 shows that grain size of specimens near the true ductility line shows ranges between 10 and 163 μm. Hence, there is strong evidence that grain size has no effect on ductility when castings are free from structural defects.

That grain size has no effect on the ductility potential is consistent with the finding in cast Al-7% Si–Mg alloys that SDAS, similarly, does not affect $e_{F(max)}$. Although Lee [9] has been correct to state that the effect of grain size on elongation is lessened with increasing quality, the results in the present study suggest that the effect of grain size on elongation disappears completely as elongation approaches $e_{F(max)}$. If grain size is taken as a measure of the local solidification time, then, in the absence of bifilms, the heterogeneous nucleation sites for pores and intermetallics do not exist, resulting in defect-free castings, regardless of how long it takes for the castings to solidify. Moreover, cracking along grain boundaries is not expected to occur as easily during tensile deformation when bifilms (and intermetallics) are not on grain boundaries. Although grain boundaries are usually assumed to be weak and consequently cracking along them is considered normal, recent research [60] on bicrystals has shown that the strength of grain boundaries, when inclusions and impurities are not present, approaches the theoretical strength of monocrystals. Hence cracking along grain boundaries during tensile deformation and a "beneficial" effect of grain refining should be taken as symptoms of a high density of bifilms in the structure. This point has been suggested by Campbell [18] to explain the true "grain refining" effect of Zr, a common alloying addition in Mg alloys, by the sedimentation of bifilms to the bottom of the melt.

Table 1
Detailed information about data indicated in Fig. 1.

Point	Alloy	Ref.	Temper	d (μm)	Process	Casting
1	EK11	35	F	30	Permanent mold casting	5 mm diameter, 25 mm length
2	AZ31	36	F	–	Copper mold	150 mm diameter, 200 mm length
3	AT33	37	F	55	Copper mold	60 mm × 40 mm × 12 mm
4	AZ31	36	F	163	Copper mold with electromagnetic stirring	150 mm diameter, 200 mm length
5	QK71	38	T6	71	Green sand casting	13 mm diameter cast tensile bars
6	AZ91	39	W	125[a]	Sand casting	200 mm × 100 mm × 15 mm plate
7	AM60	40	F	10[a]	Intensively sheared melt, high pressure die casting	6.4 mm diameter bars
8	GN112	41	W	70[a]	Permanent mold casting	70 mm × 50 mm × 20 mm plate
9	ZQ33	38	T6	90[a]	Green sand casting	13 mm diameter cast tensile bars
10	GW63	42	F	25	High vacuum die casting	6.3 mm diameter tensile bars
11	ZK61	43	T6	76	Green sand casting	25.4 or 50.8 mm-thick rectangular plates with chills
12	ZQ71	43	T6	81	Green sand casting	25.4 or 50.8 mm-thick rectangular plates with chills
13	ZA81	44	T6	80	Permanent mold casting	Ingot
14	ZQ64	45	T6	–	Permanent mold casting	Aerospace casting
15	ZK61	46	T6	–	Green sand casting	13 mm diameter cast tensile bars
16	ZQ71	45	T6	–	Permanent mold casting	Aerospace casting
17	Mg–20Gd	47	F	80	Copper mold	70 mm × 40 mm × 9 mm ingot
18	ZQ91	48	T6	25	Green sand casting	13 mm diameter cast tensile bars
19	ZQ64	49	T6	–	–	12 kg premium quality casting

[a] Estimated from micrograph.

Along the same lines as grain size, the effect of section thickness should be reevaluated. Hu et al. [61] stated that yield strength and elongation decrease with section thickness, i.e., solidification time. However, when attention was paid to every detail of the casting process, Lagowski and Meier [43] reported that section thickness had no effect on the ductility of Mg alloys.

Turning our attention to past efforts to estimate defect-free elongation, Eq. (2), developed for $\sigma_Y = 125$ MPa, can be compared with Eq. (5). Taking the two extreme grain size values in Table 1, 10 and 163 μm, Eq. (2) yields 13.4% and 11.0% elongation for the defect-free condition. These numbers are significantly lower than $e_{F(max)} = 28.6\%$ found by using Eq. (5) for the same yield strength. Hence Eq. (2) underestimates $e_{F(max)}$ significantly. The same conclusion can be made for the estimates of $e_{F(max)}$ made by Weiler and Wood [25] and Lee and Shin [8]. The estimate, $e_{F(max)} = 29\%$, provided for Lee et al. [27] at $\sigma_Y \approx 120$ MPa, is almost identical to the outcome of Eq. (5) (29.1%).

The ductility potential line (Eq. (5)) can now be used to assess the structural quality of all Mg alloy castings by using Eq. (4). Therefore, Q_T can be used as a metric during any effort to improve the structural quality and hence the performance of Mg alloy castings. Until guidelines specific to Mg alloys are developed, the quality improvement recommendations made [14] for aluminum alloy castings can be taken as a starting point.

4. Conclusions

- A relationship representing the ductility potential has been developed for all cast Mg alloys:

$$e_{F(max)}(\%) = 41.8 - 0.106\sigma_y$$

- Most estimates of defect-free elongation for cast Mg alloys in the literature significantly underestimate the ductility potential.
- Grain size has no significant effect on elongation as it approached the ductility potential line.
- Chemical composition of the alloy as well as the temper affect the yield strength of metal but not the ductility potential at a given yield strength.
- Casting geometry, size and the type of casting process were not found to have any effect on the ductility potential.
- The actual elongation can be compared with the ductility potential to calculate Q_T, which can be used as a metric in any quality improvement effort in Mg alloy castings.

References

[1] P. Krajewski, A. Sachdev, A. Luo, J. Scroth, Light Met. Age 67 (5) (2009) 6–13.
[2] D.J. Bray: in AGARD Lecture Series No. 174, 1990, pp. 7–1.
[3] Anon, High Integrity Magnesium Alloy Components, 2010 (USAMP Project AMD 601, Final Report).
[4] J. Campbell, Mater. Sci. Technol. 22 (2006) 127–145 (999-1008).
[5] J.T. Staley Jr., M. Tiryakioğlu, J. Campbell, Mater Sci. Eng. A 465 (2007) 136–145.
[6] B.L. Mordike, T. Elbert, Mater. Sci. Eng. A 302 (2001) 37–45.
[7] J. Campbell, Castings, Elsevier, London, 2003 (2nd edition).
[8] C.D. Lee, K.S. Shin, Acta Mater. 55 (2007) 4293–4303.
[9] C.D. Lee, Mater. Sci. Eng. A 459 (2007) 355–360.
[10] M. Tiryakioğlu., Mater.Sci. Eng. A 527 (2010) 4546–4549.
[11] J. Song, S.-M. Xiong, M. Li, J. Allison, Mater. Sci. Eng. A 520 (2009) 197–201.
[12] N.R. Green, J. Campbell, Mater. Sci. Eng. A 173 (1993) 261–266.
[13] C. Nyahumwa, N.R. Green, J. Campbell, Metall. Mater. Trans. A 32 (2001) 349–358.
[14] M. Tiryakioğlu, J. Campbell, Intl. J. Metalcast. 8 (2014) 39–42.
[15] M. Tiryakioğlu, J. Campbell, N. Alexopoulos, Mater. Sci. Eng. A 506 (2009) 23–26.
[16] M. Tiryakioğlu, J. Campbell, Mater. Sci. Technol. 25 (2009) 784–789.
[17] M. Tiryakioğlu, J. Campbell, N.D. Alexopoulos, Metall. Mater. Trans. A 40A (2009) 1000–1007.
[18] J. Campbell, Metall. Mater. Trans. A (2015), http://dx.doi.org/10.1007/s11661-015-2955-8 (in press).
[19] J. Campbell, Mater. Sci. Technol. 22 (2006) 127–145.
[20] M. Tiryakioğlu, J. Campbell, N. Alexopoulos, Metall. Mater. Trans. B 40 (2009) 802–811.
[21] M. O.Pekguleryuz, K.Kainer, A.Kaya, Woodhead Publishing, 1st edition, 2013.
[22] J.A. Chapman, D.V. Wilson, J. Inst. Met. 91 (1962) 39–40.
[23] Z.M. Li, A.A. Luo, Q.G. Wang, L.M. Peng, P.H. Fu, G.H. Wu, Mater. Sci. Eng. A 564 (2013) 450–460.
[24] G.V. Raynor, The Physical Metallurgy of Magnesium and its Alloys, Pergamon Press, London, 1959.
[25] J.P. Weiler, J.T. Wood, Mater. Sci. Eng. A 527 (2009) 25–31.
[26] J.P. Weiler, J.T. Wood, Mater. Sci. Eng. A 527 (2009) 32–37.
[27] S.G. Lee, G.R. Patel, A.M. Gokhale, A. Sreeranganathan, M.F. Horstemeyer, Scr. Mater. 53 (2005) 851–856.
[28] M. Tiryakioğlu, J.T. Staley, J. Campbell, Mater. Sci. Eng. A 368 (2004) 231–238.
[29] M. Tiryakioğlu, J. Campbell, J.T. Staley, Mater. Sci. Eng. A 368 (2004) 205–211.
[30] M. Tiryakioğlu, J. Campbell, J.T. Staley, Scr. Mater. 49 (2003) 873–878.
[31] M. Tiryakioğlu, J.T. Staley Jr., J. Campbell, Mater. Sci. Eng. A 487 (2008) 383–387.
[32] M. Tiryakioğlu, J. Campbell, N.D. Alexopoulos, Metall. Mater. Trans. A 40A (2009) 1000–1007.
[33] M. Tiryakioğlu, J. Campbell, N. Alexopoulos, Mater. Sci. Eng. A 506 (2009) 23–26.
[34] M. Tiryakioğlu, J. Campbell, Mater. Sci. Technol. 25 (2009) 784–789.
[35] Y. Huang, W. Gan, K.U. Kainer, N. Hort, J. Magnes. Alloy. 2 (2014) 1–7.
[36] J.P. Park, M.G. Kim, U.S. Yoon, U.S. Kim, W.J. Kim, J. Mater. Sci. 44 (2009) 47–53.
[37] H.Y. Wang, X.L. Nan, N. Zhang, C. Wang, J.G. Wang, Q.C. Jiang, Mater. Chem. Phys. 132 (2012) 248–252.
[38] B. Lagowski, J. Meier, Properties of Sand Cast Magnesium Alloys, Part IV,, Department of Mines and Technical Surveys, Ottawa, Canada, (1960), p. 756–766 (Mines Branch Research Report, R63).
[39] L. Čižek, M. Greger, L. Pawlica, L.A. Dobrzański, T. Tański, J. Mater.Process. Technol. 157–158 (2004) 466–471.
[40] S. Ji, W. Yang, B. Jiang, J.B. Patel, Z. Fan, Mater. Sci. Eng. A 566 (2013) 119–125.
[41] K.Y. Zheng, J. Dong, X.Q. Zeng, W.J. Ding, Mater. Sci. Eng. A 489 (2008) 44–54.
[42] S. Li, D. Li, X. Zeng, W. Ding, Trans. Nonferrous Met. Soc. China 24 (2014) 3769–3776.
[43] B. Lagowski, J. Meier, Properties of Sand-Cast Mg Alloys, Part VIII: Foundry Characteristics of Mg–Zn–Ag–Zr Casting Alloys, Department of Mines and Technical Surveys, Ottawa, Canada, 1965 (Mines Branch Research Report, R161).
[44] J. Wang, R. Liu, T. Luo, Y. Yang, Mater. Des. 47 (2013) 746–749.
[45] A.J. Iler, Development of Manufacturing Capability for Producing High Performance Aluminum and Magnesium Alloy Castings, Northrop Corporation, 1964 (Report: NOR 64-278).
[46] J. Meier, M. Martinson, AFS Trans. 58 (1950) 742–751.
[47] Q. Peng, Y. Wu, D. Fang, J. Meng., L. Wang, J. Rare Earths 24 (2006) 466–470.
[48] A. Couture, J.W. Meier, Properties of Sand-Cast Mg Alloys, Part VI: Effect of Pouring Temperature and Holding Time, Department of Mines and Technical Surveys, Ottawa, Canada, 1965 (Mines Branch Research Report, R152).
[49] J. Meier, Research in Premium Quality Casting in Light Alloys,, Department of Mines and Technical Surveys, Ottawa, Canada, 1965 (Mines Branch Research Report, R149).
[50] B. Per, P. Ketil, W. Hakon, JOM 55 (2003) 46–51.
[51] J. Jiang, Y. Wang, Y. Li, J. Qu, W. Shan, S. Luo, J. Mater. Proc. Technol 212 (2012) 1191–1199.
[52] J.H. Forsmark, J.W. Zindel, L. Godlewski, J. Zheng, J.E. Allison, M. Li, Integr. Mater. Manuf. Innov. 4 (2015) 1–38.
[53] J. Jiang, Y. Wang, J. Qu, Trans. Nonferrous Met. Soc. China 24 (2014) 321–333.
[54] H. Honsel, P. Zimmermann, Giesserei 50 (1963) 765–781.
[55] K.E. Nelson, AFS Trans. 69 (1961) 756–766.
[56] B. Lagowski, J. Meier, Properties of Sand Cast Magnesium Alloys, Part V, Department of Mines and Technical Surveys, Ottawa, Canada, 1964 (Mines Branch Research Report, R140).
[57] A. Couture, J.W. Meier, The Effect of Test Bar Variables on the Mechanical Properties of Mg Casting Alloys, Department of Mines and Technical Surveys, Ottawa, Canada, 1965 (Mines Branch Research Report, R151).
[58] A. Couture, J.W. Meier, Properties of Sand-Cast Mg Alloys, Part VII: The Effect of Wall Thickness on Tensile Properties of Mg–Al–Zn Alloy Castings, Department of Mines and Technical Surveys, Ottawa, Canada, 1965 (Mines Branch Research Report, R153).
[59] A. Wang, B. Zhang, D. Li, R. Fritzsch, X. Zeng, H.J. Roven, W. Ding, Trans. Nonferrous Met. Soc. China 24 (2014) 3762–3768.
[60] I.M. Mikhailovskij, T.I. Mazilova, V.N. Voyevodin, A.A. Mazilov, Phys. Rev. B 83 (2011) 134115.
[61] H. Hu, M. Zhou, Z. Sun, N. Li, J. Mater. Process. Technol. 201 (2008) 364–368.

APPENDIX II

Shape Casting: 6th International Symposium
Edited by: Murat Tiryakioğlu, Mark Jolly, and Glenn Byczynski
TMS (The Minerals, Metals & Materials Society), 2016

CHARACTERIZATION OF TENSILE DEFORMATION IN AZ91D Mg ALLOY CASTINGS

Ogün ŰNAL, Murat Tiryakioğlu

University of North Florida; 1 UNF Drive; Jacksonville, FL 32224, USA

Keywords: Work Hardening; Kocks-Mecking; Porosity; Defects; Bifilms

Abstract

AZ91 cast Mg alloy specimens in T4 and T6 tempers have been tested in tension. True stress - true plastic strain relationship has been characterized by evaluating the fits to four constitutive equations. Moreover, work hardening behavior in both tempers has been investigated and how well the four constitutive equation can model this behavior has been tested. The effects of temper and structural quality on tensile properties and work hardening are discussed in the paper.

Introduction

Mg alloy castings have been attractive candidates in load-bearing applications due to their low density [1]. However, Mg alloys have not been used as frequently as cast aluminum alloys in aerospace and automotive applications. Barriers that limits the wider use of Mg alloy have been recently identified as [2] (i) porosity and hot-tearing during solidification, (ii) thermal treatments and (iii) process design to produce high-integrity cast magnesium components with high ductility and strength, low porosity that are free from structural defects such as pores and oxide bifilms.

Structural defects such as porosity and bifilms in castings adversely affect mechanical properties, including fatigue life [3,4], elongation (e_F) [5,6,7,8,9] and tensile strength [10,11]. Recent research showed that [12] surface films are entrained into the casting, act as nucleation sites for pores and intermetallics, and eventually lead to premature fracture. It is imperative that the initial melt has a low density of entrained films, referred to as bifilms, and the filling system be designed to minimize or even eliminate damage by entrainment of surface films. In the absence of structural defects, it has been recently shown by the authors [13] that cast Mg alloys have a high tensile ductility potential.

In cast Al alloys, it was found [14,15,16] that true tensile deformation characteristics cannot be determined when structural defects are present, because these defects reduce the work hardening rate. Moreover, a sudden drop in work hardening rate was observed just before final tensile fracture as a result of major structural defects. There have been several studies [17,18,19] on tensile work hardening characteristics of Mg alloys. In these studies various constitutive equations have been used. To the authors' knowledge, there is no comprehensive study in which constitutive equations have been evaluated and work hardening characteristics have been characterized in cast Mg alloys. This study is motivated by this gap in the literature.

Background

A review of literature showed that the true stress (σ) – true plastic strain (ε_p) relationships in Mg alloys have been modeled by using the Hollomon [20,21], Voce [22,23], Ludwig [24] and Swift [25] constitutive equations. These equations are presented in Table 1. Note that the Hollomon Equation has two parameters while the others have three parameters that need to be estimated. Work hardening rate, Θ, can be written as;

$$\Theta = \frac{d\sigma}{d\varepsilon_p} \tag{1}$$

Tensile instability takes place when the Considère criterion is met such that $\Theta = \sigma$. In many applications, it is important to estimate the stress and strain where the Considère criterion is met. Therefore it is necessary to evaluate how the constitutive equations model work hardening rate. Hence, the derivative of all constitutive equations were taken and rearranged so that Θ is only a function of σ. These work hardening rate equations are also provided in Table 1.

Table 1. True stress-true plastic strain and work hardening rate as a function of true stress for the four constitutive equations.

Constitutive Equations	**$\sigma = f(\varepsilon_p)$**	**$\Theta = f(\sigma)$**
Hollomon	$K_H {\varepsilon_p}^{n_H}$	$n_H \left(\frac{\sigma}{K_H}\right)^{\left(\frac{n_H - 1}{n_H}\right)}$
Voce	$\sigma_\infty - (\sigma_\infty - \sigma_0)e^{-K_V \varepsilon_p}$	$K_V(\sigma_\infty - \sigma)$
Ludwig	$\sigma_L + K_L {\varepsilon_p}^{n_L}$	$n_L K_L \frac{(\sigma - \sigma_L)^{\left(\frac{n_L - 1}{n_L}\right)}}{K_L}$
Swift	$K_S(\varepsilon_p + \varepsilon_S)^{n_S}$	$K_S n_S \left(\frac{\sigma}{K_S}\right)^{\left(\frac{n_S - 1}{n_S}\right)}$

In castings, work hardening rate analysis is conducted usually to evaluate structural quality; when Θ was plotted versus σ in cast aluminum alloys, a sudden drop was observed just prior to fracture [14,15]. Fractographic analysis showed that this sudden drop could be attributed to major casting defects. In specimens with a higher structural quality (no major defects), there was no sudden drop in Θ and deformation continued past the intersection of the curves for Θ and σ.

In cast Al alloys, work hardening rate was found to decrease linearly with true stress, which represents the Kocks-Mecking (KM) work hardening model [26, 27];

$$\Theta = \frac{d\sigma}{d\varepsilon_p} = \Theta_0 - K\sigma \tag{2}$$

where Θ_0 is the initial work hardening rate and K is the KM parameter. Note that Equation 2 is identical to the work hardening rate for the Voce equation in Table 1, such that, $\Theta_0 = \sigma_\infty K_V$ and $K = K_V$. With decreasing elongation (i.e., structural quality [13,28]), K was found to increase in A206-T7 aluminum alloy castings [16].

The performance of the four constitutive equations listed in Table 1 in modeling the work hardening behavior of AZ91D cast magnesium alloy was assessed by using tensile data from specimens in T4 and T6 tempers. Moreover, the work hardening characteristics in T4 and T6 were characterized by using σ-Θ charts.

Experimental Details and Analysis

The chemical composition of the AZ91D cast magnesium alloy used in this study is given in Table 2.

Table 2. Chemical composition (in wt.%) of the AZ91D Mg alloy used in this study.

Al	Zn	Mg	Si	Fe	Be	Ni	Cu	Mg
8.7	0.65	0.25	0.006	0.003	0.0008	0.0006	0.0005	Balance

Initially sand cast tensile bars with 12.7 mm diameter were produced. These bars were machined into 6.4 mm diameter bars and heat treated to T4 and T6 tempers. Thirty specimens in each temper were tested in tension at a strain rate of 10^{-3}/s. The specimens with the highest elongation in each dataset were determined and their tensile data were used in this study. True stress and true strain values were obtained by assuming conservation of volume.

Results and Discussion

Evaluation of Constitutive Equations

The σ-ε_p curves of the specimens selected for this study are presented in Figure 1. The specimens had yield strength (σ_Y) of 90.4 and 124.6 MPa and elongation (e_F) of 16.2 and 8.0% for T4 and T6 tempers, respectively.

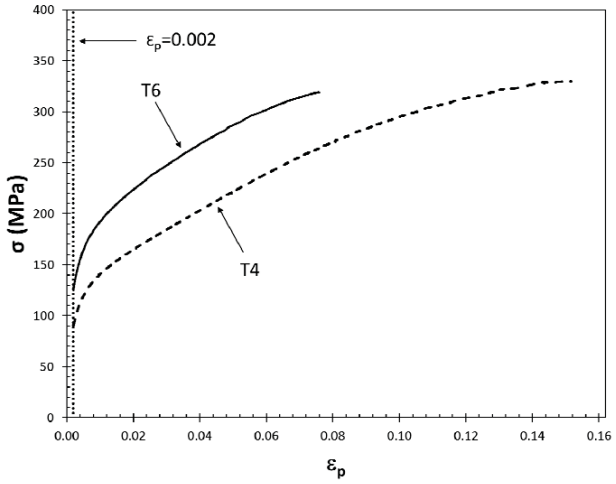

Figure 1. True stress-true plastic strain curves for the two specimens investigated in this study.

The Newton-Raphson method was used to estimate the parameters of the four constitutive equations that provided the best fit, i.e., lowest root mean square error (RMSE) and highest coefficient of determination, R^2, to the tensile data shown in Figure 1. The values of the estimated parameters as well as RMSE and R^2 for each fit are presented in Table 3. Note that the R^2 values in each case is above 0.99 which shows that all constitutive equations included in this study can be used to characterize the true stress-true strain relationship in this alloy. For the specimen in T4 temper, the best fit was obtained by the Voce equation, and for the T6 specimen, the Ludwig equation provided the best fit.

Table 3. Estimated parameters of constitutive equations for the two specimens and the RMSE and R^2 of each fit.

		T4			T6		
Equations	**Parameters**	**Estimate**	**RMSE (MPa)**	**R^2**	**Estimate**	**RMSE (MPa)**	**R^2**
Hollomon	**K_H (Mpa)**	645.2	6.22	0.991	605.0	2.81	0.997
	n_H	0.346			0.250		
Voce	**σ_∞ (MPa)**	393.8	3.14	0.998	341.5	5.14	0.991
	σ_0 (MPa)	106.9			135.8		
	K_V	10.5			27.2		
Swift	**K_S (MPa)**	733.7	3.40	0.997	636.0	2.33	0.998
	ε_S	0.007			0.001		
	n_S	0.413			0.269		
Ludwig	**σ_L (MPa)**	68.5	3.51	0.997	54.7	1.99	0.999
	n_L	0.516			0.334		
	K_L (MPa)	729.4			628.2		

Work hardening rate for the two tensile curves in Figure 1 were obtained by a moving 11-point fitting scheme and its differentiation. The change in Θ with the difference between true stress and yield strength (σ-σ_Y) for the two specimens is presented in Figure 3. Note that curves with work hardening rates obtained by using the equations in Table 1 and estimated parameters in Table 3 are also indicated. For the T4 specimen in Figure 3.a, all constitutive equations initially underestimate the work hardening rate. The Voce equation provides the best fit after approximately σ-σ_Y= 50 MPa. All constitutive equations provide almost identical fits for σ-$\sigma_Y \geq$ 100 MPa. For the T6 specimen, Hollomon, Swift and Ludwig equations give similar fits that closely follow the work hardening rate curve. The Voce equation does not provide a good fit, especially at lower stress levels.

The results for the T4 and T6 specimens are contradictory in how the four constitutive equations perform. Among the four equations, only the Voce equation is based on the evolution of the dislocation density with plastic deformation, developed by Kocks and Mecking [26,27]. Merely fitting the four constitutive equations to the stress-strain data past yield strength is not sufficient to characterize the plastic deformation behavior in this alloy.

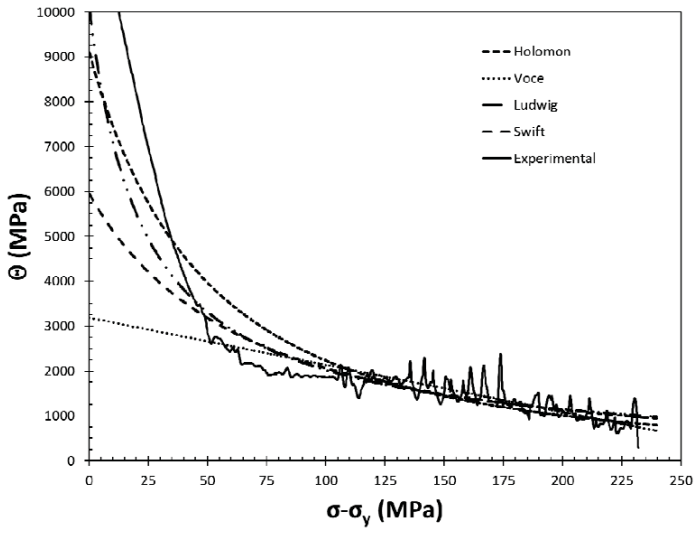

(a)

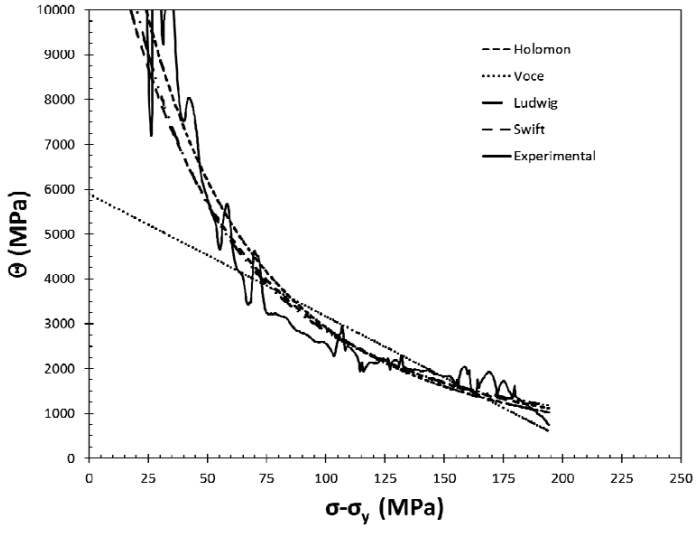

(b)

Figure 2. Kocks-Mecking diagram and plots of work hardening rate calculated from derivation of constitutive equations for (a) T4 and (b) T6.

Kock-Mecking Analysis

The work hardening rate in the two specimens as a function of σ-σ_Y is presented again in Figure 3. Note that in both specimens, there is a distinct Stage III work hardening region in Θ decreases linearly with increasing stress, following Equation 2. For the T4 specimen, Θ_0 = 4,827 MPa and K = 12.8. For the T6 specimen, Θ_0 and K are 5,709 MPa and 14.1, respectively.

In both specimens, a sudden drop in work hardening rate prior to final fracture is observed. It was determined [14,15] in cast aluminum alloys via fractographic analysis that this sudden drop was a result of the presence of structural defects, such as bifilms and pores in castings. These defects result in premature fracture in tension. Note that the sudden drop in work hardening rate for both specimens has taken place at a level well above the level of true stress, as indicated by the "$\Theta = \sigma$" line. Therefore, the Considère criterion is met only at the microscale, in areas around casting defects that acted as stress concentrators.

It is noteworthy that the T4 specimen exhibited first a steep decrease in work hardening rate, due to a short elastoplastic transition, followed by a plateau in work hardening rate, indicated as Stage II. Consequently, there is a region in the true stress-true plastic strain curve in Figure 1 where true stress increases linearly with strain, approximately between true stress levels of 150 and 250 MPa. For the T4 specimen, Stage II work hardening is followed by Stage III in which work hardening rate decreases linearly with stress. The presence of a Stage II with constant work hardening rate was reported for pure Mg [17] and several Mg alloys [29,30]. Note that Θ is 1850 MPa in Stage II in Figure 3.a, which is similar to the levels reported for pure Mg [17] and equal channel angular pressed (ECAP) AM60 alloy [29].

The steep decrease in Θ, indicative of a short elastoplastic transition, is in contradiction with the results reported [31] for a hot-extruded AZ31B alloy, for which internal strains developed in tension and compression were measured by *in situ* neutron diffraction. The results showed that the elastoplastic transition is extended, sometimes lasting as long as 10% strain. Moreover, work hardening is a result of "a composite-like load sharing between soft- and hard-oriented grains" [31]. Note that the decrease in Θ for the T6 specimen is not as steep and there is no Stage II with a constant work hardening rate, Figure 3.b. Hence the elastoplastic transition is longer for the T6 specimen. Kocks Mecking analysis conducted by del Valle et al. [29] on ECAP AM60 showed that some specimens displayed the short elastoplastic transition followed by a Stage II, similar to the T4 specimen in Figure 3.a, whereas others had an extended elastoplactic transition and no Stage II with a constant Θ, similar to the T6 specimen, Figure 3.b. The reason for this difference in ECAP AM60 was attributed to texture effects. However, to the authors' knowledge, there is no study in the literature in which the differences in work hardening behavior has been attributed to temper in Mg alloys. More research is needed to determine the reasons behind the effect of temper on work hardening behavior.

Conclusions

- All four consttutive equations give similar fits to true stress-true plastic strain data. However, Kocks-Mecking analysis is required to characterize the work hardening behavior in AZ91D alloy.
- A sudden drop in work hardening rate just prior to fracture took place observed in both specimens, indicative of the presence of structural defects.

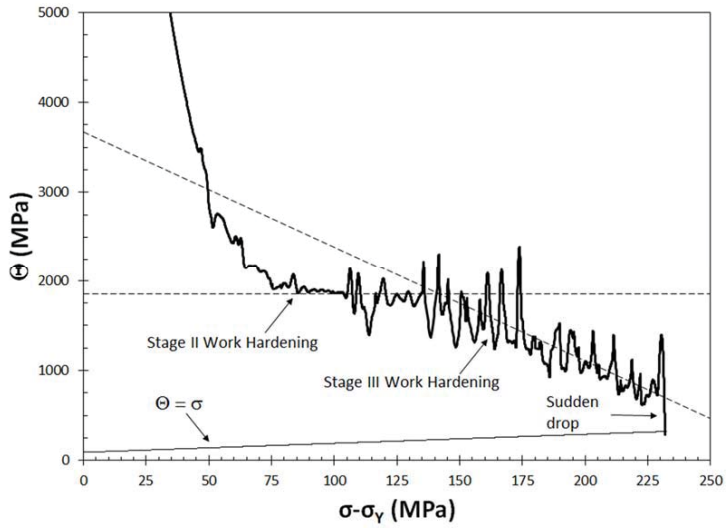

(a)

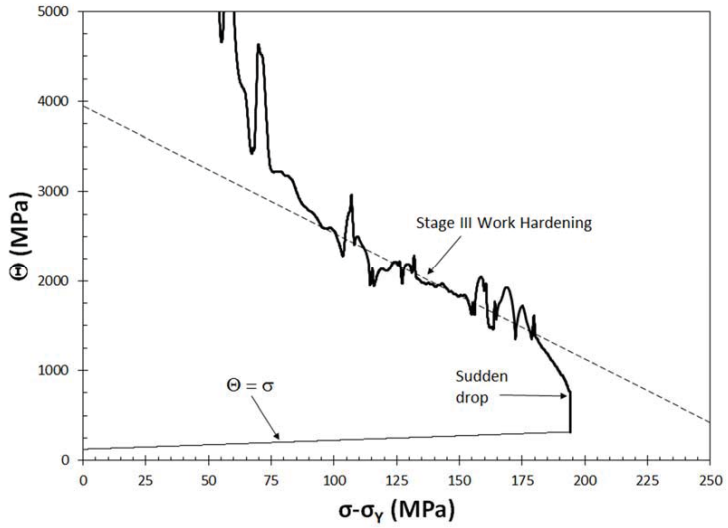

(b)

Figure 3. The relationship between (σ-σY) and work hardening rate, Θ, for specimens in (a) T4 and (b) T6 temper.

- Work hardening behavior was observed to be affected by temper; a short elastoplastic transition followed by a Stage II with a constant Θ was observed in the T4 specimen, whereas the T6 specimen exhibited a longer elastiplastic transition and no Stage II with a Θ. Hence, temper was found to affect the work hardening behavior in Mg alloys.
- Both T4 and T6 specimens displayed Stage III work hardening, with Θ decreasing linearly with true stress.

References

1. P. Krajewski, A. Sachdev, A. Luo, J. Scroth, Ligt Metals Age, 67 5 (2009) 6-13.
2. Anon. "High Integrity Magnesium Alloy Components", USAMP Project AMD 601, Final Report, (2010).
3. J. Campbell, Castings, 2nd Edition, Butterworth-Heinemann Ltd, Oxford, 2003.
4. J. T. Staley Jr., M. Tiryakioglu, J. Campbell, Mater Sci. Eng. A 465 (2007) 136-145.
5. B. L. Mordike, T. Elbert, Mater. Sci. Eng. A, 302 (2001) 37-45.
6. C. D. Lee, K. S. Shin, Acta Mater. 55 (2007) 4293-4303.
7. C. D. Lee, Mater. Sci. Eng. A 459 (2007) 355-360.
8. M. Tiryakioğlu. Mater.Sci Eng. A, 527 (2010) 4546–4549.
9. J. Song, S.-M. Xiong, M. Li, J. Allison: Mater. Sci. Eng. A 520 (2009) 197–201.
10. N. R. Green, J. Campbell, Mater. Sci. Eng. A, 173 (1993) 261-266.
11. C. Nyahumwa, N. R. Green, J. Campbell, Metall. Mater. Trans. A 32 (2001) 349-358.
12. J. Campbell, Mater. Sci. Technol. 22 (2006) 127-145 999-1008.
13. O. Űnal, M. Tiryakioğlu: Mater. Sci. Eng. A, 643 (2015) 51-54.
14. M. Tiryakioğlu, J. Campbell, J.T. Staley: Scripta Mater., (2003), vol. 49, p. 873.
15. M. Tiryakioğlu, J. Campbell, J.T. Staley: Mater. Sci. Eng. A, (2004), vol. 368, p. 205.
16. M. Tiryakioğlu, J.T. Staley, Jr., J. Campbell: Mater. Sci. Eng. A. 487 (2008) 483-487
17. C. H. Caceres, A.H. Blake, Mater. Sci. Eng. A 462, (2007), 193-196.
18. H.-Y. Wu, J.-C. Yan, H.-H. Tsai, C.-H. Chiu, G.-Z. Zhou, C.-F. Lin: Mater. Sci. Eng. A, 527 (2010) 7197-7203.
19. N. Afrin, D.L. Chen, X. Cao, M. Jahazi: Scripta Mater. 57 (2007) 1004–1007.
20. C.H. Caceres. Int J Cast Met Res. 10, (1998) 293.
21. H Takuda, T Yoshii, N Hatta: J. Mater. Process. Technol. 89–90 (1999) 135–140.
22. S.R. Agnew, D.W. Brown, C.N. Tomé: Acta Mater. 54 (2006) 4841–4852.
23. S.R. Agnew, M.H. Yoo, C.N. Tomé: Acta Mater. 49 (2001) 4277–4289.
24. M. Turski, J. F. Grandfield, T. Wilks, B. Davis, R. DeLorme, K. Cho: In "Essential Readings in Magnesium Technology" (ed. S.N. Mathaudhu, A.A. Luo, N.R. Neelameggham, E.A. Nyberg, W.H. Sillekens) pp. 457-462, Wiley, 2014.
25. E. El-Magd, , M. Abouridouane: Int. J. Impact Eng. 32 (2006) 741–758.
26. U.F. Kocks: J. Eng. Mater. Tech., (1976), vol. 98, p. 76.
27. H. Mecking, U.F. Kocks: Acta Metall., (1981), vol. 29, p. 1865.
28. M. Tiryakioğlu, J. Campbell, N. Alexopoulos: Metall. Mater. Trans. B, 40 (2009) 802-811.
29. J.A. del Valle, F. Carreno, O.A. Ruano: Acta Mater. 54 (2006) 4247-4259.
30. M. Karami, R. Mahmudi: Mater. Sci. Eng. A 607 (2014) 512-520.
31. S.R. Agnew, C.N. Tomé, D.W. Brown, T.M. Holden, S.C. Vogel: Scripta Mater. 49 (2003) 1003-1008.

APPENDIX III

Derivation of Four Constitutive Equations:

Hollomon:

$$\sigma = K_H \varepsilon_p^{\,n_H}$$

$$\frac{d\sigma}{d\varepsilon} = nK_H \varepsilon^{(n_H - 1)}$$

$$\Theta = n_H \left(\frac{\sigma}{K_H} \right)^{(\frac{n_H - 1}{n_H})}$$

Ludwig:

$$\sigma = \sigma_L + K_L \varepsilon_p^{\,n_L}$$

$$\frac{d\sigma}{d\varepsilon} = n_L K_L \varepsilon^{(n_L - 1)}$$

$$\Theta = n_L K_L \frac{(\sigma - \sigma_L)^{(\frac{n_L - 1}{n_L})}}{K_L}$$

Swift:

$$\sigma = K_S (\varepsilon_p + \varepsilon_S)^{n_S}$$

$$\Theta = K_S n_S \left(\frac{\sigma}{K_S} \right)^{(\frac{n_S - 1}{n_S})}$$

Voce:

$$\sigma_\infty - (\sigma_\infty - \sigma_0) e^{-K_V \varepsilon_p}$$

$$\frac{d\sigma}{d\varepsilon} = 0 - (\sigma_\infty - \sigma) \exp(-K_V \varepsilon)(-K_V)$$

$$\Theta = K_V \left(\sigma_\infty - \sigma \right)$$

APPENDIX IV

Calculation of RMSE:

$$RMSE = \sqrt{\frac{\Sigma_{t=1}^{n}(y_t - y)}{n\text{-}a}}$$

Number of Data Points for T4 specimen: 3237

Number of Data Points for T6 specimen: 2150

Number of Parameters for Hollomon: 2

Number of Parameters for Voce: 3

Number of Parameters for Ludwig: 3

Number of Parameters for Swift: 3

APPENDIX V

Calculation of Quality Index:

$$Q_T = \frac{e_F}{e_{F(\max)}}$$

Calculation of Ductility Potential:

$$e_{F(\max)}(\%) = 41.8 - 0.106\sigma_Y$$

True Stress:

$$\sigma = \sigma_e(1+\varepsilon_e)$$

True Strain:

$$\varepsilon = \ln(1+\varepsilon_e)$$

True Plastic Strain:

$$\varepsilon_p = \ln(1+\varepsilon_e) - (\sigma / E)$$

E_{Mg} = 45000 MPa

VITA

I graduated High School and applied for undergraduate program at University of Istanbul. I completed my internship in Kale Aero in 2011. I received my Bachelors of Science degree in Metallurgy and Materials Engineering in 2014. I have been accepted for the graduate program in Mechanical Engineering at University of North Florida. During this program I have worked as teaching, research and laboratory assistant and also I have published two papers which are listed below:

1. O. Unal, M. Tiryakioglu, On the Ductility Potential and Assessment of Structural Quality in Mg Alloy Castings, Mater. Sci. and Eng. A., 643, (2015), 51-54.
2. O. Unal, M. Tiryakioglu, Characterization of Tensile Deformation for AZ91D Mg Alloy Castings, to be presented in TMS 2016.